DISSERTATION

Modeling and Simulation of Surface Processes at Nanoscale Sensors

ausgeführt zum Zwecke der Erlangung des akademischen Grades
eines Doktors der Naturwissenschaften unter der Leitung von

Associate Prof. Dipl.-Ing. Dr. techn. Clemens Heitzinger

E101–Institut für Analysis und Scientific Computing, TU Wien

eingereicht an der Technischen Universität Wien
Fakultät für Mathematik und Geoinformation
von

Mag. Gerhard Tulzer BSc
Matrikelnummer 0504759
Hildebrandgasse 4/2/5
1180 Wien

Diese Arbeit haben begutachtet

—————————————   ——————————
Clemens Heitzinger   Anton Köck

Wien, im März 2015

Kurzfassung

Die vorliegende Arbeit befasst sich mit Oberflächenprozessen an Nanowire-Sensoren. Im Speziellen werden Gassensoren sowie Biosensoren betrachtet.

Im Falle von Gassensoren liegen keine direkten Messungen der Target-Moleküle an der Oberfläche vor. Deshalb müssen die Informationen darüber über eine Kopplung der Oberflächenprozesse mit einem elektrischen Transportmodell für den Halbleiter beschafft werden. Die benötigten Daten können dann aus dem vom Sensor gegebenen Signal bestimmt werden.

Im Falle von Biosensoren ist es nicht ausreichend, Hybridisierung und Dissoziation an der Oberfläche zu betrachten, sondern es muss auch die Bewegung der Target-Moleküle in der den Sensor umgebenden Flüssigkeit beachtet werden, was ein gekoppeltes System von Reaktions-Diffusions-Gleichungen liefert.

In dieser Arbeit werden Modelle auf zwei verschiedenen Ebenen für beide Systeme entwickelt. Erstens werden deterministische Modelle aus der Literatur für die genannten Systeme angepasst, was auf nichtlineare gewöhnliche Differentialgleichungen für Gassensoren und ein gekoppeltes Reaktions-Diffusions-System für Biosensoren führt. Mit diesen Modellen ist es möglich, die die Oberflächenprozesse bestimmenden Parameter aus gegebenen Messdaten zu bestimmen.

Zweitens werden diese Modelle verfeinert indem die zufällige Natur von chemischen Prozessen berücksichtigt wird, was auf stochastische Modelle führt. Im Falle von Gassensoren wird dieses Modell benützt, um das Verhalten des Rausch-Levels im gemessenen Signal qualitativ zu erklären. Die Messdaten werden dazu mittels einer Wavelet-Zerlegung betrachtet. Für das System der Biosensoren wurden zwei Algorithmen (einer in einer, einer in zwei Dimensionen) implementiert um das gekoppelte System zu simulieren. Während Simulationen in einer Dimension das grundsätzliche Verhalten und erste wichtige Eigenschaften des Systems sichtbar machen, können die Simulationen in zwei Dimensionen genutzt werden, um Besonderheiten in der Geometrie mit dem Verhalten des Sensors in Zusammenhang zu bringen.

Abstract

The work at hand considers the surface processes taking place at nanowire sensors. In particular, gas sensors as well as biosensors are considered.

When dealing with gas sensors, there are no direct measurements of the surface interactions at hand. Therefore, the surface interaction model has to be coupled with an electric transport model for the nanowire, which allows to relate the measured signal to the surface processes.

In the case of biosensors, not only hybridization and dissociation at the surface, but also the movement of the target molecules in the liquid surrounding the nanowire needs to be taken into account, which yields a coupled system of reaction-diffusion equations.

In this work, these systems are modeled at two different levels. First, deterministic models are adopted from literature to obtain a system of highly nonlinear ordinary differential equations for gas sensors and a system of reaction-diffusion equations for biosensors. These systems are then used to determine the parameters governing the surface processes taking place at both devices.

Second, we refine this approach to obtain stochastic models for the systems of interest. In the case of gas sensors, this model is used to qualitatively explain the noise level in the measured signal. To this end, the experimental data is analyzed using wavelet decomposition. For the biosensors, two algorithms (one in 1D and one in 2D) were implemented to simulate the movement of the target particles as well as the hybridization and dissociation processes at the surface. The one-dimensional algorithm allows first insights in the general behavior and important features of the system. The two-dimensional simulations enable distinction of several regions of the surface that show different behavior under the presence of target molecules.

Acknowledgments

First and foremost, I am grateful to my advisor, Assistant Prof. DI Dr. Clemens Heitzinger for giving me the opportunity to work in his emerging research group, for giving me the chance to attend several scientific conferences, and, of course, to prepare the work at hand.

I thank Dr. Stefan Baumgartner and DI Dr. Martin Vasicek, who constituted the research group in the beginning of my doctoral studies and who helped me a lot in the beginning of my research in this field.

The work on gas sensors would not have been possible, if it were not for the group of Univ.-Doz. Mag. Dr. Anton Köck. I would like to thank especially Dr. Elise Brunet and Dr. Stephan Steinhauer, who built the sensors and performed the measurements discussed in this thesis, and of course were always there for questions on the behavior of the devices. Also, I am grateful to Univ.-Doz. Mag. Dr. Anton Köck and Dr. Giorgio C. Mutinati for many fruitful discussions.

I cannot thank Michaela Buhl enough for her patience with me during the intense months of preparing this thesis, for her unlimited support and for being a source of motivation at any time.

Above all I would like to thank my parents, Mag. Dr. Friedrich Tulzer and Mag. Gerhild Tulzer, and my whole family for all their constant support and encouragement.

Contents

Chapter 1

Introduction

Generally, a sensor is a device that translates information on the investigated situation into information that can be processed by humans. As an example, a thermometer relates the density of mercury to the temperature, a laser speedometer relates the phase shift of the light wave to the speed of a vehicle, and a gas sensor relates the presence and concentration of a gas to an electrical signal, and the respective thing is performed by a biosensor. The part of a sensor performing this core feature is called *transducer*, which is the most important structure of the device. This work is about the interactions of target particles, i.e. gas molecules or biomolecules with the transducer.

Over the decades and centuries, there was a continuous development of the methods implemented and of the devices for the measurement of all the quantities arising in everyday life. Nowadays, the clear focus for improvement is on miniaturizing devices for mobile use, even as parts of things everybody carries around with them at any time such as smartphones or tablets. To achieve this goal, making use of structures at the micro- and nanoscale is unavoidable.

The quality of a sensor, regardless of its target, can be characterized by three parameters:

- *Stability:* To obtain reliable results from a sensing device, the response must always be the same under the same conditions. If this requirement is not met, calibrations prior to the measurement are in order. Usually, it is necessary to perform one calibration when using a device the first time. A lack of stability leads to a need for frequent re-calibration, which is at least inconvenient for the user, and in worst cases, not manageable.

- *Sensitivity:* It is obvious that there needs to be a response of the device to the presence of the target species, whatever this is. However, a good sensor will not only tell that the target species is there, but also report how much of it is present. The precision of this

---

feature and also the detection limit, i.e. the lowest quantity detectable with the sensor at hand, are important when deciding which device to use.

- *Selectivity:* The sensor response should only be due to the quantity of interest. If there are other species present at the transducer, they need to be disregarded in any way. Depending on the specific target, there are different strategies to ensure this, although this requirement cannot always be met easily and is still open for discussion in certain cases, as will be seen later on.

Especially when it comes to nanoscale devices, their optimal design with respect to the three mentioned parameters is still a matter of discussion. In particular, there are two possibilities to gain insight on this topic. First, one could build different devices and compare their performance under circumstances they will face during their application. This is extremely money and time consuming, since expensive machinery is needed and the manufacturing process takes some time. Second, one could predict the sensor's behavior by conducting computer simulations. This approach is much cheaper in both of the discussed quantities and therefore favorable.

Recently, a self-consistent 3d model for electrical conduction in nanowire BIOFET sensors was derived and mathematically analyzed [7, 45]. This approach was refined and improved [8, 12] and used for optimal sensor design [9, 10, 11]. The topic of this work is to derive a model for the surface processes taking place at semiconductor nanowires used for both gas sensing and detection of biomolecules.

1.1   Gas Sensors

There are many reasons to measure the ingredients of a gas. The most straightforward application is of course monitoring air quality under certain circumstances. Different settings like air pollution in a city or heating ventilation and air conditioning (HVAC) systems are of interest here. Moreover, there are many processes where toxic gases are produced and people must not be exposed to them. Therefore, a reliable alarm is needed, which concerns home safety as well as industrial processes. A different branch is mobile health care, where mostly breath analysis is addressed. Several diseases can be diagnosed by investigating the compounds of the exhaled air, and the availability of mobile devices to conduct the analysis is of great value. For a review on possible applications, see [103].

Considering metal oxide gas sensors, stability is achieved using suitable processes for nanowire growth and circuit integration. Since most of the metal oxides are capable of detecting many different gas species, sensitivity is established and discussed later on in detail. However, selectivity is still an issue, as might become clear from the previous statement. The investigation of surface processes, which is the topic of one part of the work at hand, is an important step towards amelioration of the situation.

In general, there are many different approaches to detect gases and monitor their quantities. Apart from optical, capacitive, calorimetric or acoustic wave sensors, there are two types of particular interest. First, sensors with a field-effect transistor (FET) configuration enable a charge transport characteristic that is very sensitive to the gate potential, which is in turn sensitive to the target gas. Second, there are conductometric sensors, where the metal oxide

works as a resistor, changing its resistivity according to present gas species. In this work, we shall deal with conductometric sensors, and we therefore turn our attention on this type for the remainder of this discussion.

The working principle of conductometric gas sensors is very simple. The basic structure, here in the case of a metal-oxide nanowire gas sensor, is shown in Figure 1.1. The core is the metal oxide nanowire which is contacted to two electrodes. The nanowire acts as a transducer, which transforms the chemical signal of gas interaction into an electrical one. If one applies a voltage between these electrodes, the current through the metal oxide can be measured.

During the measurement process, the metal oxide is exposed to the gaseous probe of interest. When a gas molecule is near the sensor surface, it may adsorb and, during this process, exchange electrons with the metal oxide, which alters the number of free carriers in it. This yields a modulation of the conductance of the material, which corresponds to obtaining a change in the current for a fixed applied voltage.
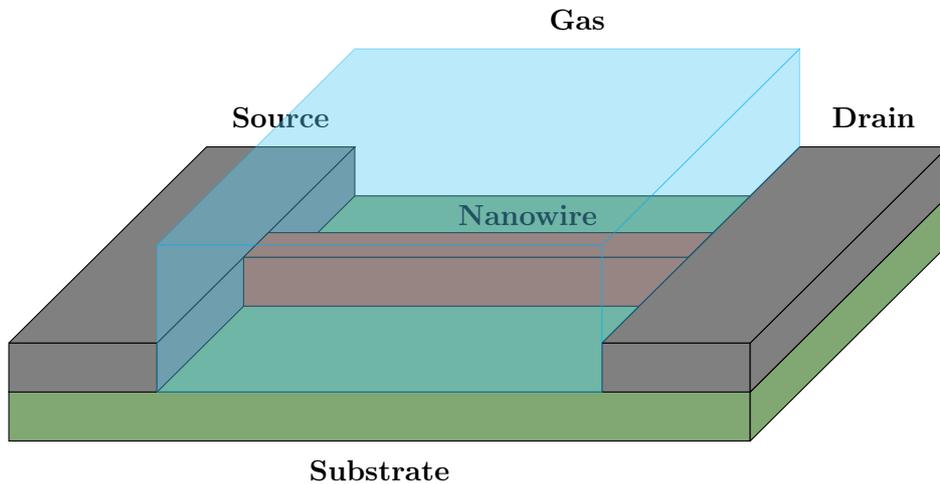
Figure 1.1: Sketch of a nanowire gas sensor structure. The image is not true to scale, in fact the nanowire can have a length of several μm and is just a few tens of nanometers thick (cf. Figure 1.2).

The implementation of semiconductors as conductometric gas sensors goes back to the findings of Heiland [43], Bielanski [14] and Seiyama [80]. By now, several subtypes have emerged. Thick film sensors are porous and yield a high surface-to-volume ratio, which increases sensitivity, but prohibits exact reproducability of the sensing layer. Thin film sensors are not that sensitive, but allow reproduction of the thin film. Moreover, they can easily be integrated into a variety of micro-sized devices (cf. [66, 109]), which lowers power consumption and enables mobile use. Finally, sensors based on single nanowires or nanowire networks have an extremely high surface-to-volume ratio and have single-crystalline sensing layers, which combines high sensitivity, reproducability and easy integration in small-size devices.

A large class of semiconductors used in the fabrication of nanowire gas sensors are metal oxides, since they meet all the requirements for mass production (simple manufacturing process and affordability) as well as for sensing properties like reliability and sensitivity. Prominent materials

used for this purpose include SnO_2 [17, 20, 21], ZnO [2, 101], TiO_2 [32], In_2O_3 [106], WO_3 [76] and CuO [58, 89], which have all been thoroughly investigated over the past decades. Thorough reviews on different materials, manufacturing processes and results are found in [4, 53, 83].

Several strategies have been followed to enhance selectivity of conductometric gas sensors. Doping of the implemented nanowires with different metals, which may enhance the response to certain target gases is an experimental approach. An array of differently doped nanowires may therefore not only enable distinction of different gases, but also increase the sensitivity of the system. As an example, doping of tin dioxide with copper [55], copper oxide [49], but also with noble metals like palladium [85] has been reported to give promising results. However, target gases can also be distinguished without modification of the nanowire sensors. Ponzoni et al. show the temperature dependence of a WO_3 sensor response towards NO_2, H_2S, CO and NH_3 [76], which is considerably different for each gas. In this manner, gases can be discriminated by pattern recognition.

The latter, heuristic, approach is further refined by developing a model for the interactions of the target gases with the nanowire surface. The crucial step is then to estimate numerical values for the parameters governing these reactions, and their dependence on temperature. With this information obtained, one can simulate the sensor behavior at arbitrary temperatures and for arbitrary target gas concentrations. Ding et al. [25] as well as Fort et al. [29, 30, 31] reported results with commercial thin film gas sensors.

In this work, we use this approach for nanowire gas sensor prototypes built by the group of Anton Köck (formerly Austrian Institute of Technology, now Materials Center Leoben), who implemented mainly SnO_2 and CuO sensors [17, 37, 88, 89]. We seek to confirm the reaction paths proposed in literature and estimate the governing parameters for different gases in order to predict the sensor behavior.
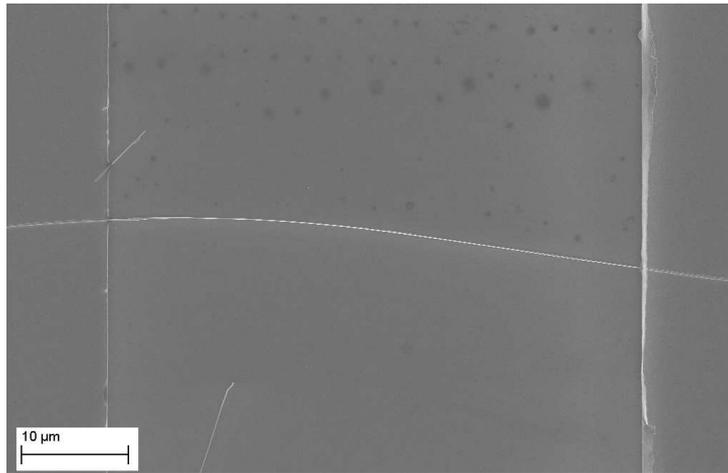
Figure 1.2: SEM image of a single SnO_2 nanowire as used in our experiments. The areas to the very left and right are the electrical contacts (Ti/Au). The nanowire is approximately 53 μm long.

1.1.1   Tin Dioxide (SnO$_2$) Sensors

Tin dioxide is a material widely used for gas sensing. In its pure stoichiometric form, it is an insulator due to its large bandgap of 3.6 eV. However, singly or doubly ionized oxygen vacancies form donor levels at 30 meV and 150 meV below the conduction band. At elevated temperatures, these electrons have enough energy to act as free electrons in the conduction band, which makes SnO$_2$ a semiconductor.

First SnO$_2$ based gas sensors were described for commercial use in the early 1970's by Taguchi's patents [70, 71], where, among others, detection of hydrogen, carbon monoxide, alcohol vapor and smoke is reported. In 1977, the detection of water vapour was reported [15]. Since then, mainly two types of sensors are employed. First, thin film sensors allow integration on microhotplates, which enables very small devices, but are less sensitive than thick film sensors due to their lower porosity. Several groups report detection of various gases with thin film sensors [73, 78, 82]. Second, nanowire based sensors have many advantages over thin film sensors, since they have a higher surface-to-volume ratio, show higher stability and yield lower power consumption [16]. Numerous publications discuss the sensing properties of, among others, CO, CO$_2$, H$_2$, H$_2$S, NH$_3$, SO$_2$ and ethanol, where also the use of noble catalysts has been shown to be useful [17, 20, 21, 46, 102] to enhance both sensitivity and selectivity. A review on concentration ranges and corresponding sensitivities for several target gases is given in [3].
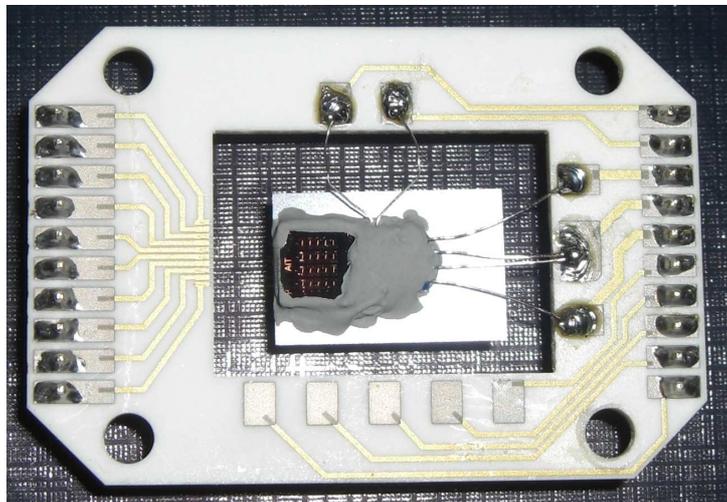
Figure 1.3: Image of an integrated sensor on the microchip. The whole device is not larger than approximately 2 cm.

A typical SnO$_2$ single nanowire as used in our experiments is shown in Figure 1.2. The areas to the very left and right are the electrical contacts. A real life image of the integrated sensor on the microchip is shown in Figure 1.3.

1.1.2   Copper Oxide (CuO) Sensors

Copper oxide is a p-type semiconducting material with a reported indirect bandgap between 1.2-2.1 eV [61, 69, 79], although even higher bandgaps have been reported for copper oxide nanoparticles [50].

Gas sensors based on this material are mainly built as nanowire devices, where single as well as network configurations are possible. For the nanowire fabrication, several techniques, e.g. thermal oxidation, electrochemical deposition or direct plasma oxidation methods are employed [28]. With these structures, detections of CO, H_2S, NO_2, NH_3 and ethanol were reported [51, 59, 60, 84, 105], but are not limited to these species. Detection ranges were reported in the low ppm range, for H_2S even in the range of tens of ppb.

As discussed previously, CuO is also widely used as dopant for gas sensors with other metal oxides as transducer materials, which greatly amplifies sensitivity and also the response to several gases, which is an important step towards selectivity.

We investigated the measurements conducted with CuO nanowire sensors in a network configuration for the analysis of fluctuations and noise depending on the gas species present in the measurement chamber.
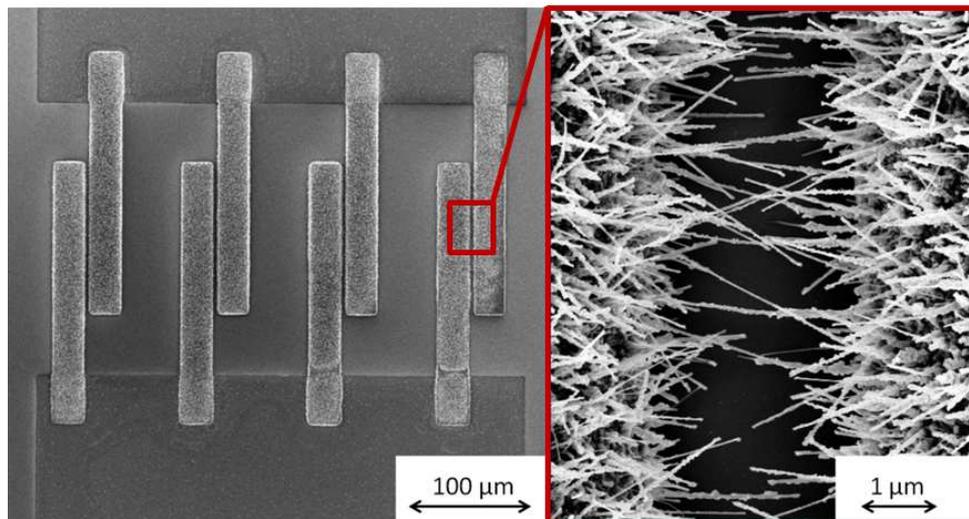
Figure 1.4: SEM image of a typical copper oxide nanowire network as used in our experiments.

A SEM image of a device used in our experiments is shown in Figure 1.4. In particular, the left part of the image shows several electrodes, which each have a nanowire network as shown in the right part of the image. For a thorough description of the used devices see [87, 88, 89].

1.2   Biosensors

The main aspect for the necessity of biomolecule detection is disease diagnosis. In order to employ this type of diagnosis for the general public a simple, fast and reliable method is necessary. In the past, many approaches have been followed to obtain suitable devices. For example, optical detection via fluorescence methods is well-studied, but its major drawback is the necessity of marking the target molecules prior to its detection (cf. [57]), which is of course a major inhibitor for mass production and use.

Another important group of methods for detection are electrochemical techniques, which have been shown to be even more sensitive. As there are many different techniques, we shall only consider BIOFET devices here.

This approach is a label-free, real-time method for detecting biomolecules by using nanowire sensors based on the *field effect*. This type of sensors, which is based on a principle reported by Bergveld [13], has first been presented by Cui et al. [22]. Since then, detection of various biomolecules, including proteins, nucleic acids and viruses have been demonstrated in aqueous solutions [26, 48, 74, 90, 108], especially in whole blood [91].
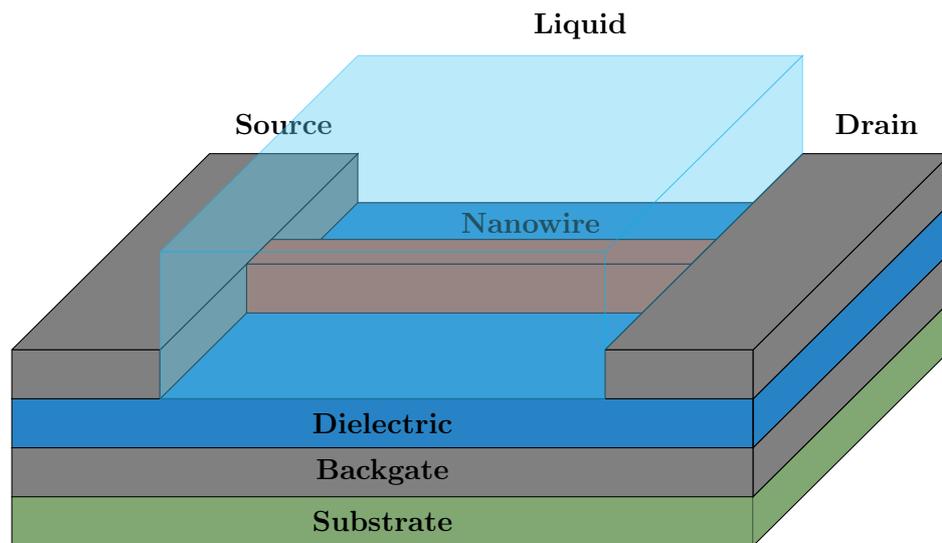
Figure 1.5: Sketch of a nanowire BIOFET structure. The working principle is that of a field-effect transistor with a backgate electrode. The functionalization is not shown here. Note the similarity to the structure of a nanowire gas sensors (cf. Figure 1.1).

Generally, field-effect transistors consist of a doped semiconductor that is contacted to three electrodes (*source*, *gate*, *drain*). The conductivity of the semiconductor is then modulated by the voltage applied to the gate electrode, which allows very sensitive regulation of the current through the semiconductor. Additionally, another *backgate* electrode can be implemented in order to increase sensitivity of the device.

For the detection of biomolecules, the gate electrode is replaced by a functionalized layer at the semiconductor surface. The functionalization consists of the receptor molecules for the intended

species to search for, such as antibodies for the detection of antigens or the matching single-stranded DNA for DNA detection. This layer is surrounded by an aqueous solution containing the target particles. If the matching molecules hybridize, the charge density at the surface is altered, which has the same effect on the nanowire as the gate electrode has. Note that since every receptor is only sensitive for the respective matching species, selectivity of this device comes for free.

A sketch of a typical biosensor structure is shown in Figure 1.5, where the functionalization of the surface is not depicted for simplicity. A cross-section depicting the receptor molecules is shown in Figure 3.2 later on. The most frequently used material for the transducer is silicon, but also metal oxides have been shown to be working (cf. [24]), while silicon oxide is mostly used as dielectric.

First steps have already been made in the description of biomolecule detection, where especially the fluctuations and hybridization-induced noise was investigated [18, 44]. This approach is continued in this work, where deeper insight behavior of the system is targeted. In particular, the prediction of sensor responses under the exposure to different target-molecule densities shall be investigated.

1.3   Remarks

Throughout the description of the working principles of both conductometric gas sensors and field-effect-based biosensors it becomes clear that the detection mechanism is very similar for both devices. Therefore, it seems natural that both mechanisms can be described by the same model. Its development and its implementation for simulations is the topic of the work at hand, where approaches on two different levels are considered.

First, we consider a deterministic model for the interaction processes at the transducer surfaces (cf. Chapter 2). This model needs to be coupled with an electrical conduction model in the case of gas sensors, or with a diffusion model in the case of biosensors to take all the relevant features of the system into account.

A refined approach including the random nature of chemical processes leads to a stochastic adsorption model (cf. Chapter 3), describing the density of adsorbed particles as stochastic processes. In these systems, the measureable data is obtained via the statistics of the stochastic processes, which can be calculated explicitly under several simplifying assumptions. If the latter ones are not suitable, numerical solutions are the best one can get.

The deterministic model is used for the determination of parameters governing the respective reactions (cf. Chapter 4). The gaseous species considered here include carbon monoxide, oxygen and hydrogen, while the hybridization of ssDNA oligomers will be investigated within the biosensors framework. These data obtained for the hybridization processes can then be utilized in the simulations of Chapter 5.

In Chapter 5, the stochastic description of the surface processes is first used to analyze experimental data from the detection of hydrogen sulfide and water vapor. A decomposition of the signal enables the distinction of situation where the gases are present from those where they are not. Second, two algorithms coupling the stochastic hybridization processes coupled to the

diffusion model were implemented in order to simulate sensor behavior under the influence of target molecules. Here, the focus is on the equilibrium values as well as on the evolution over time of the signal, the fluctuations, and the signal-to-noise ratio.

Chapter 2

Deterministic Detection Models

In order to be able to simulate the sensor response under the influence of the target, we need to rephrase the working principle of the device into mathematical terms. This step is called *modeling*. There, every step in the mechanism is described with a suitable approach and finally, all the different models are coupled to obtain the whole system describing a working sensor device. In this chapter, we will discuss the approaches used to model the underlying processes for the two sensors of interest. In each case, there are two steps to consider in order to obtain a realistic model.

There is no opportunity to observe the surface interactions at metal oxide gas sensors directly. Rather, these processes are only accessible via measurements of the conductivity of the transducer. As a consequence, the full gas sensor model combines an electrical conduction model for the nanowire with a surface interaction model, which allows deductions from measurement data. Here, the interactions of oxygen, carbon monoxide, hydrogen, hydrogen sulfide and water vapor are discussed.

Unlike as for gas sensors, there exist direct measurements of the binding processes of biomolecules to its receptors at nanowire biosensors, which allows straightforward investigation of the surface interactions. Therefore, the electrical conduction model for the nanowire is not necessary, although it would also be suitable to simulate the actual sensor response. However, especially when it comes to lower target-molecule concentrations, the transport through the surrounding liquid also needs to be taken into account. Therefore, the model for biosensors combines a transport equation for the target molecules in the liquid with the surface interactions to obtain a reliable description of biomolecule detection.

Note that a diffusion model is not necessary for gas sensors, since expecially at high temperatures the diffusion constant of a gas is large enough to consider the transport to be instantaneous.

In this chapter, we assume that there are large amounts of all the quantities involved and we are considering large timespans. This assumptions allow to neglect the random nature of all the chemical reactions and we can just consider the average values, which leads to a deterministic model.

In the following, we will first develop the specific description of gas detection (cf. Sections 2.1 and 2.2) and then continue with the coupled model for biosensing in Sections 2.3 and 2.4.

These derivations are based on the author's publications [96] and [98].

2.1   Conduction in the Metal Oxide

The principle of carrier transport in the nanowire strongly depends on several factors, where its geometry, in particular its thickness, and its morphology play the most important roles. For example, in poly-crystalline probes, the electrons need to overcome the electronic barriers at the many grain boundaries, while in single-crystalline probes these barriers are only present at the surfaces. Also, the donor density as well as relative permittivity and, apart from material properties, temperature have influence on the the decision which model to use, since they change the effect of the surface states on the whole nanowire behaviour.

The classical model for the carrier current in semiconduction materials is given by the drift-diffusion equations [64],

$$\nabla \cdot \vec{j}_n = R, \tag{2.1a}$$

$$\nabla \cdot \vec{j}_p = -R, \tag{2.1b}$$

$$\vec{j}_n = qn\mu_n\vec{E} + qD_n\nabla n, \tag{2.1c}$$

$$\vec{j}_p = qp\mu_p\vec{E} - qD_p\nabla p, \tag{2.1d}$$

where $\vec{j}_{n,p}$ denote the current densities, R denotes the recombination rate [81], $\mu_{n,p}$ are the mobilities and $D_{n,p}$ are the diffusion constants for electrons and holes, respectively, q denotes the electronic charge and $\vec{E}$ is the electric field. The respective first terms on the right hand side of the last two equations represent drift, while the respective last ones represent diffusion.

The electric field is derived from the solution of the *Poisson equation*,

$$-\nabla \cdot (\epsilon_0\epsilon_r\nabla V(\vec{x})) = \rho \tag{2.2}$$

with suitable boundary conditions, which relates derivatives of the electrical potential V to the charge density $\rho := q \cdot (p - n)$ in the nanowire and the permittivity of the material $\epsilon_0\epsilon_r$. Since the charge density is determined by the densities of electrons and holes, coupling of the Poisson equation to the drift-diffusion system is established. Typical boundary conditions are Dirichlet conditions at the Ohmic contacts (representing the applied voltage) and zero Neumann conditions everywhere else. The electric field is then given as the gradient of the potential,

$$\vec{E}(\vec{x}) = -\nabla V(\vec{x}). \tag{2.3}$$

In n-type sensors, there are no free holes present, while in p-type sensors, no free electrons are present, so two of the above equations always vanish. For the rest of this section, we shall only

consider n-type metal oxides. The derivation of the link between resistance of a p-type metal oxide and the surface states of the material is based on the same principles, although a little different in some details [1, 47].

Assuming that the depletion layer thickness is of comparable size with the mean free path, the current density mainly consists of the drift part. Therefore, dropping the diffusion term in (2.1) is a valid approximation, which greatly simplifies the calculations. Furthermore, assuming that the drop of the applied potential is uniform along the nanowire, it is sufficient to calculate the current through the nanowire at any cross-section via

$$I = \iint\limits_A \vec{j}_n^{\,\mathrm{drift}}\, \mathrm{d}\vec{x} = qE\mu_n \iint\limits_A n(\vec{x})\, \mathrm{d}\vec{x}, \tag{2.4}$$

where E is the electric field normal to the cross-section here. This approximation is called the *graded-channel approximation.*

We define the quantity σ to be the proportionality factor relating the electric field and the current density in the material, yielding

$$\sigma := q\mu_n n \tag{2.5}$$

for n-type sensors. This quantity is henceforth called *specific conductivity.* The total conductance for the whole sensor, which relates the electric field to the total current is then given by

$$G := \iint\limits_A \sigma\, \mathrm{d}\vec{x} = \bar{A}q\mu_n n_s, \tag{2.6}$$

where the last equation is derived from *potential barrier theory* [25, 68] and $\bar{A}$ is a constant taking into account the sensor geometry of the sensor. According to *potential barrier theory*, the conductance only depends on the density of electrons at the surface n_s, which in turn depends on the surface potential V_s,

$$n_s = N_D \exp\left(-\frac{qV_s}{k_B T}\right), \tag{2.7}$$

where N_D is the donor density in the metal oxide, k_B is the Boltzmann constant, and T is the temperature in Kelvin. The same theory also relates the total density of localized surface electrons to the surface potential via the Schottky relation [68],

$$V_s = -\frac{qN_{\mathrm{eff}}^2}{2\epsilon_0\epsilon_r N_D}, \tag{2.8}$$

where N_{eff} is the effective density of localized surface electrons.

Summarizing, the conductance of a nanowire is given by

$$\begin{aligned}
G &= \bar{A}q\mu N_D \exp\left(-\frac{qV_s}{k_B T}\right) = \bar{A}q\mu N_D \exp\left(-\frac{q^2 N_{\mathrm{eff}}^2}{2\epsilon_0\epsilon_r N_D k_B T}\right) = \\
&= G_0 T^{-\frac{3}{2}} \exp\left(-\frac{q^2 N_{\mathrm{eff}}^2}{2\epsilon_0\epsilon_r N_D k_B T}\right),
\end{aligned} \tag{2.9}$$

where we condensed all pre-exponential constants into one parameter G_0 and took into account that the mobility also depends on the temperature, $\mu \propto T^{-3/2}$. As can be seen from this formula, for a fixed geometry, material and temperature, the conductance varies with the effective density of surface states N_{eff}, so it is straightforward to seek for an expression for this quantity. A proper description of the processes taking place at the sensor surface, which will provide N_{eff}, is in order. This task is going to be one of the main goals of the work at hand.

2.2 Surface Processes for Gas Detection

As derived during the last section, surface processes do heavily influence the conductive behavior of the metal oxide, which is the crucial step in the sensing mechanism. The need for proper modelling of the adsorption and the desorption of gas molecules is an obvious consequence. However, this part of the sensor behavior is still open for discussion. On the one hand, several surface reactions are understood qualitatively under certain surrounding conditions, although there is some uncertainty when it comes to more complicated situations. This includes possible multiple steps in the processes and also their stoichiometry. As an example, Fort et al. [31] consider a two-step reaction mechanism for oxygen adsorption, where the first step is assumed to be much faster and therefore always to be in equilibrium. On the other hand, there is still great doubt on the quantitative results for the reaction constants that govern the surface processes. For example, Fort et al. [29] express their doubts about the accuracy of the obtained values.

As a consequence, one objective of the presented work is to confirm the reaction paths proposed in literature, and, moreover, obtain an estimation for the numerical values of the reaction-governing parameters.

A common model to describe the electronic behavior of a semiconductor surface is the *rigid band model*. Within this model, the interactions of the surface with any other species is described via localized electronic energy levels, the so called *surface states* [68]. These surface states have many different origins which also influence their density, and we are interested in two of them. First, there are intrinsic states that occur since the periodicity of the lattice is broken at the surface, which yields the named electronic behavior. Second, the adsorption of any species changes the electronic structure of the metal oxide near the surface, again yielding localized energy levels.

Free electrons in the conduction band of the metal oxide can occupy the surface states, which prevents them from contributing to the electrical conduction through the nanowire. The relation between occupied surface states and conduction is given by equation (2.9). In the following, any interaction of target gases with the surface is described in terms of surface state occupation.

2.2.1 Inert Conditions

If only inert gases like nitrogen (N_2) or noble gases (e.g. Ar) are surrounding the nanowire, there are no interactions with the surface. This is of course the most simple case, where only intrinsic surface states play a role. Here, some electrons in the conduction band are trapped in surface states and have built up a potential barrier at the surface so that the system of electrons is in an equilibrium. In this situation the number of occupied surfaces states can be influenced by varying the temperature. An increase provides more energy for the electrons and makes overcoming the

potential barrier more likely, which yields more trapped electrons in surface states. A decrease of the temperature yields a higher release rate from the surface states, which also decreases the potential barrier.
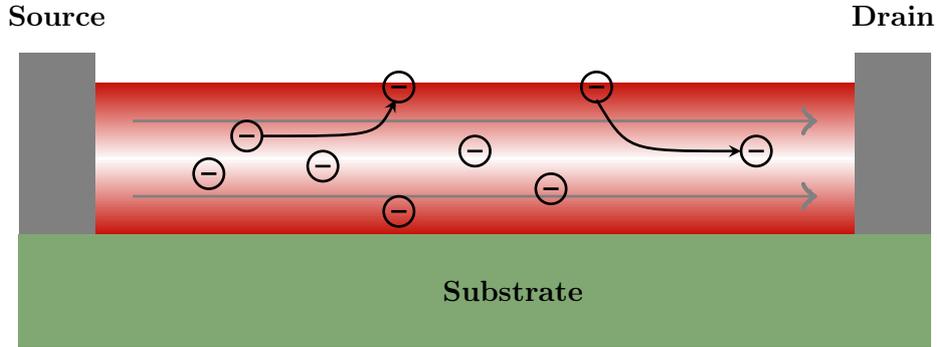
Figure 2.1: Trapping and releasing of electrons to and from intrinsic surface states.

The trapping and releasing of electrons in surface states can be described as a dynamic process. Experiments show [25] that this process is taking place in the range of minutes, which is very slow compared to typical time scales of electronic systems. The process can be written as a chemical reaction, yielding [31]

$$S_i + e^- \rightleftharpoons S_i^-, \tag{2.10}$$

where S_i, S_i^- denote an unoccupied and occupied intrinsic surface state, respectively. Figure 2.1 sketches these processes within the sketch of the whole device. Application of the mass action law allows to relate the change in the density of occupied surface states to its current value, to the density of surface electrons and to the total available density of surface states. This yields an ordinary differential equation, reading

$$\frac{\mathrm{d}N_i}{\mathrm{d}t} = k_1 n_e([S_i] - N_i) - k_2 N_i, \tag{2.11}$$

where N_i denotes the density of occupied intrinsic surface states, $[S_i]$ denotes the total density of available intrinsic surface states and k_1, k_2 are reaction constants. The first term on the right hand side represents the trapping rate, while the second one represents the releasing rate of electrons. For a given temperature, k_1 and k_2 are constant. The modelling of their temperature dependence will be discussed in Section 2.2.7. The quantity n_e represents the density of free electrons at the surface, i.e. those with enough energy to overcome the potential barrier. According to the discussion in Section 2.1, its value is given by

$$n_e := N_D \cdot \exp\left(-\frac{q^2 N_i^2}{2\epsilon_0 \epsilon_r N_D k_B T}\right), \tag{2.12}$$

Obviously, the exponential renders the differential equation nonlinear. The equation can also not be solved in closed form. To simulate the sensor behavior with given parameters, even here a numerical solution is the best we can get.

2.2.2 Oxygen

It is quite natural to investigate the interactions of oxygen with the sensor surface first, as its presence in real-life applications is unavoidable. Moreover, surface processes of oxygen come in handy under certain circumstances, since many target gases are detected via interaction with pre-adsorbed oxygen, as will be discussed in the respective sections.

The crucial parameter for oxygen adsorption is the temperature, as experiments indicate different mechanisms for different temperature ranges [5]. TPD chromatography in [104] shows that at temperatures below $150°C$ oxygen is adsorbed as O_2^-, while at temperatures between $150°C$ and $400°C$, the dominant species is O^-. Since the investigated measurements were all conducted within the latter temperature range, only the mechanism for the O^- processes will be discussed here.

Adsorption of oxygen takes place in two steps [25, 68]. First, oxygen molecules are chemisorbed to the surface, which creates an unoccupied surface state, henceforth referred to as extrinsic surface state, at the site of the adsorbed oxygen atom. Second, the oxygen atom is ionized via occupation of the extrinsic surface state, a process similar as described in Section 2.2.1. A scheme of the mechanism is shown in Figure 2.2.
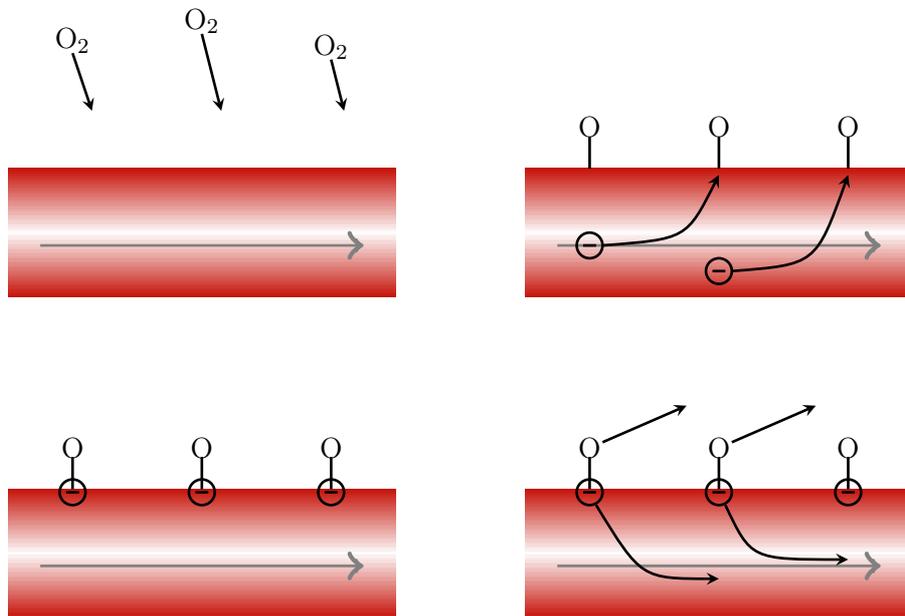
Figure 2.2: Mechanism of oxygen adsorption/desorption at SnO_2 surfaces. Upper left image: Oxygen reaches the surface and creates an extrinsic surface state. Upper right image: The extrinsic surface states are occupied by free electrons. Lower left image: Situation with occupied surface states. Lower right image: Oxygen is desorbed, electrons are released and contribute to conduction.

The reactions equations for this process are

$$\frac{1}{2}O_2 + S_e \rightleftharpoons S_O, \tag{2.13a}$$

$$S_O + e^- \rightleftharpoons S_O^-, \tag{2.13b}$$

where S_e denotes an available surface site, S_O and S_O^- denote unoccupied and occupied extrinsic surface states, respectively. The negative sign distinguishes unoccupied from occupied surface states and also indicates the type of its charge. Similarly to the intrinsic behavior, occupation of an oxygen surface state traps a free electron at the surface, preventing it from contributing to conduction through the sensor. In this two-step process, the first reaction has been shown to be much faster than the latter one [25]. Therefore, Fort et al. [29, 31] consider the chemisorption process to be always in its equilibrium, which yields a simplification of the investigated system. However, we will implement this process as stated above in order to still investigate the full system.

Again, application of the mass action law yields the following equations

$$\frac{dN_O}{dt} = k_3 \left[O_2\right]^{\frac{1}{2}} \left([S_e] - N_O - N_O^-\right) - k_4 N_O - \frac{dN_O^-}{dt}, \tag{2.14a}$$

$$\frac{dN_O^-}{dt} = k_5 n_e N_O - k_6 N_O^-, \tag{2.14b}$$

where $[S_e]$ denotes the total density of surface sites and N_O and N_O^- denote the densities of unoccupied and occupied extrinsic surface states, respectively. As the occupation of extrinsic surface states influences the potential barrier, the expression for the surface electron density changes, now yielding

$$n_e := N_D \cdot \exp\left(-\frac{q^2 \left(N_i + N_O^-\right)^2}{2\epsilon_0 \epsilon_r N_D k_B T}\right). \tag{2.15}$$

With oxygen present, this expression has to be used in (2.11) too, which establishes coupling between the two processes. Note that N_{eff} is now given by the sum of intrinsic and extrinsic surface states.

2.2.3   Carbon Monoxide

Carbon monoxide is a toxic gas that occurs, e.g., during incomplete combustion of fossil fuels. Monitoring its level is therefore not only important for personal safety, but also useful for optimization of combustion processes. The detection of carbon monoxide with nanowire gas sensors has been reported and discussed in, e.g. [52].

According to literature, there are several paths that have to be taken into account when considering CO detection. First, CO may adsorb directly to the SnO_2 surface via a mechanism quite similar to oxygen adsorption [38],

$$CO + S_e \rightleftharpoons S_{CO}, \tag{2.16a}$$

$$S_{CO} \rightleftharpoons S_{CO}^+ + e^-, \tag{2.16b}$$

where the notation used in previous sections has been adopted. Again, we have a chemisorption process followed by ionization. However, the important qualitative difference to oxygen adsorption is the opposite charge of the occupied surface states. In other words, occupation of a carbon monoxide surface state injects a free electron into the nanowire, which can then contribute to conduction in the metal oxide. Gases injecting electrons upon reacting with the surface are called *reducing* gases. The differential equations for the discussed process are

$$\frac{\mathrm{d}N_{\mathrm{CO}}}{\mathrm{d}t} = k_7 \left[\mathrm{CO}\right] \left([S_e] - N_{\mathrm{CO}} - N_{\mathrm{CO}}^+\right) - k_8 N_{\mathrm{CO}} - \frac{\mathrm{d}N_{\mathrm{CO}}^+}{\mathrm{d}t}, \tag{2.17a}$$

$$\frac{\mathrm{d}N_{\mathrm{CO}}^+}{\mathrm{d}t} = k_9 N_{\mathrm{CO}} - k_{10} n_e N_{\mathrm{CO}}^+, \tag{2.17b}$$

where here, the expression for n_e is

$$n_e := N_D \cdot \exp\left(-\frac{q^2 \left(N_i - N_{\mathrm{CO}}^+\right)^2}{2\epsilon_0 \epsilon_r N_D k_B T}\right). \tag{2.18}$$

The negative sign in the expression for N_{eff} is due to the opposite charge of intrinsic and carbon monoxide surface states, which yields a lower effective potential barrier than in the inert situation.

Second, carbon monoxide interacts with pre-adsorbed ionized oxygen. This reaction's product is gaseous carbon dioxide (CO_2), while the electron occupying the surface state is released and can contribute to conduction. Unlike the reactions discussed so far, this process is irreversible. The reaction equation reads

$$\mathrm{CO} + S_{\mathrm{O}}^- \rightarrow \mathrm{CO}_2 + e^- + S_e. \tag{2.19}$$

The last term in this equation indicates that a formerly occupied surface site has now become available.

2.2.4   Hydrogen

Hydrogen is a highly explosive gas that arises, for instance in various industrial processes. Moreover, it faces a future as favorable energy carrier [65] and rocket fuel [86]. All these situations make proper and effective monitoring of hydrogen indispensable.

Malyshev et al. [63] consider hydrogen detection with SnO_2 sensors under various conditions, including different temperatures, target gas concentrations, humidity levels and different catalysts. However, they propose a reaction mechanism only for temperatures higher than 350°C. A mechanism for lower temperatures involving dominant pre-adsorbed oxygen species is proposed by Gong et al. [36], which will be the one implemented for our studies and checked for validity. Other than in the case of carbon monoxide, hydrogen does not directly interact with the metal oxide surface, but only with pre-adsorbed oxygen.

The reaction path investigated is

$$\mathrm{H}_2 + S_{\mathrm{O}}^- \rightarrow \mathrm{H}_2\mathrm{O} + e^- + S_e, \tag{2.20}$$

which has to be combined with the equations of oxygen adsorption discussed in Section 2.2.2. The mechanism, which is again reversible, produces water vapour, a free electron in the nanowire

and an available chemisorption site. The corresponding ODE system is obtained by adding one term to the oxygen adsorption system,

$$\frac{\mathrm{d}N_\mathrm{O}}{\mathrm{d}t} = k_3 \left[\mathrm{O}_2\right]^{\frac{1}{2}} \left([S_e] - N_\mathrm{O} - N_\mathrm{O}^-\right) - k_4 N_\mathrm{O} - \frac{\mathrm{d}N_\mathrm{O}^-}{\mathrm{d}t}, \tag{2.21a}$$

$$\frac{\mathrm{d}N_\mathrm{O}^-}{\mathrm{d}t} = k_5 n_e N_\mathrm{O} - k_6 N_\mathrm{O}^- - k_{11} \left[H_2\right]^{\frac{1}{2}} N_\mathrm{O}^-, \tag{2.21b}$$

where the expression for n_e is the same as in equation (2.15), since hydrogen does not chemisorb directly to the surface.

Since during this reaction water vapor is produced, there could, theoretically speaking, also occur an interaction of H_2O with the surface. In our case, this fact will be neglected, which is justified by the specific setup of the measurement chamber and the low gas concentrations used in the respective experiments.

2.2.5 Hydrogen Sulfide

Hydrogen sulfide is a highly toxic gas that appears for example during putrefaction, but also during refinery of petroleum. Monitoring the hydrogen sulfide level is therefore crucial for the safety of the involved personnel. Detection of H_2S was, e.g., reported in [19].

At low concentrations, H_2S interacts with the pre-adsorbed oxygen forming water vapour and sulfur dioxide (SO_2). For n-type SnO_2 sensors at temperatures above 370°C, a mechansim involving doubly charged oxygen was proposed, yielding [62]

$$H_2S + 3S_\mathrm{O}^{2-} \rightarrow H_2O + SO_2 + 6e^- + 3S_e. \tag{2.22}$$

According to this reaction path, six electrons per reaction are injected into the metal oxide, which should make the device highly sensitive for H_2S detection.

For lower temperatures, a mechanism based on singly charged adsorbed oxygen was proposed for p-type CuO sensors [107],

$$H_2S + 3S_\mathrm{O}^- + 3h^+ \rightarrow H_2O + SO_2 + 3S_e, \tag{2.23}$$

where h^+ denotes a hole. Adaptation of this process for n-type sensors yields

$$H_2S + 3S_\mathrm{O}^- \rightarrow H_2O + SO_2 + 3e^- + 3S_e, \tag{2.24}$$

from which we obtain

$$\frac{\mathrm{d}N_\mathrm{O}}{\mathrm{d}t} = k_3 \left[\mathrm{O}_2\right]^{\frac{1}{2}} \left([S_e] - N_\mathrm{O} - N_\mathrm{O}^-\right) - k_4 N_\mathrm{O} - \frac{\mathrm{d}N_\mathrm{O}^-}{\mathrm{d}t}, \tag{2.25a}$$

$$\frac{\mathrm{d}N_\mathrm{O}^-}{\mathrm{d}t} = k_5 n_e N_\mathrm{O} - k_6 N_\mathrm{O}^- - k_{12} \left[H_2S\right] \left(N_\mathrm{O}^-\right)^3. \tag{2.25b}$$

This systems resembles equations (2.21), but has now another nonlinear term in the second equation.

However, especially at higher target gas concentrations, H_2S directly interacts with the surface by replacing lattice oxygen with sulfur, yielding

$$2H_2S + SnO_2 \rightleftharpoons 2H_2O + SnS_2 \tag{2.26}$$

for SnO_2 nanowires [62]. Although this process also severely alters the electrical behavior of the device and therefore allows gas detection in principle, this mechanism is beyond the capabilities of the model used in this work and cannot be considered here. As a consequence, only very low concentrations of H_2S will be investigated.

2.2.6 Humidity

Humidity, i.e. the presence of water vapour in the ambient air, crucially alters the conductive behavior of metal-oxide sensors. Due its presence almost everywhere in natural environments, it is an important step to better understand these alterations. However, the underlying mechanisms are very complicated and not yet confirmed for all situations, which prevents any exact studies in this work. Since we will only qualitatively investigate the effects of water vapour interactions on the noise level, we will just write down the reaction paths discussed in literature.

When considering SnO_2 sensors, two types of interaction seem possible. First, there is the interaction with lattice atoms [6],

$$H_2O + 2Sn_{lat} + O_{lat} \rightleftharpoons 2\,[Sn_{lat} - OH] + [O_{lat} - H]^+ + e^-. \tag{2.27}$$
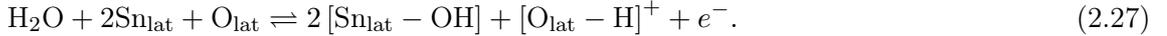
Second, there is interaction both with pre-adsorbed oxygen atoms and Sn lattice atoms, which yields [54]

$$H_2O + O^- + 2Sn \rightleftharpoons 2\,[Sn_{lat} - OH] + e^-. \tag{2.28}$$

For CuO sensors, a reaction model related to the one in equation (2.28) was proposed. Here, copper atoms from the lattice are involved [47],

$$H_2O + O^- + 2Cu + h^+ \rightleftharpoons 2\,[Cu_{lat} - OH] + S_e. \tag{2.29}$$

As already mentioned, these processes will not be investigated for the estimation of reaction parameters. Rather, the effect of humidity on the quality of the signal will be considered in Section 5.1, where it suffices to have an idea of what happens at the surface when water vapour is present.

2.2.7 Reaction Constants

For a given temperature, the k_i are constant. However, they vary with temperature. A widely used model to take this fact into account is the *Arrhenius form* [56], given by

$$k_i := \sigma_i \cdot \exp\left(-\frac{E_i}{k_B T}\right), \tag{2.30}$$

where $i \in \mathbb{N}$, κ_i is the frequency factor and E_i is the activation energy, which are both constant. The index here denotes the different reaction constant arising in all the mechanisms. Therefore,

for each reaction rate to determine, we have in fact two quantities to estimate, which doubles the overall number of unknown parameters stemming from reaction constants in the system when considering more than one temperature.

Moreover, since the activation energies arise within an exponential, the system depends on the parameters in a highly nonlinear way, which makes their estimation even more difficult.

2.2.8 Material Parameters

There are still two material parameters within the model that have not been discussed yet. In particular, the relative permittivity ϵ_r and the free donor density N_D require some attention. Most importantly, numerical values need to be chosen in order to perform the simulations. Since both parameters strongly depend on the manufacturing process, choosing the correct numerical values is not straightforward. However, since the results are not qualitatively influenced by any of the quantities, we chose some typical values, which are shown in Table 2.1.

Parameter	Numerical Value	Unit	Comment
q	1.602×10^{-19}	C	elementary charge
k_B	1.38×10^{-23}	$\mathrm{J\,K^{-1}}$	Boltzmann constant
T	–	K	temperature
ϵ_0	8.854×10^{-12}	$\mathrm{A\,s\,(V\,m)^{-1}}$	dielectric constant
ϵ_r	9.58	–	relative permittivity
N_D	6×10^{23}	$\mathrm{m^{-3}}$	free carrier concentration
$\mu_{n,p}$	–	$\mathrm{cm^2 (V\,s)^{-1}}$	mobility of electrons/holes
$D_{n,p}$	–	$\mathrm{cm^2\,s^{-1}}$	diffusion coefficient
$\vec{j}_{n,p}$	–	$\mathrm{A\,cm^{-2}}$	current density
$\vec{E}$	–	$\mathrm{V\,m^{-1}}$	electric field
σ	–	Ω^{-1}	conductivity
$\bar{A}$	–	–	geometric factor
G	–	Ω^{-1}	conductance
V_S	–	V	surface potential
σ_i	–	depends on reaction order	frequency factor
E_i	–	J	activation energy

Table 2.1: Used symbols and their numerical values for gas-sensor applications.

2.3 Surface Processes for Biosensing

The principle of detecting biomolecules at surfaces is resembling the one for gas adsorption in general, but has its differences in some details. Consider the surface of a nanowire biosensor. In order to detect biomolecules, it is functionalized with appropriate receptor (or *probe*) molecules.

Advantageously, one can control their surface density experimentally, which allows to fix this parameter in simulations. This functionalized surface is surrounded by an aqueous solution containing the matching target molecules. The dynamic process of binding and unbinding of the respective species, or hybridization and dissociation, again changes the surface charge density and hence the electrical characteristics of the nanowire, which allows detection of the binding processes in measurements. Since these surface processes do not involve any electron transfers with the semiconductor as it was the case for gas sensors, the reaction formulation is comparably simple in this case and written as

$$\mathbf{T} + \mathbf{P} \xrightarrow{r_a} \mathbf{PT}, \tag{2.31a}$$

$$\mathbf{PT} \xrightarrow{r_d} \mathbf{T} + \mathbf{P}, \tag{2.31b}$$

where $\mathbf{T}$ denotes a target molecule, $\mathbf{P}$ denotes a probe molecule and $\mathbf{PT}$ denotes a probe-target complex at the sensor surface. The two reaction constants are given by r_a and r_d, respectively. Since two compounds are necessary for hybridization, this reaction is of second order, while the dissociation is of first order. Biosensors usually are operated at constant temperatures, which is why we do not need to write them in the Arrhenius form.
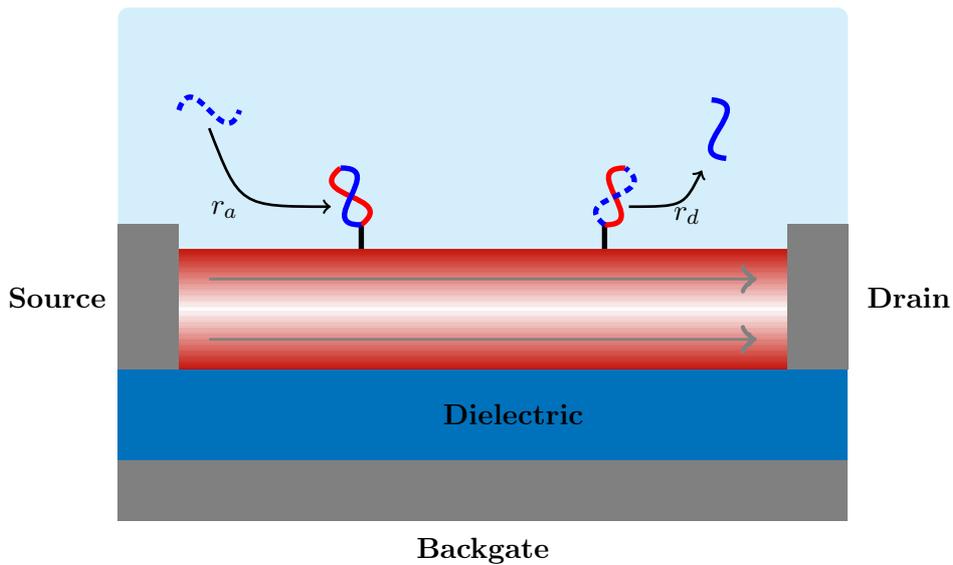
Figure 2.3: Investigated surface processes at silion nanowire sensors. The receptor molecules are shown in red, while the target molecules are shown in blue.

If there are large amounts of target as well as probe molecules present in the liquid and at the sensor surface, respectively, the effects caused by randomness of the chemical reactions is negligible. In this case, the mass action law allows a transformation of equations (2.31) into an ordinary differential equation for the density of probe-target complexes at the functionalized surface, yielding

$$\frac{\mathrm{d}\mathbf{PT}}{\mathrm{d}t}(t) = r_a C_T (C_P - \mathbf{PT}(t)) - r_d \mathbf{PT}(t) \tag{2.32a}$$

$$\mathbf{PT}(0) = 0, \tag{2.32b}$$

where C_T denotes the target-molecule concentration near the surface and C_P denotes the density of probe molecules at the surface. As we do not want to have any probe-target complexes present at the surface in the beginning of the simulation, we impose a zero initial condition for the system, which corresponds to a complex-free surface in the beginning of the simulation. Of course, other initial complex-densities can be implemented easily by setting the respective non-zero initial condition.

Considering the density of target molecules in the liquid as a reservoir, which means that the target-molecule concentration is constant no matter how many molecules are taken away, this equation has an analytic solution, which is given by

$$\mathbf{PT}(t) = \frac{r_a C_P C_T}{r_a C_T + r_d} \cdot \left(1 - e^{-(r_a C_T + r_d)t} \right) = \frac{\alpha}{\beta} \cdot \left(1 - e^{-\beta t} \right), \tag{2.33}$$

where we used the abbreviations

$$\alpha := r_a C_P C_T, \tag{2.34a}$$
$$\beta := r_a C_T + r_d. \tag{2.34b}$$

With this expression, the probe-target density can be computed explicitly for any time. Finally, the receptor density is known in this setting, which indeed leaves us just with two unknown parameters to determine in this situation.

Putting all this together, under the assumptions made to derive this model, parameter estimation is much simpler than for the gas-sensor case.

2.4   Diffusion of Biomolecules

For a realistic model of the surface processes at the nanowire, it is not sufficient to only consider the hybridization and dissociation processes assuming constant target-molecule concentration. Rather, one also needs to take into account the fact that with every target DNA hybridized with its matching receptor molecule, there are fewer molecules near the surface to interact and vice versa. However, if there is still DNA throughout the aqueous phase, there will be diffusion which transports the particles towards the surface and allows the continuation of the hybridization process.

Naturally, this process is modeled by the diffusion equation, which is given by

$$\frac{\partial u}{\partial t} = D\Delta u \quad \text{in } \Omega \times (0, t_{\text{end}}], \tag{2.35a}$$
$$\nu \cdot \nabla u = g \qquad \text{on } \partial\Omega \times (0, t_{\text{end}}], \tag{2.35b}$$
$$u(x, 0) = u_0 \qquad \text{in } \Omega. \tag{2.35c}$$

This is an equation for the density of target molecules $u(x,t)$, which is a time-dependent function. Here, Ω denotes the liquid domain surrounding the nanowire. In particular, the quantity needed for the surface processes is

$$C_T = C_T(t) = \frac{1}{\Omega_S} \int\limits_{\Omega_S} u(x,t)\mathrm{d}x, \tag{2.36}$$

which is the mean value of the target-molecule density near the surface. The parameter D is the diffusion constant of the investigated target molecules. To determine its numerical value, the single-stranded DNA molecules can be considered as rod-like according to Tirado et al. [92]. In this study, the macroscopic diffusion coefficient is given by

$$D = \frac{\gamma k_B T}{3\pi \eta L_{\mathrm{DNA}}}, \tag{2.37}$$

where γ is a correction factor taking into account so-called *end-effects*, which converges to a finite value for infinitely long rods, k_B is the Boltzmann constant, T is the temperature in Kelvin, η is the viscosity of the liquid, and L_{DNA} is the length of the DNA oligomer. In our numerical studies, we consider a setup described in the work by Peterson et al. [75], from which all necessary parameters are derived. The respective numerical values for these quantities are given in Table 2.2.

Parameter	Numerical Value	Units	Comment	Reference
γ	2.074	–	correction factor	[92]
k_B	1.38065×10^{-23}	$\mathrm{J\,K^{-1}}$	Boltzmann constant	–
T	298.15	K	temperature in Kelvin	[75]
η	9.719×10^{-4}	$\mathrm{N\,s\,m^{-2}}$	viscosity	[39]
L_{DNA}	10.5	nm	length of molecules	[75]
D	8.877×10^{-11}	$\mathrm{m^2\,s^{-1}}$	diffusion constant	(2.37)

Table 2.2: Parameters used for the computation of the diffusion constant.

The rod-like model relies, among others, on the strong influence of interactions between different parts, especially the two ends of the same molecule, which is mostly repulsive. Instead of this assumption, there is also a different approach. Considering these interactions to be weak, the DNA oligomer becomes more flexible, which is then referred to as *free-draining* model. In this case, the *Rouse* diffusion coefficient [77] is given by

$$D_{\mathrm{Rouse}} = \frac{k_B T}{6\pi \eta L_P}, \tag{2.38}$$

where L_P is the *persistence length* of the DNA. Tree et al. [93] estimated its value to be between 0.6 nm and 1.3 nm depending on the ionic strength of the solution, which yields 3.75×10^{-10} m^2/s

and 1.73×10^{-10} m^2/s as numerical values for the diffusion coefficients. However, since this approach yields the same order of magnitude for the diffusion coefficient and is still not perfectly confirmed, as has been pointed out in [93], the influence on the solution is not too large, and we employ the numerical value obtained in (2.37).

The function g setting the boundary condition in equation (2.35b) is defined such that at the boundary representing the device surface it gives the net balance of hybridization and dissociation processes, while there is no molecule flow at all the other boundaries. This is exactly the point where the surface interactions at the nanowire influence the diffusion throughout the liquid, which, together with equation (2.36) establishes the coupling of the system.

The initial condition given by equation (2.35c) allows to set up different situations for the beginning of the measurement. For example, one could consider a well stirred solution or imitate an injection of the target molecules at the very top of the liquid domain. Of course, the possible complexity of the scenario depends on the number of dimensions that are considered for this problem. This topic is investigated later on in this study.

2.5   Summary

The coupling of a widely used model for electrical transport through a metal-oxide nanowire to a surface-interaction model enables the investigation of adsorption processes at the transducers, especially the determination of reaction parameters. This will be the task in Chapter 4. In comparison, the hybridization processes at biosensors appear to be simpler, but for a full description, the diffusion of the target biomolecules needs to be taken into account.

Especially when it comes to low amounts of involved molecules, the randomness of all the reactions taking place cannot be neglected any longer, which is why a stochastic model for the ongoing processes is in order. This will be the topic of the next chapter.

Chapter 3

Stochastic Surface-Interaction Models

The signal of a sensor is never smooth. Rather, there are noise and fluctuations in the output, which is due to various effects. On the one hand, there are several factors in the measurement process, ranging from the power source to structural defects in the device, that make noise unavoidable. On the other hand, one important origin for fluctuations is the random nature of the reactions taking place at the sensor surface. In particular, the interaction of a target molecule with its receptor (which may be the nanowire surface itself or a respective receptor molecule) is random in space and time, i.e., the exact position where the molecule adsorbs and the exact time when this process happens are random. Since we cannot resolve the different positions at the nanowire surface for now, we will only focus on the time resolution here.

In this setting, the situation is as follows. The deterministic reaction rate approach discussed for the parameter estimation in the last chapter is only an approximation either for very large quantities of adsorption-desorption processes taking place at the same time or for large time intervals under investigation. Then, the reaction rate is given by the average of all the small time intervals. When considering low amounts of target molecules, this assumptions are not fulfilled, and therefore, there will always be some variation in the number of reactions happening within a fixed time interval. This is the origin of *biological noise* [40, 41, 42].

A sampling over many time intervals (with the system in the same state) will produce a mean value, which coincides with the numerical value of the reaction rates based derivations in the previous chapter. This fact will also be justified by the calculations in Section 3.2.

However, there is a lot of information to gather from the fluctuations, both in an absolute sense as well as regarding its value related to the mean value.

In this chapter, we will refine the deterministic model from the previous chapter to obtain a stochastic formulation of the surface processes. On the one hand, this approach together with

methods of signal decomposition will be used to understand and analyze the noise in gas-sensor measurements. On the other hand, this model together with the target-molecule diffusion model is used to simulate the hybridization processes at biosensor surfaces in Chapter 5.

The derivations on the topic of biosensors follow the author's publication [98], whereas the stochastic description of gas-sensor surface processes is based on [100].

3.1   Stochastic Formulation of the Surface Processes

To calculate the sensor behavior near the detection limit, it is necessary to look at very few molecules throughout the whole system. By doing so, the random nature of the surface processes cannot be neglected any more. It is therefore necessary to find a probabilistic formulation for the problem of interest. This can be done by considering adsorption as well as dissociation as independent stochastic processes. Therefore, the consideration of stochastic differential equations instead of ordinary differential equations is necessary. In particular, this approach yields a chemical Langevin equation and was thoroughly investigated by Gillespie ([33, 34, 35]). For thorough background information on stochastic differential equations, see [72].

Within this approach, the density of adsorbed (or hybridized) species becomes a stochastic process, which will generally be denoted as $\{\mathbf{X}_t\}_{t \in [0, t_{\mathrm{end}}]}$ here. In the case of gas-sensor adsorption, this quantity is a vector whenever extrinsic surface states are involved. This stochastic process is defined on a probability space $([0, \infty]^n, \mathcal{F}, \mathcal{P})$, where n is the total number of reaction paths, $\mathcal{F}$ is a σ-algebra on $[0, \infty]^n$ and $\mathcal{P}$ is a n-dimensional probability distribution.

The random variables $\boldsymbol{\omega}$ drawn from $[0, \infty]^n$ represent the number of reactions taking place within a certain time interval τ. For each reaction, this is a counting process, and hence, each component ω_i of $\boldsymbol{\omega}$ obeys a Poisson distribution with parameter λ_i,

$$\mathcal{P} = (\mathcal{P}_{\lambda_1}, \ldots, \mathcal{P}_{\lambda_n}). \tag{3.1}$$

The parameters λ_i depend on $\mathbf{X}_t$ and τ as they are given by the product of the respective reaction rate and the considered time interval,

$$\lambda_i(\mathbf{X}_t, \tau) = \tau \cdot k_i, \tag{3.2}$$

where the k_i represents reaction constants for biomolecule hybridization/dissociation as well as for gas-sensor adsorption/desorption.

By choosing τ large enough, one obtains large parameters λ_i. In this case, the Poisson distribution approximates a Gaussian distribution $\mathcal{N}(\mu_i, \sigma_i)$ with $\mu_i = \lambda_i$, $\sigma_i = \sqrt{\lambda_i}$ so that each index of a random variable $\boldsymbol{\omega}$ drawn from this distribution admits the form

$$\omega_i = \lambda_i(\mathbf{X}_t, \tau) + \sqrt{\lambda_i(\mathbf{X}_t, \tau)} \mathcal{N}(0, 1). \tag{3.3}$$

Altogether, by defining the matrix $\mathbf{M} = \{M_{i,j}\}_{i,j=1}^{n,m}$ for m involved species as

$$M_{i,j} = \begin{cases} l & \text{if reaction } i \text{ increases the density of species } j \text{ at surface by } l, \\ -l & \text{if reaction } i \text{ decreases the density of species } j \text{ at surface by } l, \end{cases} \tag{3.4}$$

the change in the state vector within a time interval τ is

$$\mathbf{X}_{t+\tau} - \mathbf{X}_t = \sum_{i=1}^{n} \mathbf{M}_i \omega_i, \tag{3.5}$$

where $\mathbf{X}_t$ is a m-dimensional vector.

Altogether, in the limit of $\tau \to 0$, equation (3.5) becomes a Langevin equation in white-noise form,

$$d\mathbf{X}_t = \sum_{i=1}^{n} \mathbf{M}_i \omega_i \, dt + \sum_{i=1}^{n} \mathbf{M}_i \sqrt{\omega_i} \, dB_i, \tag{3.6a}$$

$$\mathbf{X}_0 = 0, \tag{3.6b}$$

where dB_i are mutually independent standard *Wiener* processes. A Wiener process is a time-continuous stochastic process with independent, stationary and Gaussian-distributed increments. Note that if neglecting the stochastic terms in equation (3.6), one arrives exactly at the deterministic versions of the differential equations.

Apart from calculating a single outcome for such an equation, the investigation of its statistics is an important task where a lot of insight on the properties of the system is gained. Here, three quantities are of great interest.

- *Expected Value:* In our cases, the expected value represents the signal of the sensor or the measured quantity itself. It is given by

$$\mathbb{E}(\mathbf{X}_t) := \int_{[0,\infty]^n} \mathbf{X}_t(\omega) \, d\mathcal{P}(\omega). \tag{3.7}$$

- *Variance:* The variance corresponds to the fluctuations or the noise in the system and reads

$$\mathbb{V}(\mathbf{X}_t) = \int_{[0,\infty]^n} (\mathbf{X}_t(\omega) - \mathbb{E}(\mathbf{X}_t(\omega)))^2 \, d\mathcal{P}(\omega). \tag{3.8}$$

- *Signal-to-Noise Ratio:* The signal-to-noise ratio (SNR) is a very important parameter when considering the quality of any sensor. As indicated by its name, the SNR relates the measured signal and the fluctuations therein, which allows to determine the treshold for a signal to be distinguished from the noise of the device. As was stated above, the signal is related to the expected value, while the noise corresponds to the standard deviation of the random variable, yielding

$$\mathrm{SNR}(t) := \frac{\mathbb{E}(\mathbf{X}_t)}{\sqrt{\mathbb{V}(\mathbf{X}_t)}}. \tag{3.9}$$

  Note that the signal to noise ratio is a dimensionless quantity. As is clear from its definition, a large value for the SNR is always desired.

In the following we will consider the processes at both biosensors and gas sensors and calculate explicit solutions for the stochastic differential equations for biosensors under simplifying assumptions.

3.2   Stochastic Description of Processes at Biosensor Surfaces

The stochastic equations for biosensors are based on the deterministic model presented in Section 2.3. In this explicit case, we will denote the stochastic process by $\{\mathbf{PT}_t\}_{t\in[0,t_{\text{end}}]}$. The parameters governing the probability distribution are

$$\lambda_a(\mathbf{PT}_t, \tau) = \tau r_a C_T \left(C_P - \mathbf{PT}_t\right), \tag{3.10}$$
$$\lambda_d(\mathbf{PT}_t, \tau) = \tau r_d \mathbf{PT}_t. \tag{3.11}$$

Neglecting the fact that C_T is actually time-dependent, one obtains explicit expressions for the expected value, the variance and the signal-to-noise ratio of $\mathbf{PT}_t$. These quantities shall be derived in the following paragraphs.

3.2.1   Calculation of the Expected Value

The formula for the calculation of the expected value is given by equation (3.7). We therefore integrate on both sides of equations (3.6) to obtain

$$\begin{aligned}
\mathrm{d}\mathbb{E}(\mathbf{PT}_t) =\; & r_a C_T \left(C_P - \mathbb{E}(\mathbf{PT}_t)\right)\mathrm{d}t - r_d \mathbb{E}(\mathbf{PT}_t)\mathrm{d}t \\
& + \underbrace{\mathbb{E}(\sqrt{r_a C_T(C_P - \mathbf{PT}_t)}\mathrm{d}B_1)}_{=0} - \underbrace{\mathbb{E}(\sqrt{r_d \mathbf{PT}_t}\mathrm{d}B_2)}_{=0},
\end{aligned} \tag{3.12}$$

where the last two terms vanish because the expectancy of an $It\bar{o}$ integral is zero. Altogether, the equation simplifies to

$$\frac{\mathrm{d}\mathbb{E}\left(\mathbf{PT}_t\right)}{\mathrm{d}t} = r_a C_T \left(C_P - \mathbb{E}(\mathbf{PT}_t)\right) - r_d \mathbb{E}(\mathbf{PT}_t), \tag{3.13a}$$
$$\mathbb{E}\left(\mathbf{PT}_0\right) = 0. \tag{3.13b}$$

Obviously, the coefficients on the right hand side of this equation are exactly the same as in equation (2.32), which hence yields

$$E(t) := \mathbb{E}(\mathbf{PT}_t) = \frac{\alpha}{\beta}\left(1 - e^{-\beta t}\right). \tag{3.14}$$

The equivalence of equations (2.33) and (3.14) justifies the application of the simplified deterministic model to determine the reaction constants r_a and r_d later on in Section 4.2. In fact, the expected value of the stochastic differential equation always yields its deterministic version in the linear case.

3.2.2 Calculation of the Variance

The calculation of the variance is more involved, since it also necessary to calculate $\mathbb{E}\left(\mathbf{PT}_t^2\right)$. This quantity is computed by applying Itō's formula to $\mathbf{PT}_t^2$, yielding

$$\mathrm{d}\left(\mathbf{PT}_t^2\right) = 2\mathbf{PT}_t\,\mathrm{d}\mathbf{PT}_t + \mathrm{d}\mathbf{PT}_t\,\mathrm{d}\mathbf{PT}_t. \tag{3.15}$$

We obtain an equation in white-noise form by substituting the expression for $\mathrm{d}\mathbf{PT}_t$ from equation (3.6) and by using $\mathrm{d}B_i\,\mathrm{d}B_j = \delta_{ij}\mathrm{d}t$ as well as $\mathrm{d}t\,\mathrm{d}t = \mathrm{d}t\,\mathrm{d}B_i = \mathrm{d}B_i\,\mathrm{d}t = 0$,

$$\begin{aligned}
\mathrm{d}\left(\mathbf{PT}_t^2\right) = {}& \left(r_a C_T C_P + (2r_a C_T C_P - r_a C_T + r_d)\mathbf{PT}_t - 2(r_a C_T + r_d)\mathbf{PT}_t^2\right)\mathrm{d}t \\
& + 2\mathbf{PT}_t\left(\sqrt{r_a C_T(C_P - \mathbf{PT}_t)}\mathrm{d}B_1 - \sqrt{r_d \mathbf{PT}_t}\mathrm{d}B_2\right),
\end{aligned} \tag{3.16}$$

where several algebraic manipulations have been made. Again, application of the expected value and usage of the abbrevations defined in equations (2.34) yields

$$\begin{aligned}
\mathrm{d}\mathbb{E}(\mathbf{PT}_t^2) = {}& \alpha\mathrm{d}t + (2\alpha - r_a C_T + r_d)\mathbb{E}(\mathbf{PT}_t)\mathrm{d}t - 2\beta\mathbb{E}(\mathbf{PT}_t^2)\mathrm{d}t \\
& + \underbrace{\mathbb{E}\left(2\mathbf{PT}_t\sqrt{r_a C_T(C_P - \mathbf{PT}_t)}\mathrm{d}B_1\right)}_{=0} - \underbrace{\mathbb{E}\left(2\mathbf{PT}_t\sqrt{r_d \mathbf{PT}_t}\mathrm{d}B_2\right)}_{=0}
\end{aligned} \tag{3.17}$$

and therefore

$$\frac{\mathrm{d}\mathbb{E}(\mathbf{PT}_t^2)}{\mathrm{d}t} = \alpha + (2\alpha - r_a C_T + r_d)\frac{\alpha}{\beta}\left(1 - e^{-\beta t}\right) - 2\beta\mathbb{E}(\mathbf{PT}_t^2), \tag{3.18a}$$

$$\mathbb{E}\left(\mathbf{PT}_0^2\right) = 0, \tag{3.18b}$$

which is again a linear ordinary differential equation. Note that the time-dependent inhomogenity stems from the expression for the expected value derived in equation (3.14). Its solution is given by

$$\begin{aligned}
P(t) :={}& \mathbb{E}\left(\mathbf{PT}_t^2\right) \\
={}& \frac{\alpha}{\beta^2}\left(\alpha + r_d + (r_a C_T - 2\alpha - r_d)\,e^{-\beta t} + (\alpha - r_a C_T)\,e^{-2\beta t}\right).
\end{aligned} \tag{3.19}$$

Finally, the variance of $\mathbf{PT}_t$ is calculated from equations (3.14) and (3.19), yielding

$$\begin{aligned}
\mathbb{V}(\mathbf{PT}_t) = {}& \mathbb{E}(\mathbf{PT}_t^2) - \mathbb{E}(\mathbf{PT}_t)^2 = P(t) - E(t)^2 \\
={}& \frac{\alpha}{\beta^2}\left(r_d + (r_a C_T - r_d)\,e^{-\beta t} - r_a C_T e^{-2\beta t}\right) \\
={}& \frac{\alpha}{\beta^2}(1 - e^{-\beta t})(r_d + r_a C_T e^{-\beta t}).
\end{aligned} \tag{3.20}$$

This last result can also be derived via binomial statistics, where the event to consider is the number of binding processes at a certain time. The parameter governing this statistics is then

$$p(t) := \frac{E(t)}{C_P}, \tag{3.21}$$

which yields

$$\mathbb{V}(\mathbf{PT}_t) = C_P p(t)(1 - p(t)) = \frac{\alpha}{\beta^2}(1 - e^{-\beta t})(r_d + r_a C_T e^{-\beta t}). \tag{3.22}$$

This is the same result as equation (3.20).

3.2.3 Signal-to-Noise Ratio

We can now utilize the results obtained in the last two sections to find an expression for the signal-to-noise ratio under the discussed assumptions. Using equations (3.14) and (3.20), we obtain

$$\mathrm{SNR}(t) = \sqrt{\alpha}\frac{1 - e^{-\beta t}}{\sqrt{(1 - e^{-\beta t})(r_d + r_a C_T e^{-\beta t})}}. \tag{3.23}$$

Note that the SNR has a finite value as $t \to \infty$,

$$\lim_{t \to \infty}(\mathrm{SNR}(t)) = \sqrt{\frac{C_P C_T r_a}{r_d}}. \tag{3.24}$$

3.3 Stochastic Description of Surface Processes at Gas Sensors

Let us now turn to the more complicated situation of systems of nonlinear differential equations as they arise in the gas-sensors setting. In particular, we will consider the stochastic formulation for H_2S adsorption to CuO sensors here. The respective system of deterministic differential equations was presented in Section 2.2.5. The corresponding stochastic differential equation reads

$$d\mathbf{X}_t = \sum_{i=1,\dots,6,12} \mathbf{M}_i \omega_i dt + \sum_{i=1,\dots,6,12} \mathbf{M}_i \sqrt{\omega_i} dB_i, \tag{3.25}$$

$$\mathbf{X}_0 = \bar{\mathbf{X}}, \tag{3.26}$$

where (cf. equation (2.25))

$$\begin{aligned}
\lambda_1(\mathbf{X}_t, \tau) &= \tau k_1 n_e([S_i] - N_i), & \mathbf{M}_1 &= [1, 0, 0, 0], \\
\lambda_2(\mathbf{X}_t, \tau) &= \tau k_2 N_i, & \mathbf{M}_2 &= [-1, 0, 0, 0], \\
\lambda_3(\mathbf{X}_t, \tau) &= \tau k_3 n_e([S_e] - N_O - N_O^-)[O]^{1/2}, & \mathbf{M}_3 &= [0, 1, 0, 0], \\
\lambda_4(\mathbf{X}_t, \tau) &= \tau k_4 N_O, & \mathbf{M}_4 &= [0, -1, 0, 0], \\
\lambda_5(\mathbf{X}_t, \tau) &= \tau k_5 n_e N_O, & \mathbf{M}_5 &= [0, -1, 1, 0], \\
\lambda_6(\mathbf{X}_t, \tau) &= \tau k_6 N_O^-, & \mathbf{M}_6 &= [0, 1, -1, 0], \\
\lambda_{12}(\mathbf{X}_t, \tau) &= \tau k_{12}(N_O^-)^3[H_2S], & \mathbf{M}_{12} &= [0, 0, -3, 0],
\end{aligned}$$

and the respective expressions for n_e (cf. equation (2.12)) and k_i (cf. equation (2.30)) discussed earlier apply.

Obviously, this system is very complicated. In this work, we want to focus on the following very simple deduction. The more sources of noise we have, i.e. the higher the dimension of the probability space is, the larger the variance of the signal will be. This feature will be investigated later on in Section 5.1.

3.4 Algorithms for Reaction-Diffusion Systems

We turn now back to the biosensor setting. In this section, we focus on the calculation of solutions for reaction-diffusion systems as we encounter them in the case of biosensors. To obtain numerical data for the investigated problem, we implemented two different algorithms. The first, box-based, algorithm is very simple and does not require the exact position of the target molecules within the liquid domain. As easy as this approach is in one dimension, as cumbersome its extension to higher dimensions gets, which is why another, random-walk based, approach was also implemented. Here, the positions of all the particles at the current time is stored and all the desired quantities are computed from this data.

As a first step, one can just consider a one-dimensional domain, which corresponds to investigating a uniform geometry parallel to plane the nanowire surface. The advantage here is the shorter calculation times. Nevertheless, many useful insights can be obtained already from this setup.

However, the implementation of a two-dimensional domain allows to investigate a specific sensor geometry and to discriminate between the nanowire and the wafer on which the transducer is put. Of course, here one considers a cross-section perpendicular to the orientation of the nanowire. On the one hand, this setup enables the study of the effects of the surrounding wafer on the nanowire. On the other hand, much more complicated (especially more realistic) geometries and initial conditions can be implemented.

Since it is valid to assume that the whole device is uniform along the nanowire, the implementation of a three-dimensional system is not necessary, since everything can be computed on a cross-section of the device.
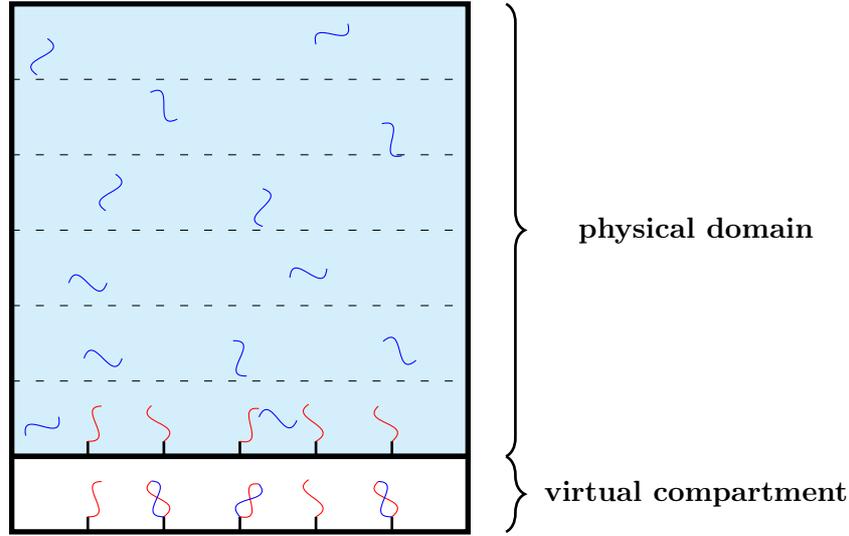
3.4.1 Box-Based Approach

The following description of this algorithm is limited to the one-dimensional case for simplicity. An extension to higher dimensions is possible, but cumbersome.

The idea of this approach is to divide the whole liquid domain in several compartments and to just consider the number of particles therein, not their exact position. Diffusion is therefore the transition of a particle from one box to an adjacent one, where the transition probability corresponds to the diffusion constant, the number of particles and the time interval looked at. In particular, we denote the probability that a particle from box i moves to its left or right neighbour by $\sigma_i = \mathbf{T}_i D / l^2$, where $\mathbf{T}_i$ is the number of target molecules in the compartment i and l is the height of the compartment. In order to include the chemical reactions at the surface, a further, virtual, compartment is added, which can only be accessed from the compartment representing

the area next to the nanowire surface. Here, the transition probabilities include the hybridization and dissociation frequencies, respectively, and are given by $\sigma_N = \mathbf{T}_N D/l^2 + r_a \mathbf{T}_N (\mathbf{P} - \mathbf{PT})$ and $\sigma_{N+1} = r_d \mathbf{PT}$, where $\mathbf{P}$ is the total number of probe molecules at the nanowire surface. The quantity σ_N takes into account that from box N diffusion to box $N-1$ occurs, while the transition to box $N + 1$ takes place just by hybridization.

A sketch of the domain is shown in Figure 3.1 where the physical as well as the virtual compartments are indicated.

Figure 3.1: Sketch of the domain in one dimension for the box-based approach. The virtual compartment at the very bottom represents the hybridized **PT** complexes. Target molecules are shown in blue, probe molecules are shown in red.

Algorithm 1. *(Box-Based Algorithm, based on [27])*

1. *Initialize the boxes according to the given initial data.*

2. *Calculate the timestep according to*

$$\tau = \frac{1}{\sigma_0} \log\left(\frac{1}{\xi_1}\right), \tag{3.27}$$

   where $\sigma_0 = \sum_{i=1}^{N} \sigma_i + \sum_{i=2}^{N+1} \sigma_i$ and $\xi_1 \in \mathcal{U}([0,1])$.

3. *Determine the two boxes involved in the transition from a drawn random variable $\xi_2 \in \mathcal{U}([0,1])$.*

4. *Update the number of particles in the respective boxes.*

5. *Unless the final time is reached, go to Step 2.*

A simple implementation of Step 3 is done by considering the transition from box i to either box $i-1$ or box $i+1$ as different reactions. From that, one obtains a discrete cumulated probability distribution function, which allows choosing a certain transition corresponding to a drawn random variable.

Clearly, the advantage of this algorithm is its very simple implementation and its low memory requirements compared to a random-walk approach. However, there is a drawback when considering large amounts of molecules or high reaction frequencies. Since in Step 2 the calculated τ is the time until the next reaction occurs, one obtains very small steps for the aforementioned cases, which results in longer durations for the simulations.

This algorithm was implemented within the *MATLAB* environment.

3.4.2   Random-Walk Approach

Facing the drawbacks when it comes to large amounts of molecules and the awkwardness at higher dimensions, an algorithm based on random walks was also implemented.

Here, the particles move around in the liquid domain according to their diffusion constants and drawn random variables, and if they are close enough to the surface, there is a chance that hybridization occurs. This event is also determined via a random variable, as is the dissociation of already hybridized **PT** complexes.

The advantage here is also the easily implementable possibility to distinguish different parts of the nanowire surface as well as the wafer surface on which the transducer is put. This yields the chance to compute the effects arising from complicated, though realistic, initial conditions. A sketch of the domain is shown in Figure 3.2, where a possible partition of the surface is shown with dotted lines.

Also, the size of the time steps is fixed here and can be chosen much larger than in the box-based approach, which also yields much faster computing times.

The algorithm presented in the following is based on the one by Erban et al. [27], who proposed a one-dimensional version of it.

Algorithm 2. *(Random-Walk Algorithm, based on [27])*

1. *Initialize the positions of the molecules according to given initial data.*

2. *Move each particle in the liquid according to*

$$X_i(t + \tau) = X_i(t) + \sqrt{2D\tau}\xi_1, \tag{3.28}$$

   where X_i denotes the coordinates of the i-th particle and $\xi_1 \in \mathcal{N}(0,1)^n$, where n is the dimension of the physical domain.

3. *Check if all moved particles are inside the liquid domain. If not, reflect from the respective boundaries, until they are in the liquid domain.*

4. *For every particle near enough to the surface, draw a random variable $\xi_2 \in \mathcal{U}([0,1])$. If*

$$\xi_2 \leq r_a \boldsymbol{T}(\boldsymbol{P} - \boldsymbol{PT})\tau, \tag{3.29}$$
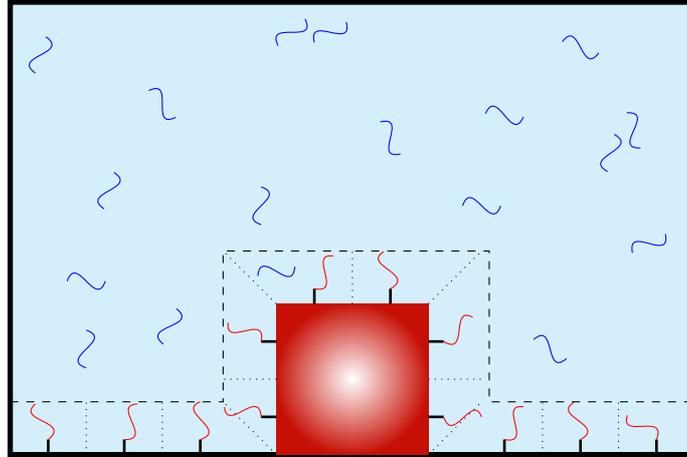
Figure 3.2: Sketch of the domain in two dimensions for the random-walk approach. The surface is divided into several domains, which allows the calculation of **PT** densities at different positions, and enables analysis of complicated initial conditions. The dashed line represents the maximum distance where hybridization is possible. The dotted lines show the partitions of the surface.

consider the particle hybridized at the corresponding part of the surface.

5. *For every particle hybridized at the surface at time t, draw a random variable ξ_3. If*

$$\xi_3 \leq r_d \boldsymbol{PT} \tau, \tag{3.30}$$

put the particle back into the liquid domain by drawing random variables for its position in the corresponding area near the surface.

6. *Unless the final time is reached, go to Step 2.*

To perform Step 4, one needs to define what actually is meant by particles near the surface. In fact, this quantity should correspond to the distance between a target and its receptor at which they hybridize. In our experiments, we consider this length to be 25 nm, which is about the length of two ssDNA strands considered here in line.

For scientific computations, this algorithm was implemented within the *Julia* environment, where a two-dimensional domain was considered. As the sensor is uniform along the third axis, the third dimension does not need to be included into the model.

In order to compare the random-walk-based algorithm to the box-based algorithm, a one-dimensional version was also implemented within the *MATLAB* environment. It turned out that the random-walk approach is approximately five times faster than the box-based algorithm. This is mainly due to the fact that for the random-walk algorithm, one can choose a larger τ, which reduces the number of steps necessary for each realization.

3.4.3 Sampling and Parallelization

Every execution of the discussed algorithms realizes one possible evolution of the system. To obtain the statistics for the parameters of interest, several thousands of iterations have to be calculated. The most important quantities to observe are the expected value and the variance of the **PT** complexes at the surface, but also waiting times until a certain amount of **PT** complexes has built might be of interest.

In order to speed up computations, parallelization of the whole task is appropriate. Advantageously, every realization is independent of each other, which enables a distribution of the single evaluations to different cores and to sample the quantities of interest directly. This procedure can be implemented in a straightforward manner by using *parfor*-loops instead of *for*-loops within *MATLAB*, or by using the *@parallel* macro within *Julia*, and yields the expected speed-up.

3.5 Wavelet Decomposition of a Signal

Transforming a signal is a very important technique to obtain information hidden in the measured stream of numbers. This procedure is widely used throughout engineering, where its most popular representative is *Fourier transformation*. This enables the calculation of a frequency spectrum of a periodic signal, which in turn allows the identification of sources of noise.

Unfortunately, since the basis functions used in Fourier analysis are periodic and therefore non-local, this technique gives only useful results for a stationary signal, which means a constant environment around the nanowire in this application. It is not possible to resolve local frequency changes. Since the core feature of the investigated measurements are changing environments and, consequently, pulsed signals, one has to come up with a different method. What is additionally needed here, is a time-localization of frequencies in the signal. An obvious approach is to use local functions, i.e. functions with compact support, for that.

The basic idea of wavelet analysis is to consider a certain basis function in L^2, a so called *mother wavelet*, that admits certain properties, which are defined via so called *filter coefficients* and a *scaling function*. By rescaling and shifting this function, one obtains an orthogonal basis that enables the decomposition of a signal. Similar to Fourier transform, for a wavelet function $\psi \in$ L$^2(\mathbb{R})$ the wavelet transform of a function $f : \mathbb{R} \to \mathbb{R}$ is given by

$$(Wf)(a,b) := \frac{1}{\sqrt{a}} \int_{\mathbb{R}} f(x)\psi\left(\frac{x-b}{a}\right)\,\mathrm{d}x, \tag{3.31}$$

where $a \in \mathbb{R}$ is the scale factor and $b \in \mathbb{R}$ is the translation.

After first mentioning of wavelets in the Appendix of *Haar*'s thesis, several types such as *Meyer* wavelets [67] or *Daubechies* wavelets [23] have been developed, where most of them have been derived according to necessary properties for a certain application. In this work, we will use two different types of Daubechies wavelets. One of these is shown in Figure 3.3 together with its scaling function.

The discrete wavelet transform resembles a fast Fourier transform. It is a linear transformation and can therefore be represented as a matrix multiplication, where the matrix entries correspond

(a) Scaling function
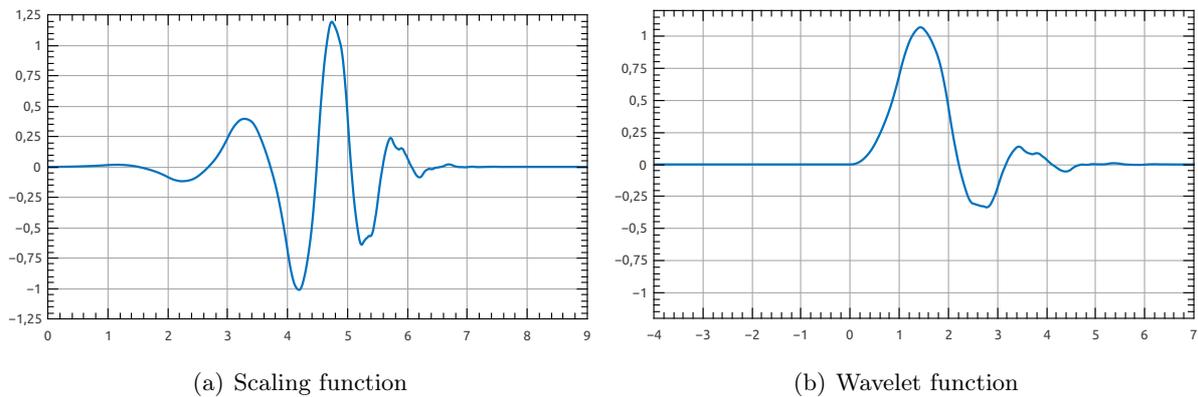
(b) Wavelet function

Figure 3.3: Scaling function and wavelet function for the investigated Daubechies wavelet of order 5.
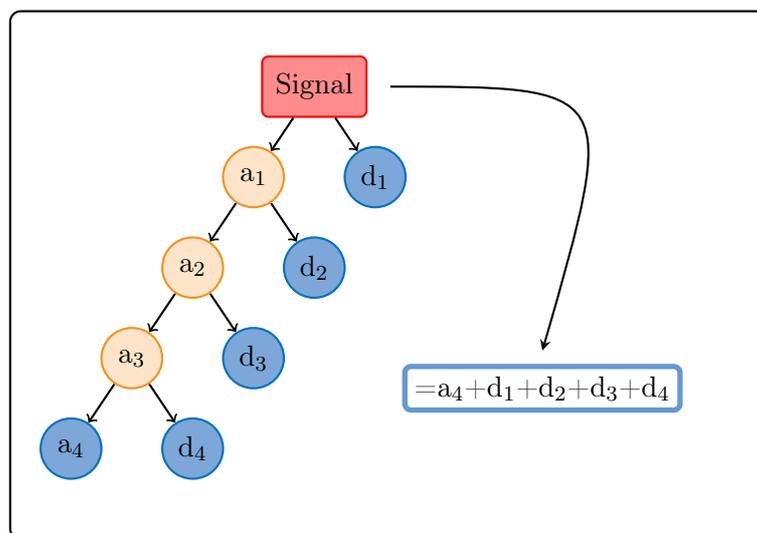
Figure 3.4: Scheme of the decomposition of a signal. The whole information is contained in all the detail coefficients d_1, d_2, d_3, d_4 and the final average coefficient a_4.

to the filter coefficients of the chosen wavelet family. In the matrix, the filter coefficients in each row are arranged in such a way that the signal vector is divided into two parts, where the first one contains an averaged signal, while the second one contains the detail information. The same procedure can be applied several to the remaining average part, again yielding an average and a detail part. This way, one obtains a hierarchy of decompositions that contains all the information. A scheme of this procedure is shown in Figure 3.4.

This procedure will be employed to obtain information on the noise in the sensor signal in Section 5.1.

3.6   Summary

The deterministic approach followed in Chapter 2 was refined to obtain a description based on the random nature of chemical reactions. These findings, together with the presented algorithms for reaction-diffusion system can be utilized to obtain numerical results on the sensor behavior. The respective simulations will be presented in Chapter 5.

Moreover, the concept of signal decomposition presented here will be employed to obtain information on a gas-sensor signal without the numerical knowledge of reaction parameters, since this method allows a deduction just based on the statistics governing the stochastic differential equations.

Determination of Model Parameters of Surface-Interaction Processes

The estimation of parameters arising as coefficients in systems of ordinary differential equations is quite a delicate task. Even in the simplest case of one linear differential equation, when there exists an analytical solution, fluctuations in the signal might lead to considerably different numerical values for the parameters. Fortunately, the experimental data for biosensor hybridization has a very low noise level, which leads to trustworthy results (cf. Section 4.2).

Of course, the situation is worse if the system is nonlinear itself and depends nonlinearly on the parameters as is the case for all the systems corresponding to gas-sensor operation. To remedy these difficulties in this situation, there are several steps that are of help. First, a proper scaling of the equations is in order, which is discussed in Section 4.3. Furthermore, we will estimate the parameters step by step if possible. The procedure begins with estimating the parameters for the trapping and releasing of the intrinsic surface states from experiments conducted under nitrogen or argon atmosphere. Next, the equations arising from the addition of one species are considered, while the already obtained parameters are used. One continues this way until all species of interest are added and all the parameters are determined.

Unfortunately, this protocol cannot always be applied, since on the one hand not all nanowire materials work properly under inert conditions, and on the other hand, measurements are not always available for the investigated setup.

The results presented in Sections 4.5 and 4.6 stem from a stepwise estimation process, while the results in Section 4.7 are obtained from an overall estimation procedure.

The material discussed in Sections 4.3-4.6 was published in [96]. The findings of Section 4.7 are based on [97] and [95], while the discussion of the error norms (cf. Section 4.8) were presented

in [94].

4.1 Determination Procedure

The determination of the the numerical values of the respective parameters was performed within the *Mathematica* environment. In particular, the simulated sensor behavior was implemented as a function of its parameters, which could then be compared to the measured data. For this task, which was to find the minimum in the difference between simulation and measurement with respect to the declared norm, a global optimization routine was employed. A discussion on the matter which norm to use is presented in Section 4.8.

The *Mathematica* environment provides several minimization methods with its package for global optimization. These include *differential evolution*, *Nelder-Mead* or *simulated annealing*. In this study, the best results were obtained by using the latter method.

4.2 DNA Hybridization

We now consider the determination of numerical values for the reaction rates of the surface processes r_a and r_d. For the adsorption of ssDNA with different probe densities at the nanowire surface, Peterson et al. [75] measured hybridization efficiency over time. We used least-squares optimization to obtain the desired values from their data. The results are shown in Table 4.1. The simulated adsorption efficiency based on those values is compared to the experimental data in Figure 4.1. Since the agreement is very good, the model for the investigated processes is suitable.

molecules/cm^2	assoc. rate r_a	dissoc. rate r_d
2×10^{12}	3933	0.0016
3×10^{12}	4071	0.0042
5.2×10^{12}	1014	0.0019
9.5×10^{12}	861	0.0037
12×10^{12}	348	0.0027

Table 4.1: Reaction parameters for DNA hybridization. The very left column gives the different probe densities.

The association rate values indicate two different regimes. Until a probe density of 3×10^{12} molecules/cm^2, the rate is almost constant, while it is considerably lower for all higher probe densities and even further decreases with increasing probe density. This can be explained in the following way.

Since DNA molecules carry charges, they repel each other if the distance between them becomes too small. A high probe density means a low distance between different probe molecules at the surface and hence lower distances between target molecules near the surface. As a consequence,
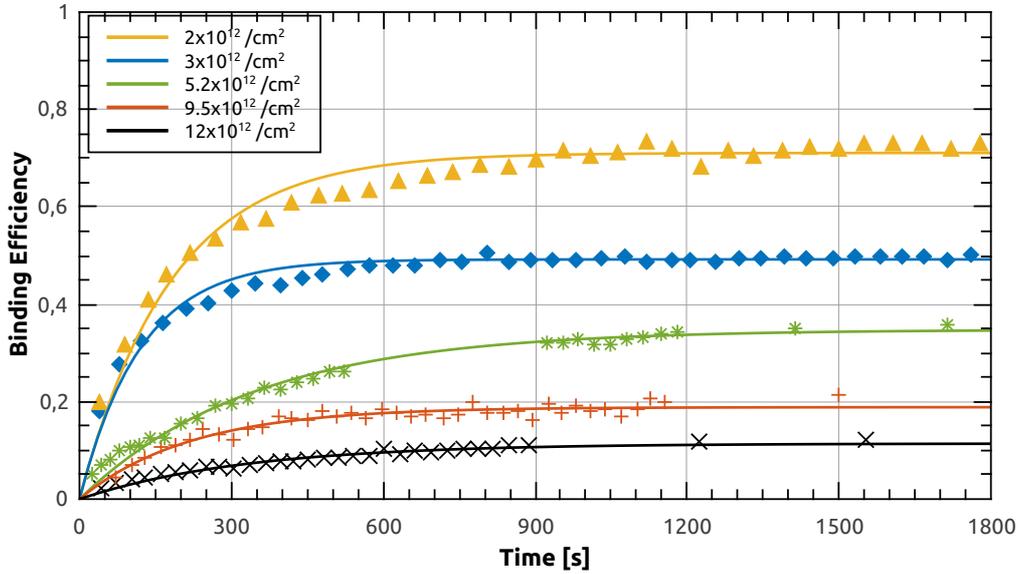
Figure 4.1: Experimental data from [75] (points) and simulated curves with the calculated parameters (lines). The parameters reflect the decreasing binding efficiency with increasing probe density.

mutual repulsion as well as sterical hindrance effects impede hybridization which yields lower binding rates. Meanwhile, the dissociation of probe-target complexes is not influenced by mutual repulsion. Altogether, as hybridization is slower for higher probe densities while dissociation rates do not change, a lower binding efficiency is obtained at the equilibrium for increasing probe density. A graphical representation of the numerical values of the reaction rates is shown in Figure 4.2.

The values obtained in this section will be employed to conduct various simulations depending on parameters such as geometry, target-molecule concentration or initial conditions in Chapter 5. The simulations are performed in one as well as in two dimensions. This is sufficient, since the nanowire and its surrounding liquid domain are uniform with respect to the axis parallel to the nanowire, which allows to omit this dimension. Therefore, we can avoid a three-dimensional simulation, which is favorable regarding complexity of the code as well as regarding calculation times.

4.3   Scaling

We now continue with the investigation of gas-sensor experiments and the determination of the respective parameters. The numerical values of all the quantities used in the model are different by many orders of magnitude, which leads to serious trouble during the task of parameter estimation. To remedy this drawback scaling of the equations is necessary. While Fort et al. [29, 31] employ a scaling procedure yielding a minimal number of extra constants in the system, we will follow an approach yielding dimensionless quantities. Normalized quantities will
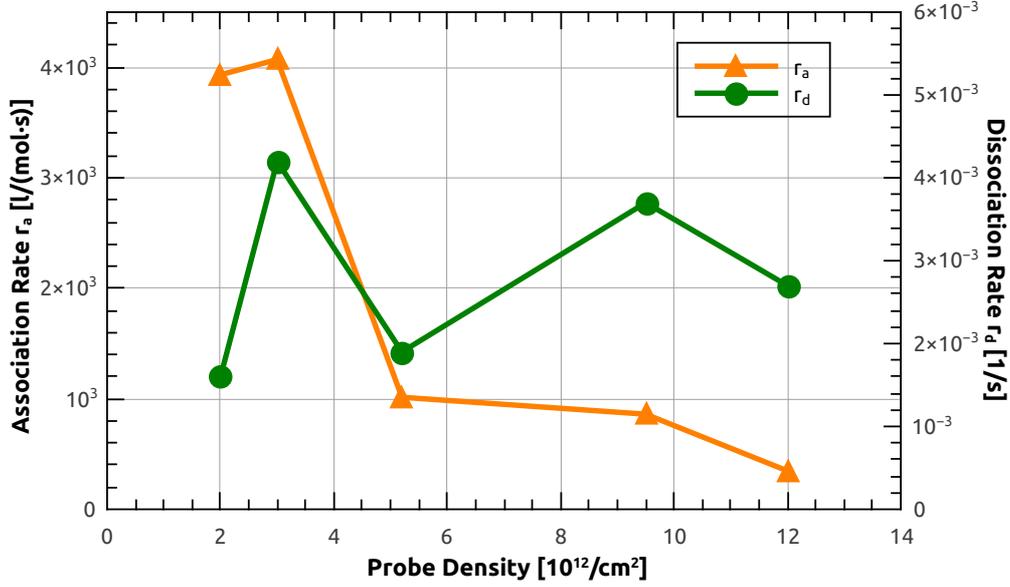
Figure 4.2: Reaction parameters versus probe-molecule density. For higher probe densities, the hybridization rate decreases significantly.

be denoted by a tilde over the variable in this work, and are obtained via

$$\widetilde{N}_\alpha^{(-,+)} = N_\alpha^{(-,+)} \cdot N_D^{-2/3} \qquad \widetilde{S}_\beta^{(-)} = S_\beta^{(-)} \cdot N_D^{-2/3} \qquad \widetilde{T} = T \cdot \frac{\epsilon_0 k_B}{q^2 N_D^{1/3}}, \qquad (4.1)$$

where $\alpha \in \{i,O,CO\}$ and $\beta \in \{i,e\}$. The superscripted signs in bracket indicate that both charged and uncharged quantities are meant here.

Together with this approach, we also condense fixed parameters within the unknown parameters. To avoid confusion if a parameter includes condensed parameters, we also change the notation for the reaction constants, yielding

$$\bar{\kappa}_i = \kappa_i \cdot \exp\left(-\frac{\lambda_i}{\widetilde{T}}\right) \qquad (4.2)$$

for the condensed quantities. With this procedure, we arrive at dimensionless quantities with simplified notation. The exact form of the equations to work with will be presented in the respective results sections for the different situations.

4.4 Estimation of G_0

When linking the measured conductance to the surface-state density, it is necessary to know all parameters arising in equation (2.9). The best way to do so is by determing the pre-exponential factor G_0 from the measurement. The procedure for that is explained in what follows.

It is of great help here that the surface-state variation is quite slow. Therefore, exposing the sensor to fast temperature changes, i.e. in the range of a few seconds, allows to consider the surface-state

density constant throughout heating or cooling periods. Application of the logarithm on both sides of equation (2.9) yields

$$\log G + \frac{3}{2}\log T = \log G_0 - \frac{q^2 N_S^2}{2\epsilon_0 \epsilon N_D k_B T} =: \log G_0 - \frac{\bar{C}}{T}, \tag{4.3}$$

where the left hand side is taken from the experiment and the right hand side represents a linear relationship between the data and T^{-1}. A linear fitting procedure gives the value for G_0.
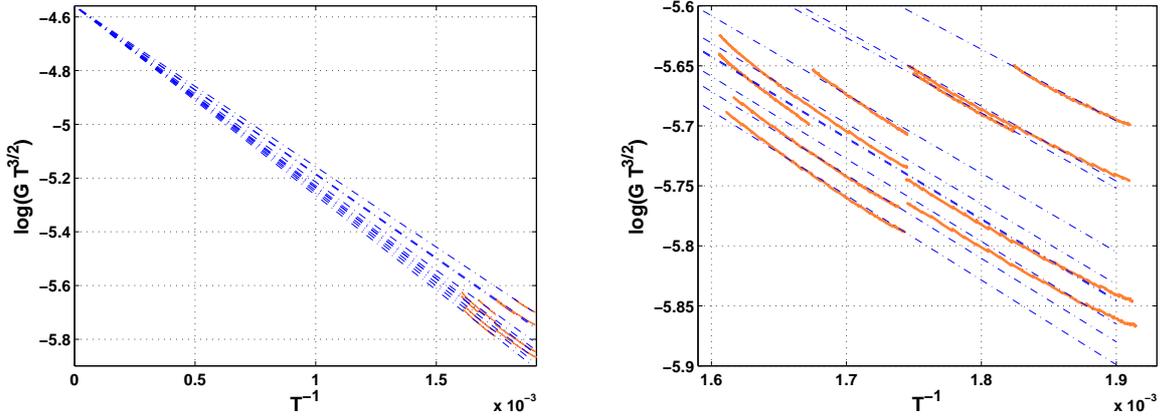
Figure 4.3: Fitting for the parameter G_0. The experimental data is shown in orange, the fitted curve is shown in dashed blue. The left image shows determination of G_0 at $T^{-1} = 0$, the right image shows a close-up view of the fitting of the experimental data.

This procedure is ideally conducted over a large temperature change. In our case, we only have small temperature changes (25-50°C), but several of these, and at different start and end points. Of course, in every situation the parameter $\bar{C}$ is going to be different, but G_0 always has to be the same, which yields $N + 1$ parameters for N temperature changes in the fit.

The resulting curves are shown in Figure 4.3. The right image shows the quality of the fit, while the left image shows the obtained numerical value, which is $G_0 = 1.047 \pm 0.0096 \times 10^{-2}\,\text{S}$. This value was then used to calculate the density of surface states for the parameter estimations for nitrogen and carbon monoxide atmospheres. Note that this value is only valid for the investigated device and also just for the measurements carried out during a short period of time before and after the discussed estimation experiment. The reason to the first restriction is the influence of the exact geometry on the conductive behavior, which is of course different for every device. The second restriction is due to the fact that with time, the electronic state of the nanowire might change due to many reasons like aging or oxidation.

With the calibration of the conduction model done, we are now ready to investigate the sensor behavior under exposure to different gases.

The measurements discussed in the following sections were conducted with single SnO_2 nanowire sensors, where the results on inert atmosphere and carbon monoxide even belong to the same

experiment (and therefore, of course, to the same sensor), while a different sensor was used for the hydrogen experiments as well as for the discussion on the error notion.

Information on the manufacturing process of the devices used in these experiments is given in [16, 17].

4.5 Inert Atmosphere

The sensor behavior in nitrogen atmosphere was investigated at 250, 275, 300, 325 and 350°C according to the temperature profile shown in Figure 4.4. The measurement indicates that the variation of the intrinsic surface states is very slow (time constants of tens of minutes), as was also reported in [25, 30].
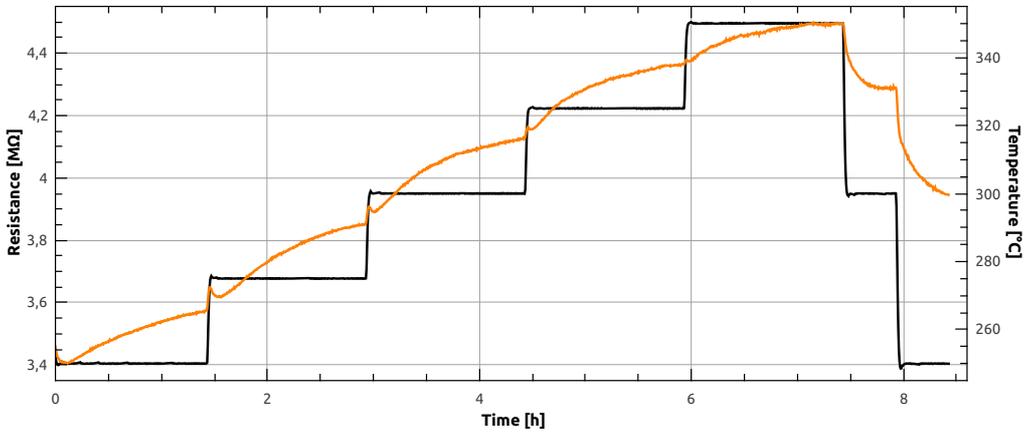
Figure 4.4: Measured resistance (orange, aligned with left y-axis) and temperature (black, aligned with right y-axis) profile in pure nitrogen atmosphere.

The scaled and dimensionless differential equation in this case is based on equation (2.11) and yields

$$\frac{\mathrm{d}\widetilde{N}_i}{\mathrm{d}t} = \kappa_1 \exp\left(-\frac{\lambda_1}{\widetilde{T}}\right) \exp\left(-\frac{\widetilde{N}_i^2}{2\epsilon_r\widetilde{T}}\right)(\widetilde{S}_i - \widetilde{N}_i) - \kappa_2 \exp\left(-\frac{\lambda_2}{\widetilde{T}}\right)\widetilde{N}_i, \tag{4.4}$$

where κ_1, κ_2, λ_1, λ_2 and $\widetilde{S}_i$ are the parameters to be determined.

As can be seen from the temperature profile, two temperatures have been considered twice, where the sensor was once heated and once cooled to that temperature. Surprisingly, the process velocity is quite different in those two cases, which is reflected in the fact that no parameter set could be found to agree with the signal in both situations. Due to this discovery, one parameter set was determined for the situation of heating, and one set was determined for cooling. Both of them are listed in Table 4.2.

The comparison of the best estimate to the measured data is shown in Figure 4.5. The timescales until recovery indicate that the equilibration during cooling is much faster than during the heating

Parameter	Heating Phase	Cooling Phase
κ_1	23.765	140.15
κ_2	0.0655	0.0279
λ_1	0.3501	0.3150
λ_2	0.7289	0.1764
$\widetilde{S}_i$	0.8855	0.9176

Table 4.2: Estimated parameters for the processes under inert conditions during heating and cooling.

phase, although still in the range of tens of minutes. This feature is also reflected in the values for the frequency factor κ_1, which is larger for the cooling period. Nevertheless, this finding might be exploited in real-life applications, in particular when it comes to time-saving measurement strategies.

(a) Heating Phase   (b) Cooling Phase
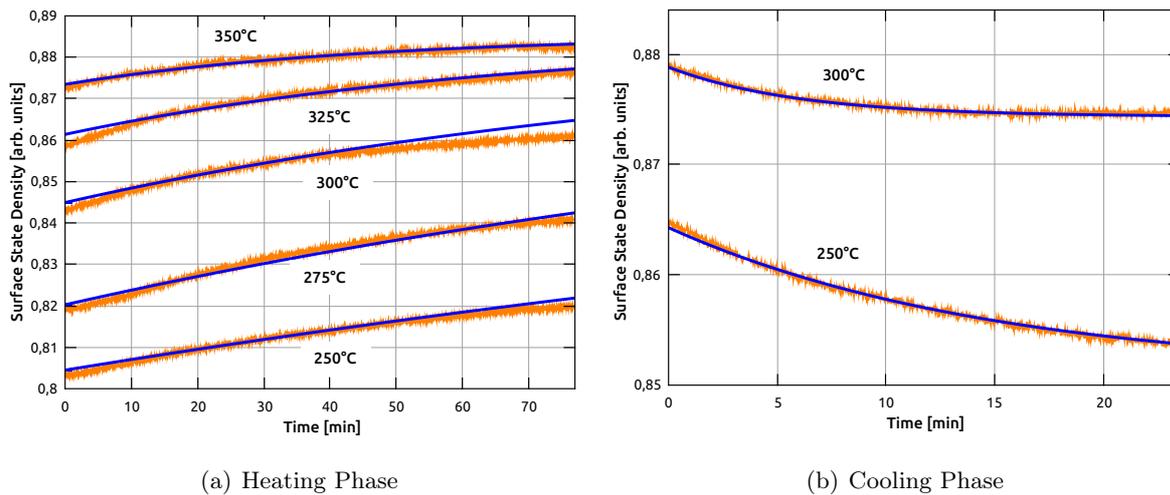
Figure 4.5: Comparison of the best estimates for pure nitrogen atmosphere to the experimental data during heating and cooling. The blue curve represents the simulation, while the orange curve represents the experimental data.

It is also worth noting that except for 350°C during the heating phase, the equilibrium is never reached, which also complicates the parameter determination.

4.6   Carbon Monoxide

The experiment discussed in the last section was continued with a measurement of carbon monoxide pulses at different temperatures. Here a concentration of 50 ppm carbon monoxide in dry nitrogen was considered, where two pulses of 15 minutes each were applied at temperatures of 300°C and 350°C, respectively (see Figure 4.6). After each pulse, 15 minutes of recovery time
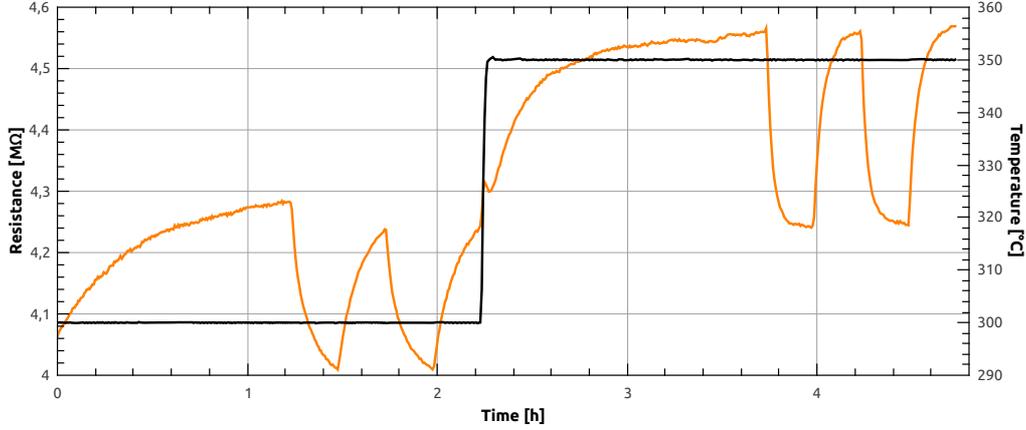
Figure 4.6: Measured resistance (orange, aligned with left *y*-axis) and temperature (black, aligned with right *y*-axis) profile for the carbon monoxide measurement.

have been scheduled.

Parameter	Numerical Value
κ_7	2.9192×10^2
κ_8	1.6136×10^9
κ_9	1.0678×10^{18}
κ_{10}	8.503×10^9
λ_7	0.2932
λ_8	0.8271
λ_9	1.4551
λ_{10}	0.8448
$\widetilde{S}_e$	72.411

Table 4.3: Estimated parameters for the adsorption process of carbon monoxide in nitrogen atmosphere.

Now, the full scaled and dimensionless system reads

$$\frac{\mathrm{d}\widetilde{N}_i}{\mathrm{d}t} = \kappa_1 \exp\left(-\frac{\lambda_1}{\widetilde{T}}\right) \exp\left(-\frac{(\widetilde{N}_i - \widetilde{N}_{\mathrm{CO}}^+)^2}{2\epsilon_r \widetilde{T}}\right) (\widetilde{S}_i - \widetilde{N}_i) - \kappa_2 \exp\left(-\frac{\lambda_2}{\widetilde{T}}\right) \widetilde{N}_i, \tag{4.5a}$$

$$\frac{\mathrm{d}\widetilde{N}_{\mathrm{CO}}}{\mathrm{d}t} = \kappa_7 \exp\left(-\frac{\lambda_7}{\widetilde{T}}\right) [\mathrm{CO}] \left(\widetilde{S}_e - \widetilde{N}_{\mathrm{CO}} - \widetilde{N}_{\mathrm{CO}}^+\right) - \kappa_8 \exp\left(-\frac{\lambda_8}{\widetilde{T}}\right) \widetilde{N}_{\mathrm{CO}} - \frac{\mathrm{d}\widetilde{N}_{\mathrm{CO}}^+}{\mathrm{d}t}, \tag{4.5b}$$

$$\frac{\mathrm{d}\widetilde{N}_{\mathrm{CO}}^+}{\mathrm{d}t} = \kappa_9 \exp\left(-\frac{\lambda_9}{\widetilde{T}}\right) \widetilde{N}_{\mathrm{CO}} - \kappa_{10} \exp\left(-\frac{\lambda_{10}}{\widetilde{T}}\right) \exp\left(-\frac{(\widetilde{N}_i - \widetilde{N}_{\mathrm{CO}}^+)^2}{2\epsilon_r \widetilde{T}}\right) \widetilde{N}_{\mathrm{CO}}^+, \tag{4.5c}$$

where the parameters of the first equation have already been considered in the previous section. Since the carbon monoxide adsorption experiment was conducted shortly thereafter, the obtained

numerical values for those parameters are assumed to be still valid and were included as known parameters into the system. Hence, the number of parameters to determine at once decreases to nine. The newly obtained parameter values are shown in Table 4.3. Obviously, the frequency factors are much higher than those for the intrinsic surface-state occupation, which means that the response of the sensor is much faster. This fact can also be qualitatively derived from the experimental data, see Figure 4.7. Furthermore, the adsorption process appears to be much faster at higher temperatures, which is also reflected in a comparably high value of the scaled activation energy λ_9.

(a) 300°C   (b) 350°C
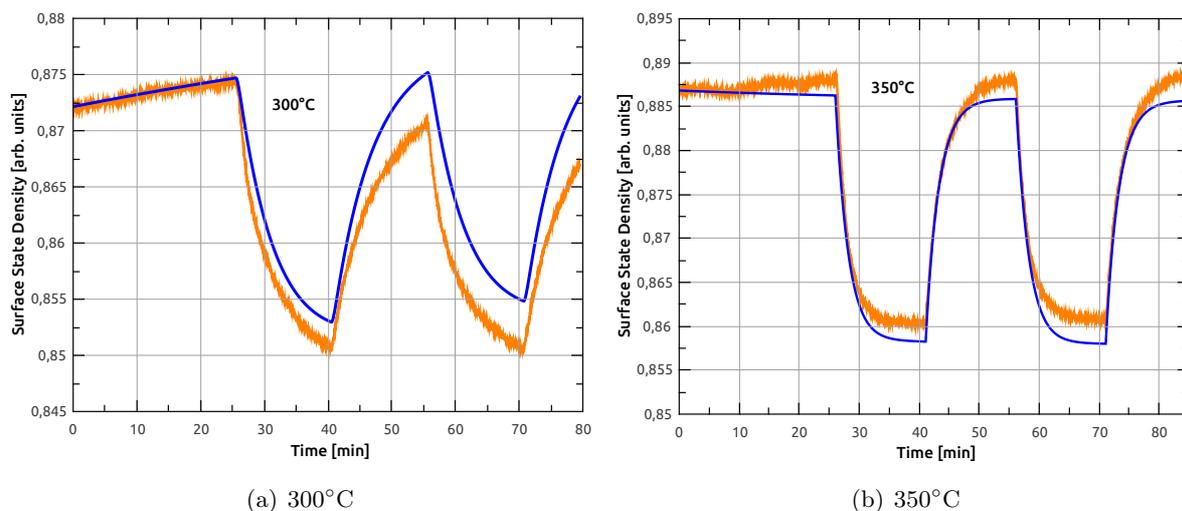
Figure 4.7: Comparison of the simulation with the best parameter estimates for the carbon monoxide pulses to the experimental data at 300°C and 350°C. Blue curve: simulation; orange curve: experimental data.

Figure 4.7 shows the comparison of the best estimates with the experimental data at both temperatures. At 350°C, the difference is small enough to be negligible, whereas at 300°C, there is a small deviation of the numerical solution from the signal. This might be due to the fact, that during the application of the gas pulses, the sensor signal is not yet stable, but still shows a drift based on the intrinsic reactions. This of course makes the parameter estimation more difficult. Nevertheless, the maximal difference between measurement and simulation is smaller than 1%.

4.7 Hydrogen

Measurements of hydrogen adsorption were only considered at one temperature. On the one hand, this simplifies the parameter determination, since we do not need to employ the Arrhenius form for reaction rates, but on the other hand, we do not gain any information on temperature dependence.

Experiments with hydrogen pulses were performed in dry air (80% N_2, 20% O_2). However, for the sensor used during these measurements, no data is available for the inert environment situation. Therefore, it was necessary to estimate the parameters for the intrinsic surface state occupation

as well as the oxygen adsorption processes at the same time. The remaining parameter $\bar{\kappa}_{11}$ for the hydrogen pulses is then derived in a second step.

The scaled system under investigation reads

$$\frac{\mathrm{d}\widetilde{N}_i}{\mathrm{d}t} = \bar{\kappa}_1 \exp\left(-\frac{(\widetilde{N}_i + \widetilde{N}_{\mathrm{O}}^-)^2}{2\epsilon_r \widetilde{T}}\right)(\widetilde{S}_i - \widetilde{N}_i) - \bar{\kappa}_2 \widetilde{N}_i, \tag{4.6a}$$

$$\frac{\mathrm{d}\widetilde{N}_{\mathrm{O}}}{\mathrm{d}t} = \bar{\kappa}_3 \left[\mathrm{O}_2\right]^{\frac{1}{2}}\left(\widetilde{S}_e - \widetilde{N}_{\mathrm{O}} - \widetilde{N}_{\mathrm{O}}^-\right) - \bar{\kappa}_4 \widetilde{N}_{\mathrm{O}} - \frac{\mathrm{d}\widetilde{N}_{\mathrm{O}}^-}{\mathrm{d}t}, \tag{4.6b}$$

$$\frac{\mathrm{d}\widetilde{N}_{\mathrm{O}}^-}{\mathrm{d}t} = \bar{\kappa}_5 \exp\left(-\frac{(\widetilde{N}_i + \widetilde{N}_{\mathrm{O}}^-)^2}{2\epsilon_r \widetilde{T}}\right)\widetilde{N}_{\mathrm{O}} - \bar{\kappa}_6 \widetilde{N}_{\mathrm{O}}^- - \bar{\kappa}_{11}\left[H_2\right]^{\frac{1}{2}}\widetilde{N}_O^-,$$

where a total of 9 parameters are to be determined.

In these measurements, pulses of 20 ppm hydrogen were applied for 15 minutes at 300°C, where two pulses were measured. The comparison of the best estimates to the measurement data is shown in Figure 4.8.
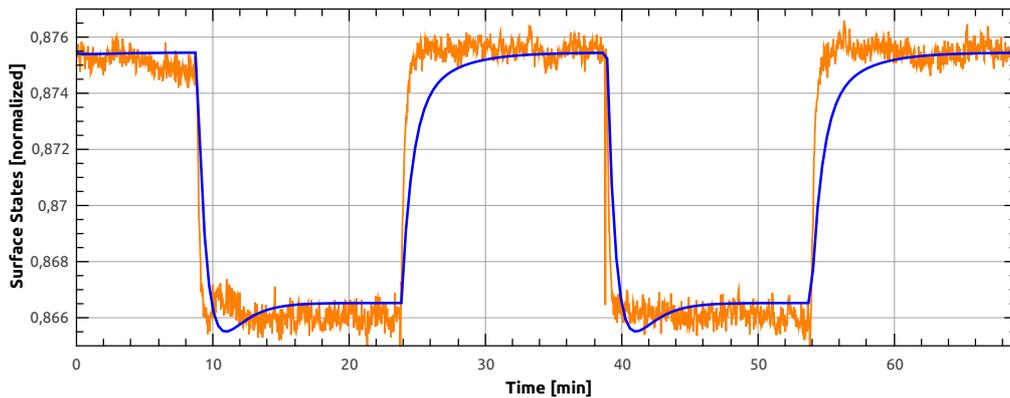
Figure 4.8: Comparison of the best estimates for the hydrogen pulses at 300°C. Blue curve: simulation; orange curve: experimental data.

The gas-induced change in the equilibrium is covered very well with the obtained model. However, at the beginning of the gas pulse, there is a small deviation between measurement and simulation, as the simulation overshoots and then reaches the equilibrium. During the recovery period, there is also a small deviation, since the simulation recovery takes a bit longer than in the measurement. However, the approximation is quite good, given the small size of the shift in the equilibrium and the fact that all parameters had to be estimated at once.

The determined numerical values are shown in Table 4.4. Here, we only needed to determine an effective frequency factor since only one temperature was considered. Therefore, no information on the activation energies is obtained. In order to compare the obtained numerical values to the results of Section 4.5, we need to compute the effective frequency factors from the nitrogen experiment using formula (2.30). There, we obtain as numerical value during the cooling phase $\bar{\kappa}_1 = 0.00281$, which is the same order of magnitude and therefore quite a reasonable result. However, the back-reaction yields a frequency factor $\bar{\kappa}_2 = 0.00012$, which is one order of magnitude lower.

Parameter	Value
$\bar{\kappa}_1$	0.00601
$\bar{\kappa}_2$	0.00580
$\bar{\kappa}_3$	0.00137
$\bar{\kappa}_4$	0.00175
$\bar{\kappa}_5$	0.00189
$\bar{\kappa}_6$	0.00547
$\bar{\kappa}_{11}$	0.00274
$\widetilde{S}_i$	3.5563
$\widetilde{S}_e$	0.5954

Table 4.4: Estimated parameters for the adsorption process of hydrogen in dry air atmosphere. Note that since we consider a fixed temperature, no activation energies were to be determined.

4.8   Using Different Error Notions

The choice of the error notion when comparing simulation and experiment is not clear a priori, although there are three natural candidates to consider, namely the L^1-norm, the L^2-norm and the L^∞-norm.

Heuristically speaking, the L^1-norm is the sum of the errors at each data point during the measurement, while the L^2-norm is the square root of the sum of the squared errors. By definition, both notions take every point of the measurement into account. Contrarily, the maximum norm only uses the largest error throughout the set of data points.
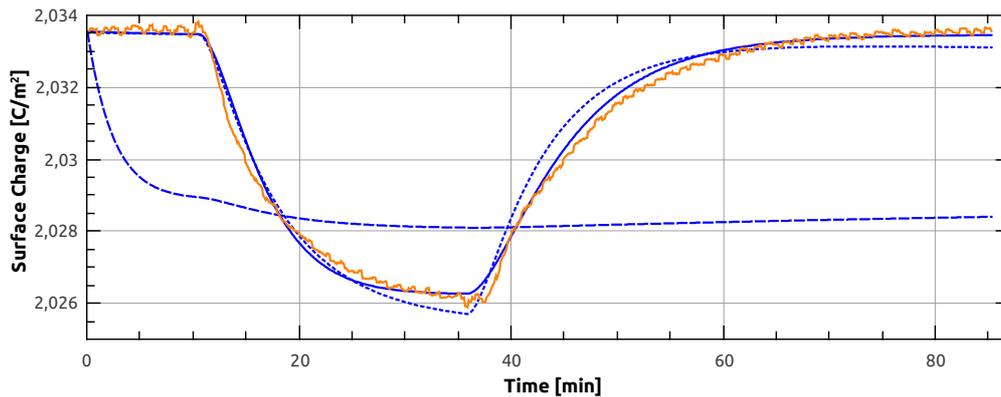
Figure 4.9: Comparison of the best estimates for the L^1-norm (blue line), the L^2-norm (blue, short-dashed) and the L^∞-norm (blue, long-dashed) to the experimental data (orange) at 200°C.

To shed light on the question which norm to use, measurements of carbon monoxide pulses in nitrogen atmosphere at 200°C, 250°C and 300°C were investigated separately. The best estimates

for all three norms are shown in Figures 4.9, 4.10 and 4.11.
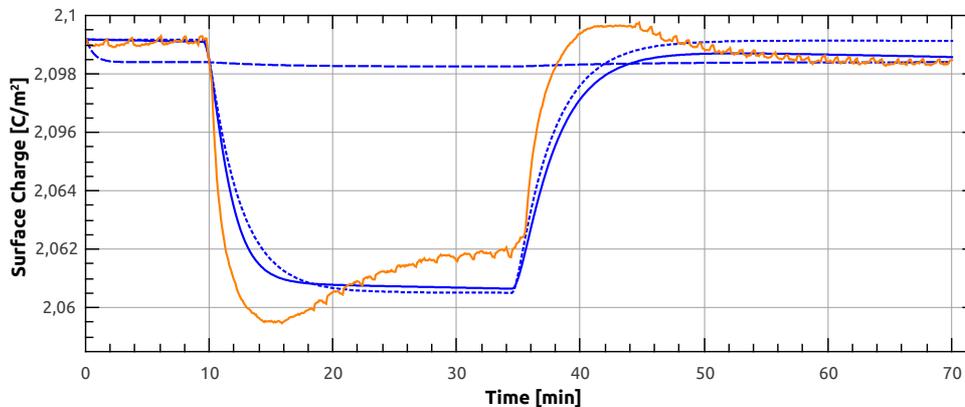
Figure 4.10: Comparison of the best estimates for the L^1-norm (blue line), the L^2-norm (blue, short-dashed) and the L^∞-norm (blue, long-dashed) to the experimental data (orange) at 250°C.

It is obvious that the maximum norm does not provide any reasonable approximation of the sensor signal, since not only is the error at the beginning of the pulse significant, but also is there no sign of a recovery of the base signal after the end of the pulse. The problem here might lie in the fact that as soon there is any deviation in the sensor signal (which might occur due to technical reasons and also due to the randomness of all the occuring processes), there will be a difference to the simulated signal, the maximum of which governs the norm. Therefore, during search for a minimum of the norm, it does not matter if there are significant deviations as long as they are smaller than the already accounted maximum deviation.

The L^1-norm does cover the beginning as well as the end of the pulse. In particular, at 200°C, the L^1-norm gives the best estimate, but there is still a significant deviation between the best estimate and the measured signal at higher temperatures.

The L^2-norm, finally, gives very good results at 200°C, and the best results at 250°C and 300°C. This is also the most widely used notion for the error, known as the *least-squares estimate.*

However, neither of the error notions gives estimates that model the exact sensor behavior at higher temperatures. Nevertheless, it has to be mentioned that the maximal drop in the signal during the pulse is in the range of 0.4% in these measurements.

4.9   Summary

The estimation of the reaction constants for biomolecule detection worked very well. The agreement of the simulation and the experimental data is good and the obtained numerical values are reasonable.

Although gas-detection measurements only provided small temperature steps, the estimation of the pre-exponential factor G_0 governing electrical conductance worked well, i.e., a low least-
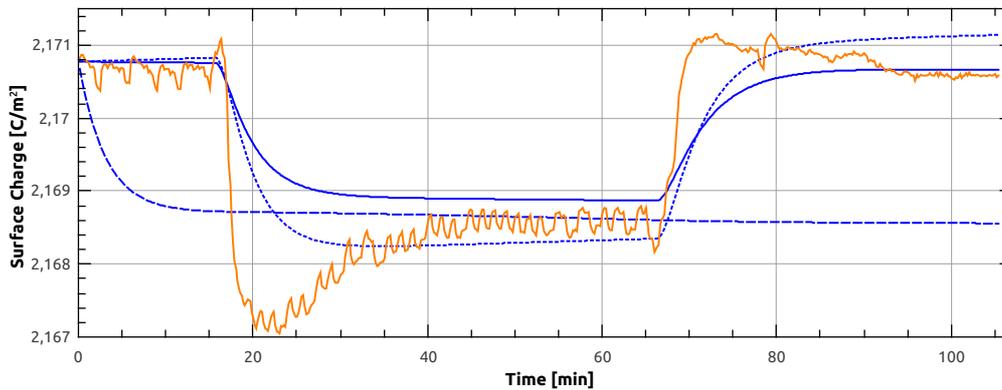
Figure 4.11: Comparison of the best estimates for the L^1-norm (blue line), the L^2-norm (blue, short-dashed) and the L^∞-norm (blue, long-dashed) to the experimental data (orange) at 300°C.

squares error was obtained in the fitting process. From this, it seems natural to assume that the applied model is a very good approximation to the actual behavior of the nanowire.

The estimation of reaction parameters turned out to be quite sensitive to errors in measurements. Even with small noise, the results can change considerably. Nevertheless, the obtained numerical values provide a satisfying approximation of the sensor signal. It must be noted that especially after finishing a heating period, there seem to be effects that are not taken into account yet. Therefore, the approximation is not as good as during other sections of the measurements.

The comparison of different norms confirmed the application of the L^2-norm as reference for the error. The L^1-norm as well as the maximum norm showed a much larger deviation from the sensor signal.

<div style="text-align: right">

Chapter 5

</div>

Analysis and Simulation of Fluctuations in Nanowire Sensors

As has been discussed at several occasions throughout this thesis, the simulation of nanowire sensors is an essential tool for optimizing the design of these devices. Here, two objectives are addressed. First, we analyze noise in gas-sensor signals in order to see whether any information on the detected gas can be extracted (cf. Section 5.1). The analysis is based on the theory presented in Sections 3.3 and 3.5. These findings were published in [100].

Second, we present simulations for realistic biosensor devices, which are mostly based on the ones considered in [75]. With the results obtained in Section 4.2, the full reaction-diffusion system is simulated and analyzed in the remainder of this chapter.

To gain first insights into the behavior of the coupled systems, we present results from the one-dimensional simulations, which have been conducted following the box-based algorithm. After we proved the necessity for including diffusion to the model, we calculate binding efficiencies as well as absolute **PT** densities for target-molecule concentrations in the range between 1 nM and 270 μM. Next, we consider the behavior of the final variance, its evolution over time as well as the SNR under the same conditions. To complete the simulations in one dimension, we investigate the system under different initial conditions, which corresponds to stirring the aqueous solution prior to the measurement. All results on one-dimensional reaction-diffusion systems were published in [98] and [99].

Since the one dimensional simulations just allow very simple geometries, we extended simulations to two dimensions. As the implementation of the box-based algorithm is a bit cumbersome in this case, we used the random-walk approach here. In these simulations, the surface will divided into several partitions, which allows to distinguish the behavior at these regions of the surface.

Again, signal, noise and SNR will be investigated depending on different widths of the domain in Section 5.3.1. Furthermore, we consider asymmetrical initial conditions, which correspond to more realistic devices, where the slit for target-molecule entry is at one particular side of the domain. The effects of this setup are investigated in Section 5.3.2.

5.1 Analysis of Gas-Sensor Signals

This section addresses the decomposition of gas-sensor signals in order to extract noise induced by surface processes. Here, wavelet decomposition is used in two different settings. First, a measurement of H_2S pulses was decomposed and the detail coefficients were investigated in detail. Second, several measurements with different environmental parameters (eight in dry air, two in humid air) were looked at using wavelet decomposition to find out the ones performed with humidity present.

All experiments discussed in this section were performed with CuO sensors using a nanowire network configuration. For a thorough presentation of the used sensor, see [87].

### 5.1.1 H$_2$S pulses

Wavelet decomposition was applied to a measurement of hydrogen sulfide (H_2S) pulses in dry air (80% nitrogen, 20% oxygen) at 325°C. The pulses included different H_2S concentrations of 100-500 ppb, where two pulses per concentration were measured. One pulse lasted for 15 minutes, after which the system was given 30 minutes to recover. The exact pulse data and the obtained signal is given in Figure 5.1.
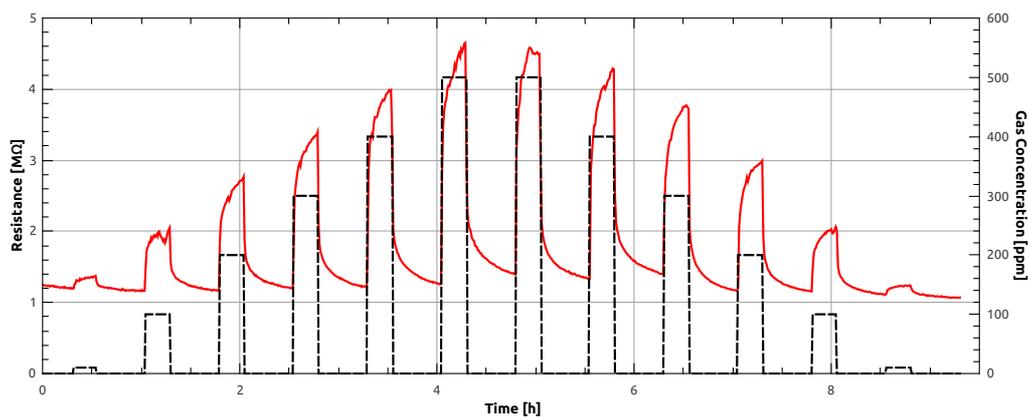

Figure 5.1: Applied gas pulses (black, dashed) and obtained signal (red line) from the H$_2$S measurement in dry air.

The application of a discrete wavelet transform gives the detail coefficients shown in Figure 5.2. Here, Daubechies wavelets of order 3 were used, and we calculated four detail coefficients. The larger variances in the first three coefficients during certain periods of time as well as the sharp
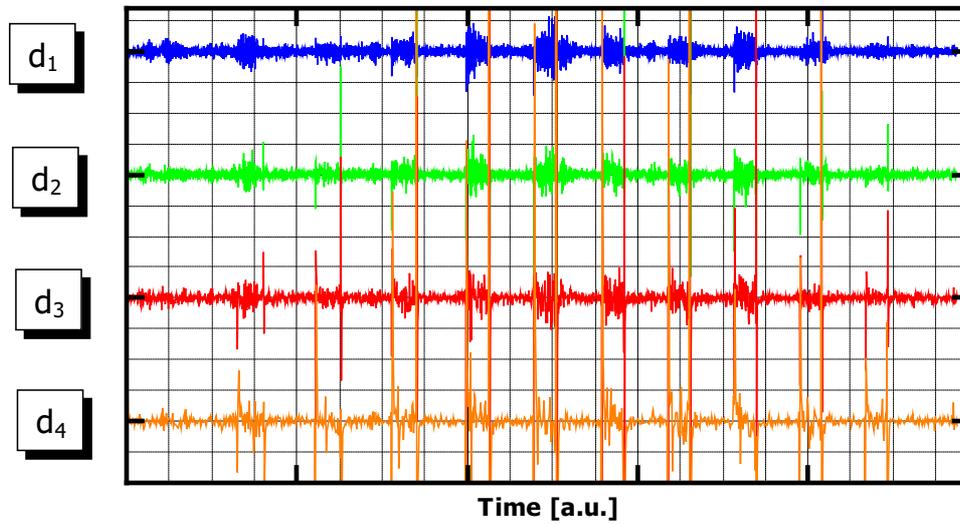
Figure 5.2: Wavelet decomposition of the investigated signal. The first four detail coefficients are shown.
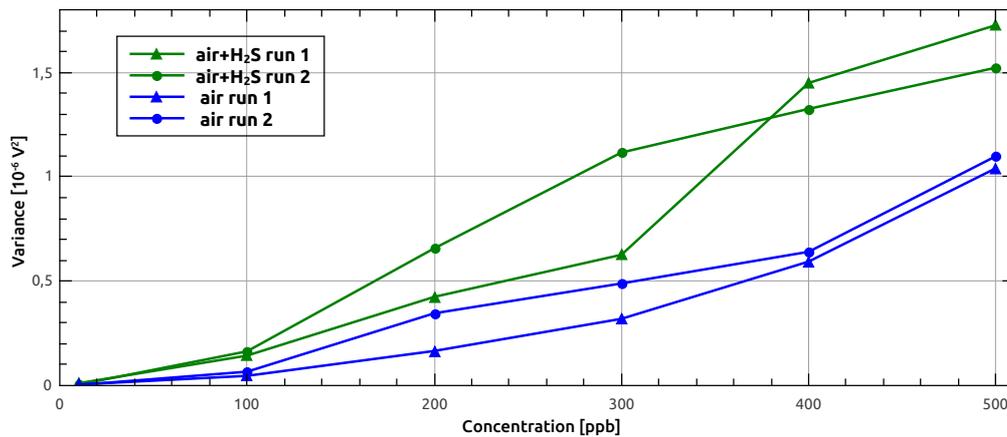
Figure 5.3: Variances of the first detail coefficient d_1 with and without presence of H_2S gas. Each gas concentration was measured twice.

extrema at the beginning and at the end of these periods already indicate the presence of the gas.

As a next step, the variances of the detail coefficients d_1 were calculated for phases with present gas and for the recovery phases. It turns out that these variances increase during the gas pulses and are even proportional to the gas concentration. During the recovery phases, the variance is also proportional to the prior gas concentration, which can be explained by the fact that the gas molecules need some time to desorb from the surface when the gas pulse is over. Until then, its effect is still seen in the noise. The results discussed in this paragraph are shown in Figure 5.3.
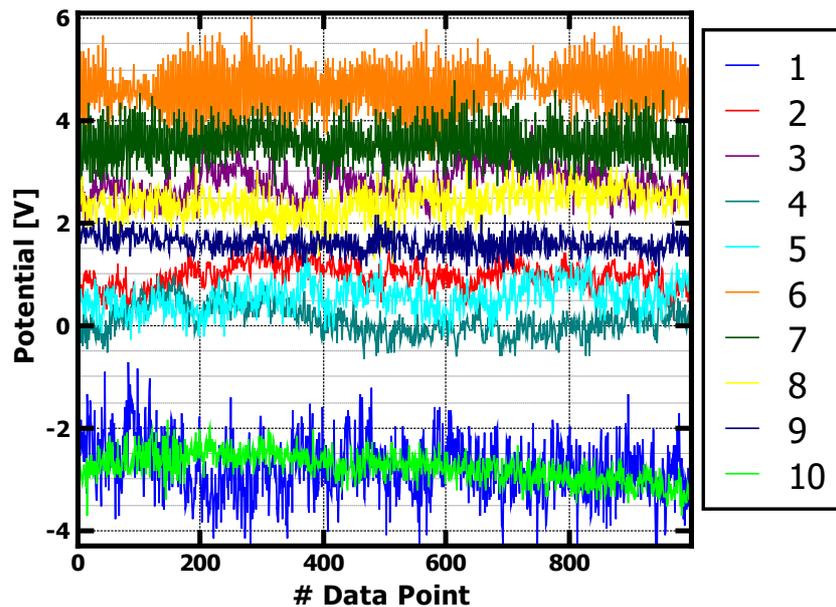
Figure 5.4: Measurements taken for the determination of the presence of humidity. Two of them were taken within a humid environment, while the rest was conducted within dry air.

5.1.2 Humidity

Ten short-time measurements using the same sensor were performed, eight of which in dry air, the rest in humid air. All the measurements were taken using different electrode setups, which results in different base resistances shown in Figure 5.4. At that time, we did not know which were the experiments in humid air.

We now searched for differences in the decomposition of the signals, which originates in the presence of water vapour. In order to do so, the signal was decomposed again using Daubechies wavelets of order 5.

The variances of the first six detail coefficients for all the measurements are shown in Figure 5.5. In every coefficient, the variance in experiments 4 and 5 is significantly higher than in all the others. This suggests that these are the experiments conducted in humid air, and also corresponds to the theoretic qualitative prediction of higher variances with more occuring reactions. Indeed, experiments 4 and 5 are the ones including water vapour in the sensor atmosphere.

5.1.3 Summary

The goal of this section was to extract information on the surface reactions from the signal by just considering the noise level. The important feature here is that no numerical information on the governing parameters is necessary. In particular, the presence of an additional species could even be determined without exactly knowing the reaction path and its stoichiometry. The difference in the noise arises by the fact that each reaction increases the noise level due to its random nature. For the pulsed gas measurement, even a correspondence to the gas concentration
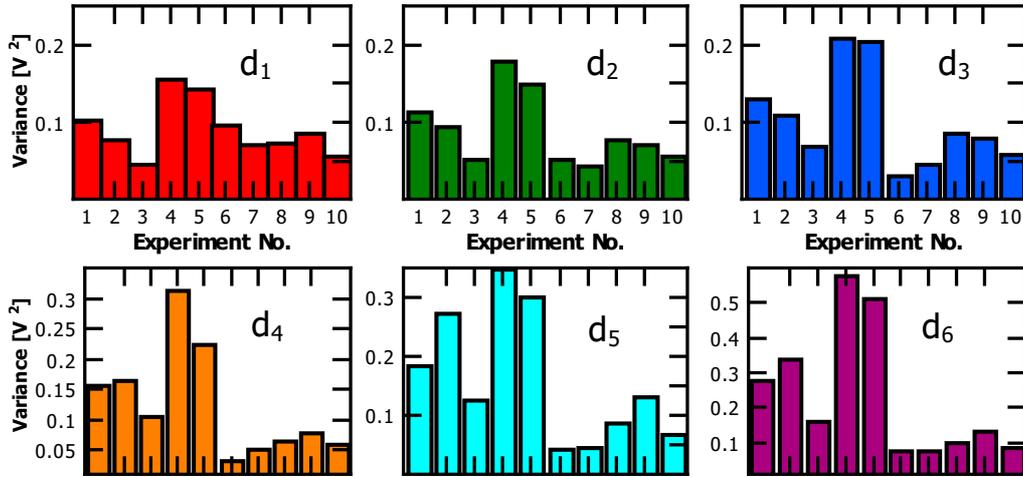
Figure 5.5: Variances of the first six detail coefficients for all ten considered measurements. Experiments 4 and 5 are the ones conducted under humid environment.

was found.

Of course, these results alone cannot be used to distinguish between different gases, since there are too many unknowns in the system to do so. However, in combination with other techniques like governing parameter estimation, this task could be accomplished.

5.2 Biosensor Simulations in 1D

We now turn our attention to simulations of biosensors. Starting with simulations in one dimension, we employed Algorithm 1 to obtain the numerical results. In this case, we considered a liquid domain of 500 μm in height and used 500 target molecules to move around. In order to obtain the desired target-molecule density, we virtually changed the width and depth of the domain. Since this has no effect on the diffusion, the only consequence is a change in the absolute number of receptor molecules at the surface that actually needs to be changed.

5.2.1 SNR in the Case of Constant Target-Molecule Concentration Near the Surface

In the (simplified) case of constant target-molecule concentration near the surface, one can easily calculate the signal-to-noise ratio via formula (3.23). For the reaction constants obtained in Section 4.2 and the target-molecule density of 1 μM used in the experiments, the evolution of the SNR is shown in Figure 5.6.

It turns out that the final SNR is higher for lower probe densities, which can also be seen from the representation in formula (3.24).
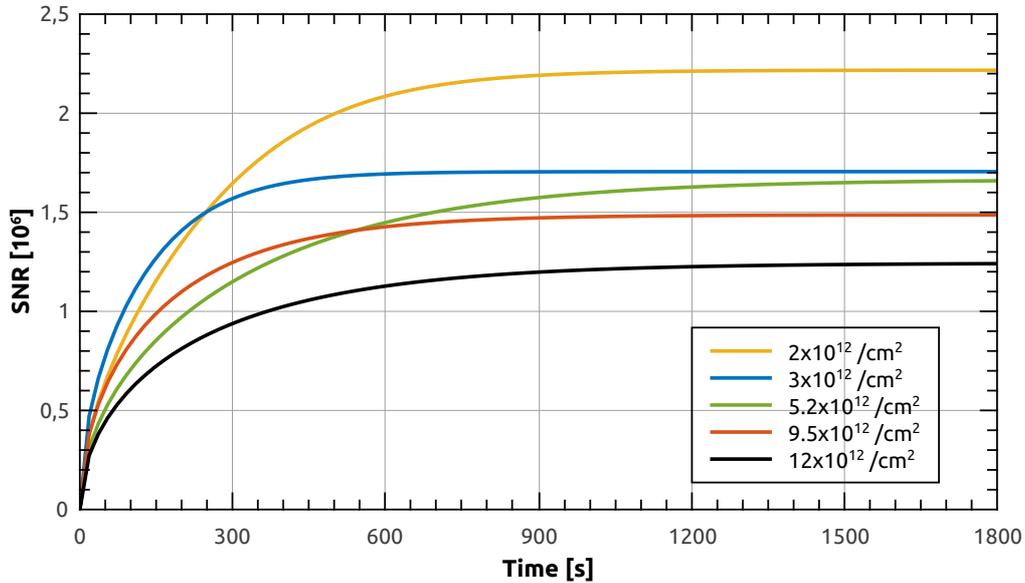
Figure 5.6: SNR for different probe-molecule concentrations in the constant target-molecule concentration regime.

### 5.2.2 Motivating the Implementation of the Coupled System

To motivate the implementation of the coupled reaction-diffusion system, we compared the results to the data obtained from the pure hybridization system. We calculated both solutions for a 1μM solution of target molecules in the liquid, and for the different probe densities. The comparison of the data is shown in Figure 5.7.

The difference between the two situations is significant for all probe densities. In particular, the surface-charge density is lower in the coupled system, which is in line with intuition, since with a limited amount of target molecules fewer probe-target complexes will build up. This fact confirms that the investigation of the coupled model leads to further information on the investigated device.

5.2.3 Binding Efficiency and Surface-Charge Density

To optimize sensor design, we investigate the correlation between probe-molecule density and target-molecule density under various circumstances. The goal is to find an optimal setup for a given target-molecule concentration, and to obtain information on detection limits and waiting times in such a setup. Here, we consider target-molecule concentrations in the range between 1 nM and 270 μM.

There are two different quantities of interest when considering optimal setups, which will both be investigated in this study. On the one hand, there is binding efficiency, which is given by the ratio of hybridized complexes at the surface to the total number of probe molecules. On the other hand, the surface-charge density is proportional to the total number of probe-target
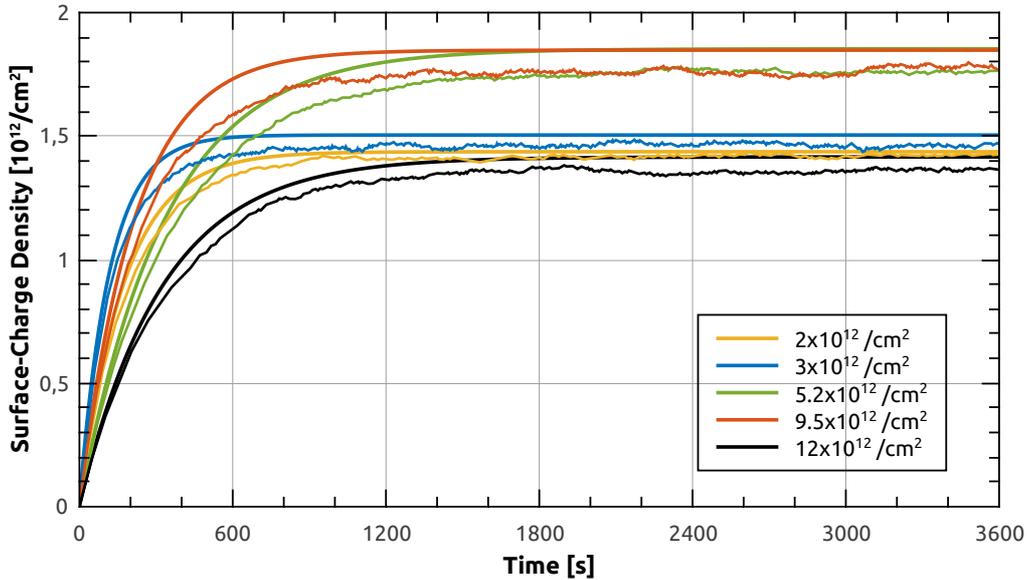
Figure 5.7: Comparison of solutions of the reaction model and the reaction-diffusion system. The differences are significant, which motivates the utilization of the coupled system.

complexes per surface area.

The reason for considering the binding efficiency is obvious, since one always seeks for the most efficient way of measuring a quantity. The necessity of considering the surface-charge density instead of the binding efficiency becomes clear when investigating very low target and probe concentrations: In this case, one may obtain a very high binding efficiency, i.e. most of the probe molecules are hybridized to complexes, but since they are very few, the change in the surface-charge density barely influences the sensor signal. Hence, if one has a noisy signal, one might miss the detection of the target molecules. Furthermore, when considering high probe-molecule densities, the change in binding efficiency may be very small, but since the absolute number of probe-target complexes at the surface is very large, the change in the surface-charge density is high and therefore yields a strong signal.

The equilibrium values of the binding efficiency depending on the target concentration are shown in Figure 5.8. The binding efficiency attains a perfect value of almost 100% when the target-molecule density is large enough. However, this treshold extremely differs between probe-molecule densities, as it is around 1 μM for 2×10^{12} molecules/cm^2 and around 270 μM for 12×10^{12} molecules/cm^2. Furthermore, when a binding efficiency of 100% is reached, it is not possible to obtain any quantitative results on the target-molecule density. For low target-molecule concentrations, the final binding efficiencies differ by a constant factor, as is indicated by the parallel lines in the log-log plot.

Figure 5.9 shows the equilibrium values of the density of probe-target complexes. As expected, the result is quite different to the efficiency approach. Again, for lower target concentrations, the resulting values differ by a constant factor, where the highest densities are obtained for lower
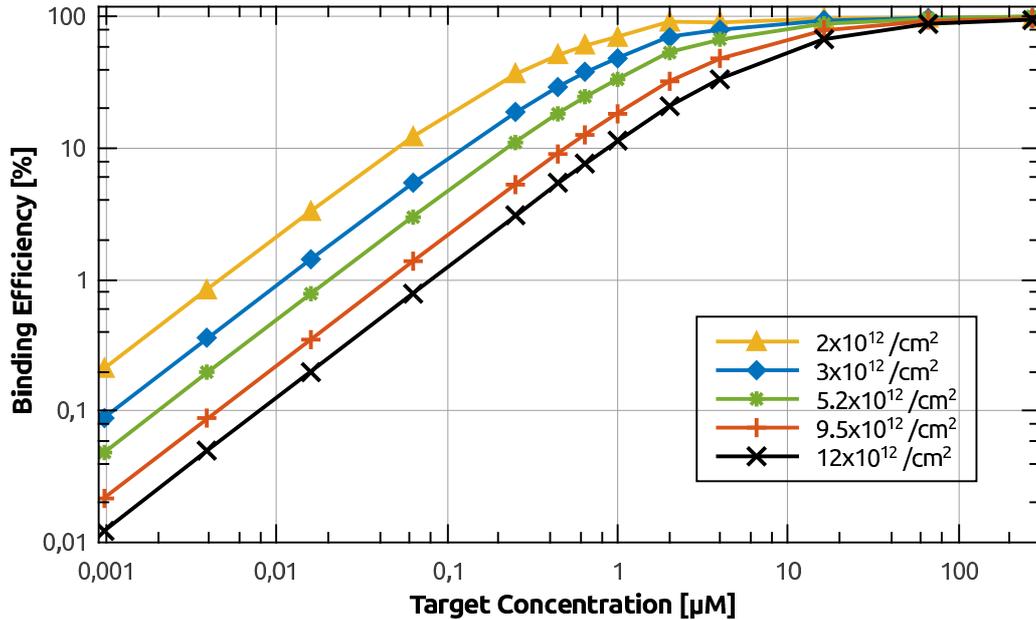
Figure 5.8: Binding efficiency as a function of target-molecule concentration. The different curves represent different probe densities at the surface (numerical values indicated in the legend). At sufficiently high concentrations, all the probe molecules are hybridized.

probe-molecule densities. However, for large target-molecule concentrations, the situation is vice versa, as we obtain lower values for lower probe-molecule densities. The equilibria with respect to the target-molecule density that are approached in the shown curves clearly originate from the perfect efficiency at the respective probe-molecule densities and therefore coincides with the respective treshold values discussed in the previous paragraph.

As a consequence, there is an inversion of the optimal probe density. As can be determined from Figure 5.9, this happens roughly around 1 μM target-molecule concentration. As discussed above, this observation is important, since it means that the probe-molecule density is a major design parameter. For optimal sensor responses, one has to adjust its value to the target-molecule density of interest.

5.2.4   Variance

To determine whether a sensor works fine or not, the expected value for the signal is not the only parameter to consider. One also needs to turn ones attention to the noise in the signal. Therefore, motivated by the discussion in Section 3.1 an investigation of the variance is crucial.

The numerical values of the variances at the equilibrium are shown in Figure 5.10. There is a maximum at a value around 3 μM. For lower target-molecule densities, the variance increases with increasing target-molecule density, while it is the other way round for target-molecule densities higher than 3 μM. This is related to the fact that at high target densities, practically every probe molecule is hybridized. Furthermore, if dissociation occurs, the respective probe molecule will be
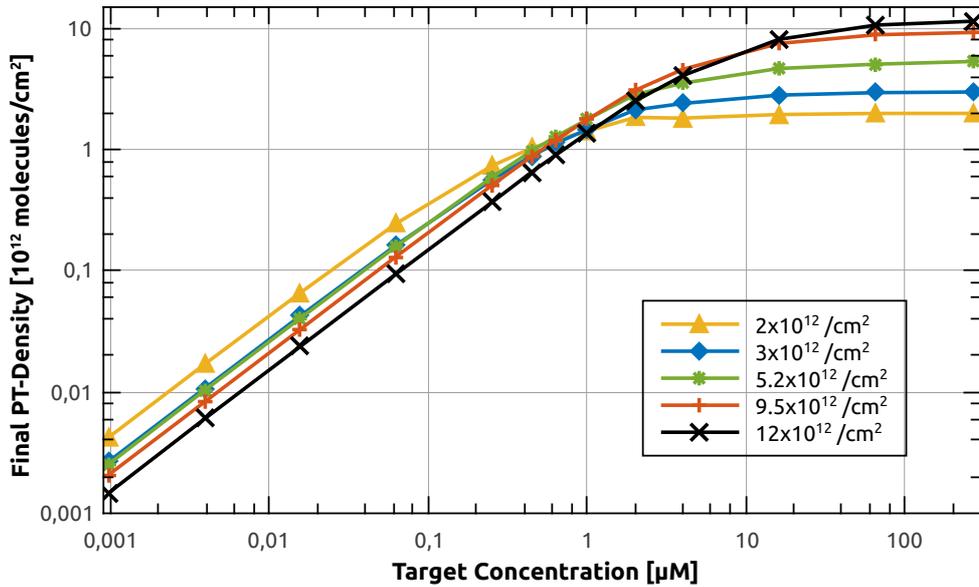
Figure 5.9: Equilibrium **PT** density depending on target-molecule concentration. Inversion of the optimal probe density occurs around 1 μM. The equilibria being approached for high target-molecule densities correspond to the perfect binding efficiencies observed in Figure 5.8.

re-hybridized almost immediately, since there are still many target molecules in the liquid. This fact is important for the investigation of the SNR, which will be done in the following section.

After we have considered the equilibrium values of the variances, we should now also have a look at their evolution over time. Therefore, we have a closer look on the simulations at several concentration regimes between 0.26 and 16.6 μM. Here, the probe-molecule density was set to 2×10^{12} molecules/cm^2. The corresponding curves are shown in Figure 5.11. At lower concentrations, i.e. up to approximately 0.46 μM, the variance monotonously increases from the beginning to reach its equilibrium state. The period of time until the equilibrium is reached decreases with higher concentration. This behavior is not surprising at all.

However, at higher concentrations, the behavior is qualitatively different, since a significant maximum evolves before the variance attains its equilibrium value. Therefore, to obtain the optimal signal-to-noise ratio, it is necessary to wait for a certain period of time, which is an important information for an experimenter. Here again, one finds the decrease in the equilibrium variance for increasing target-molecule concentration.

5.2.5 Signal-to-Noise Ratio

From the data gathered in the previous sections, we are now ready to investigate the signal-to-noise ratio of the device.

By definition of the signal-to-noise ratio in equation (3.23), the SNR is higher when the variance is lower, so from this point of view, very large as well as very low target-molecule concentrations
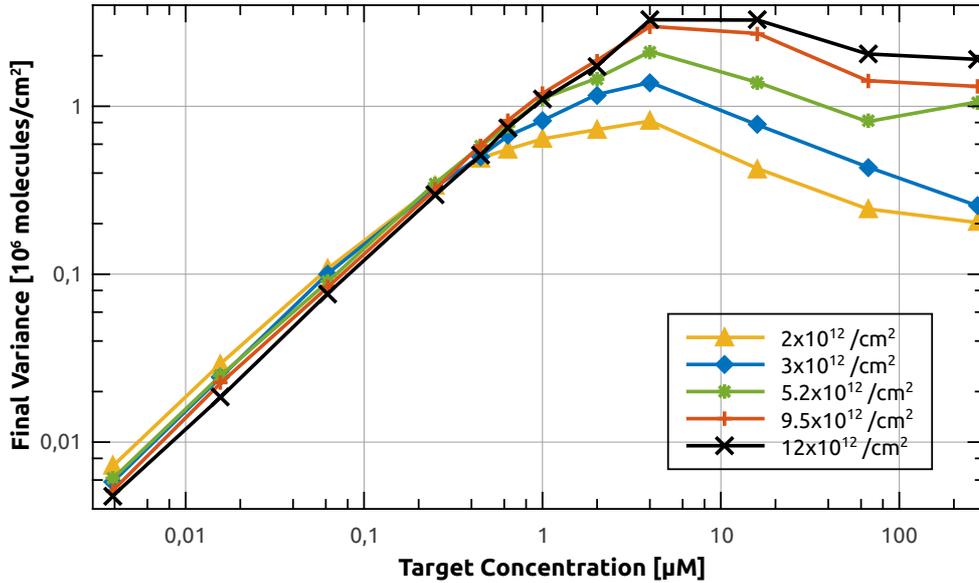
Figure 5.10: Standard deviation of the number of probe-target complexes at the surface at equilibrium with respect to the target-molecule concentration. At high concentrations, the value decreases with increasing target-molecule densities since almost all probe molecules are hybridized.

appear to be acceptable. However, since the signal increases with increasing target-molecule concentration, the SNR will be highest for large concentrations. The exact data can be seen in Figure 5.12. In fact, for concentrations below 3 μM, expected value and standard deviation increase by the same factor, so the SNR stays almost constant in this regime. At higher target concentrations, the variance decreases according to Figure 5.10, so the SNR increases.

5.2.6   Different Initial Conditions

Another parameter influencing the performance of the sensor is the initial composition of the aqueous solution. In particular, we investigate if mixing the fluid prior to the measurement will have any effect on the surface processes. This question was also investigated experimentally in [90].

Of course, the preparation of the aqueous solution is described by the initial conditions for the system, which will be set in an appropriate way. In particular, we consider two cases.

In the first case, we consider that the fluid is well stirred, which corresponds to a uniform distribution of the target molecules in the beginning of the simulation. This is established by putting an equal amount of molecules into each box. When the simulation starts, there are molecules near the surface at the beginning, which can immediately hybridize with the probe molecules at the nanowire.

Second, we consider the situation that the target molecules are poured into the measurement chamber from above. This corresponds to putting all the molecules in the very top box of the
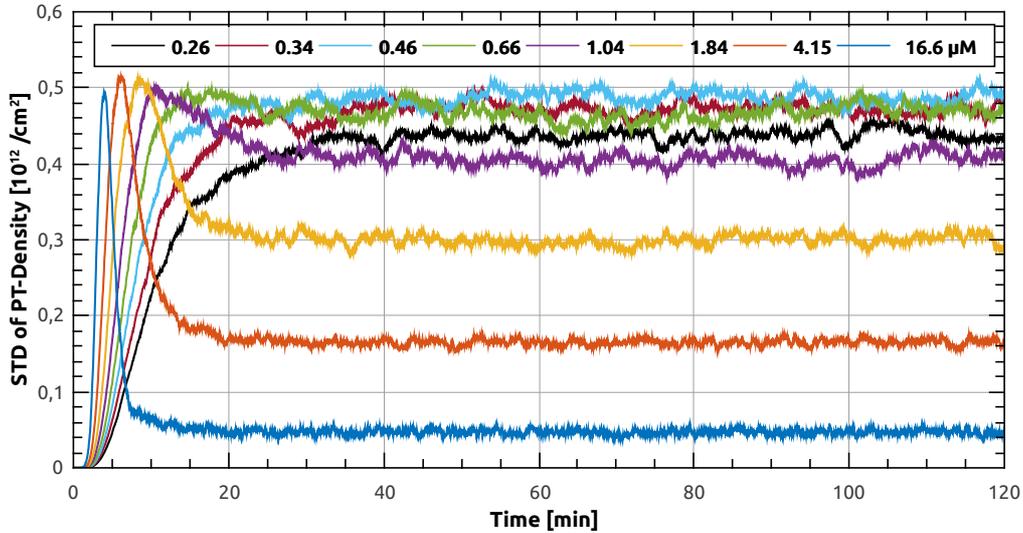
Figure 5.11: Evolution of the variance for several different target-molecule concentrations. In high-concentration regimes, a significant maximum is observable.

measurement chamber. Here, it will take some time until the target molecules reach the surface to hybridize with their matching probe molecules.

In this approach, we calculate the expected time until 80% of the equilibrium surface-charge density is reached in each case.

For low concentrations, there is almost no dependence on the concentration of the solution. At approximately 0.5 μM, the expected time starts to decrease with increasing concentration. However, the important difference here is that this effect is larger when the solution is well stirred in the beginning, as is shown in Figure 5.13.

The numbers in Figure 5.13 indicate that the equilibration process can be speeded up from a few minutes to several seconds, which is approximately two orders of magnitude. This simulation results appear to be important for experimenters, since it means that proper mixing of the solution is essential for fast detection.

5.3   Biosensor Simulations in 2D

Simulations in two dimensions allow two important improvements. First, one can distinguish hybridization at the transducer and at the chip on which the transducer is placed. The effects of this distinction and the 2D geometry are adressed in Section 5.3.1. Second, as already mentioned several times, more complicated initial conditions can be realized in this setting. Here, we will simulate the hybridization at the surface for asymmetric different initial conditions and compare the respective output to the symmetric case.
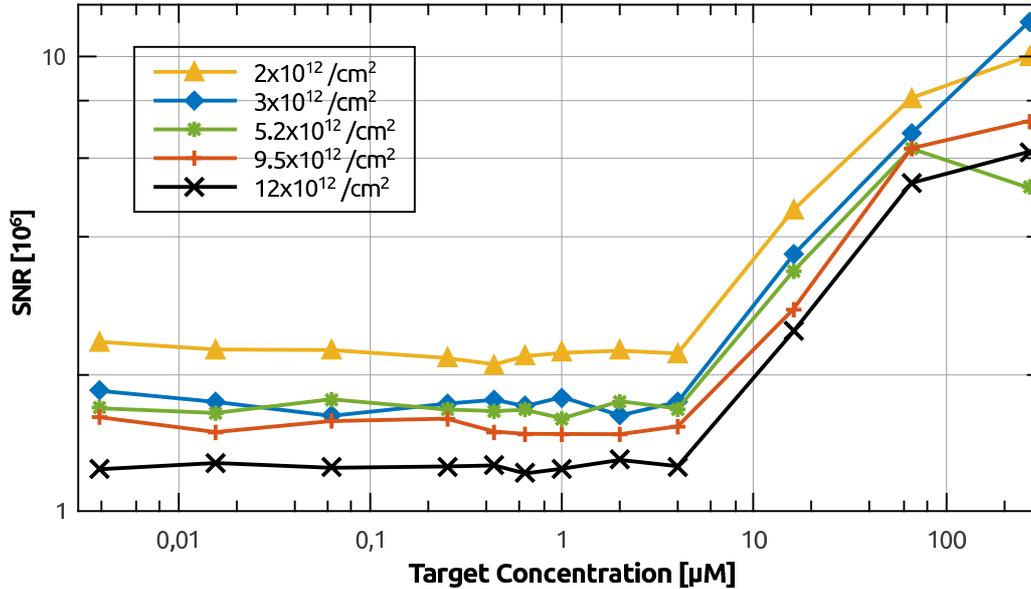
Figure 5.12: Signal-to-noise ratio at the equilibrium corresponding to Figure 5.10. Its value is constant up to a target concentration of approx. 3 μM. This is also due to the fact that the variance decreases with increasing target-molecule concentration.

### 5.3.1 Basic Features and Dependence on the Width of the Chip

First of all, we simulated the system under the following circumstances. We have a fixed number of target molecules within the liquid, and we consider different widths for the domain. Also, the height of the domain is fixed. The used parameters for this series of simulations is given in Table 5.1. With these numerical values, we obtain simulations for concentrations between 2.5 and 93 μM. As initial condition, we want to have an already mixed solution in the beginning, so the target molecules are distributed uniformly over the whole liquid domain. Here, we divided the surface into compartments of 25 μm each, which allows to investigate the hybridization in different regions of the device. A sketch of this partitioning is shown in Figure 5.14(b).

The equilibrium values of the signal depending on the target-molecules concentration are shown in Figure 5.14(a). Here, the different curves relate to different positions at the sensor. This correspondence is explained in Figure 5.14(b). It turns out that the hybridization is higher at the four compartments next to the edges of the sensors. This is due to the fact that the area from which the probe molecules in these regions are accessible is higher, as was already indicated in the sketch of the geometry in Figure 3.2. The same argument explains the lower hybridization rate at the regions representing the corners of the sensor as well as the region next to the nanowire, which have a lower area from which they are accessible. For all the other regions, the final **PT** density is between the of the two discussed values and is the same everywhere. We will refer to this three regions as *edge regions*, *corner regions* and *middle regions*, respectively.

For the highest investigated concentrations, full hybridization, which is $3\times10^{12}/\mathrm{cm}^2$ is almost reached for edge and middle regions. Based on the discussion in the previous paragraph, it is
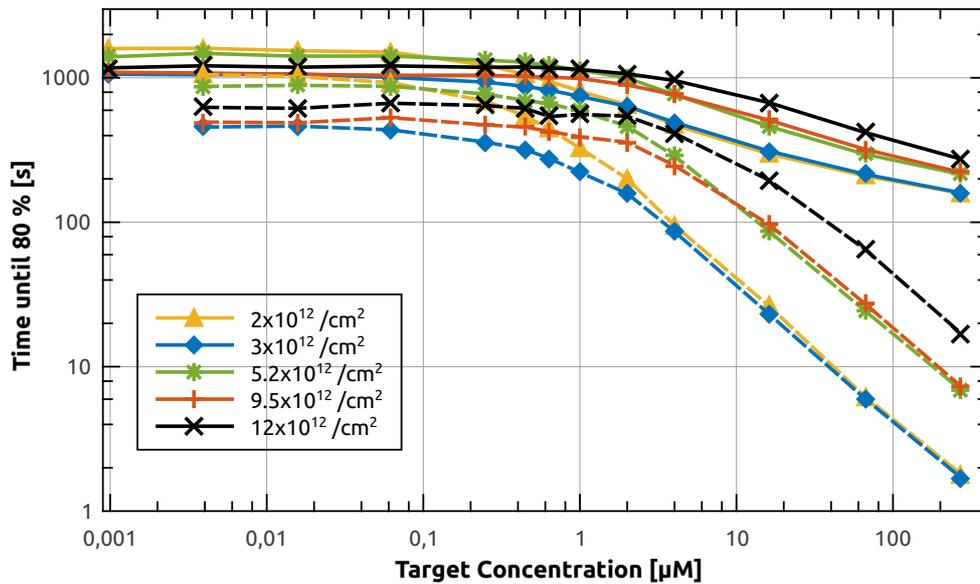
Figure 5.13: Expected time until 80% of the equilibrium surface-charge density are reached. Solid lines represent solutions where the target molecules are initially in the uppermost simulation box, while the dashed lines represent solutions where a uniform initial concentration is assumed.
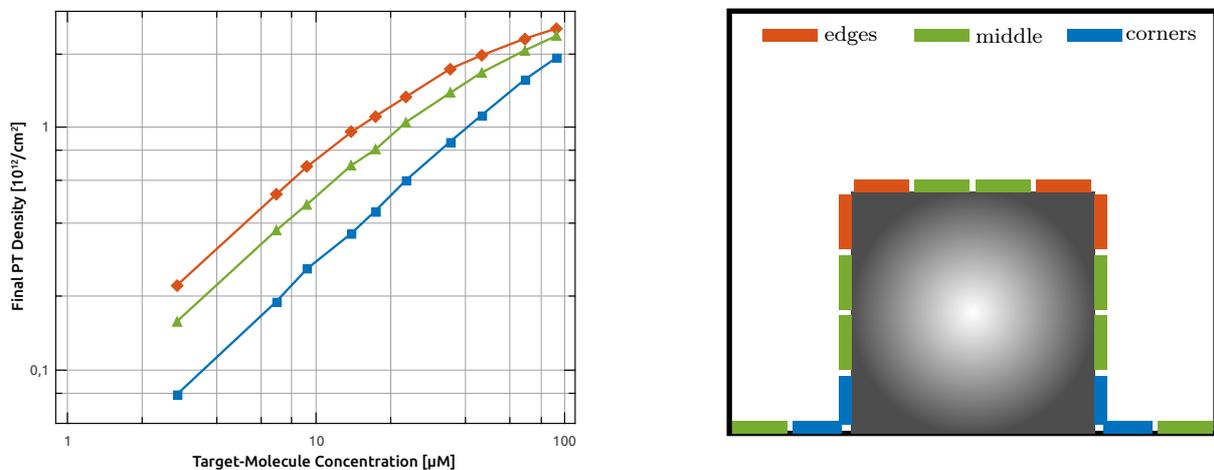
Figure 5.14: Left: Equilibrium value of the signal for different regions of the surface. Basically, there are only three regions to distiguish, where all the values are similar for the same type of surface. Right: Sketch of the different types of regions at the surface. The colors in the plot correspond to the colors indicating the types of regions.

not surprising that full hybridization is first obtained for edge regions. It can be seen that the difference between the different regions becomes lower for increasing concentrations.

parameter	numerical value	unit
height of domain	1	μm
width of domain	200-5000	nm
depth of domain	12	nm
height of sensor	100	nm
width of sensor	100	nm
number of particles	100	–
duration	150-250	s
stepsize	1	ms
iterations	2000	–
probe molecule density	3×10^{12}	cm^{-2}

Table 5.1: Used parameters for the simulations investigating the effect of the domain width on the sensor behavior.
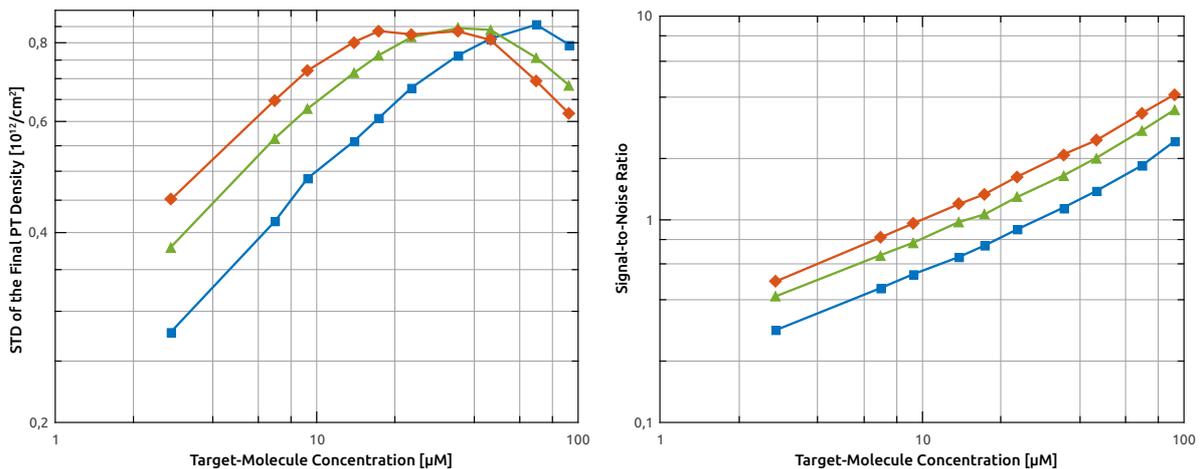
Figure 5.15: Equilibrium values for noise (left) and SNR (right). Again, the behavior for the different regions is resolved. The coloring is according to the sketch in Figure 5.14(b).

The equilibrium values for the noise, which corresponds to the standard deviation, are shown in Figure 5.15(a). Like in the 1D case, there is a maximum in the equilibrium value, but here, the position of the maximum is different for the different regions at the sensor. For increasing accessible area, the concentration of the maximum value decreases.

Resulting from Figures 5.14(a) and 5.15(a), the equilibrium values for the signal-to-noise ratio are shown in Figure 5.15(b). Similar as in the 1D case for that concentration regime, the SNR increases with increasing concentration. However, unlike in the 1D case, the behavior here is somewhat superlinear.

We now turn our attention to the evolution of the quantities of interest over time. Due to limited space in this work, we just consider one instructive case here, which will be the simulation for
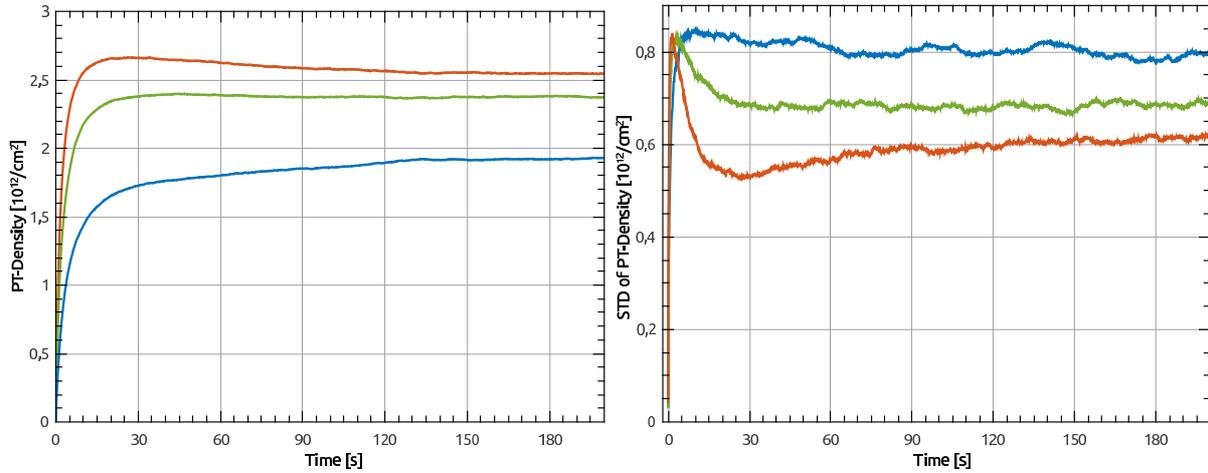
Figure 5.16: Evolution of the signal (left) and the noise (right) for the simulation of a 200 nm wide domain. The different colors correspond to different regions at the nanowire and the chip and are related to Figure 5.14(b).

a domain of 200 nm width. The evolution of the signal is shown in Figure 5.16(a). Here, the qualitative behavior is considerably different for the different regions. While it takes almost until the end of the simulation to reach the equilibrium (which is also the maximum) at corner regions, the equilibrium is attained very quickly for all the middle regions. However, the evolution for the edge regions is non-monotonic. There is a maximum after a short period of time, after which the value slowly lowers to reach the equilibrium value shortly before the end of the simulation.

The evolution of the variance is shown in Figure 5.16(b). As for the signal, the qualitative behavior is different. In all three cases, the maximum is reached after a few seconds. For the corner regions, the variance then slowly reaches its equilibrium value. The variance in the middle regions attains its equilibrium faster after a significant drop. For the edge regions, there is a steep drop after the maximum, and a minimum is reached at approximately 25 seconds, after which the value slowly attains its equilibrium.

As the variance has a significant maximum for the edge regions while at this point, the drop has already happend for the middle region and the noise in the corner region has just a little dropping ahead, the global minimum in the noise of the whole sensor might not be in the equilibrium. This is an important information for an experimenter, since it means that one has to conduct the measurement at the right time before the equilibrium is reached.

5.3.2   Different Initial Conditions

As we have seen in the previous section, we obtain the same results at similar regions of the surface. Therefore, in this case it is enough to only consider on half of the domain. Now we are ready to go one step further by considering more realistic initial conditions. In fact, in experiments the target molecules sometimes enter the domain via one small slit in the side of the box. This will be modeled here by putting all target molecules in a small area at the very right of the domain, as is shown in Figure 5.17(a).
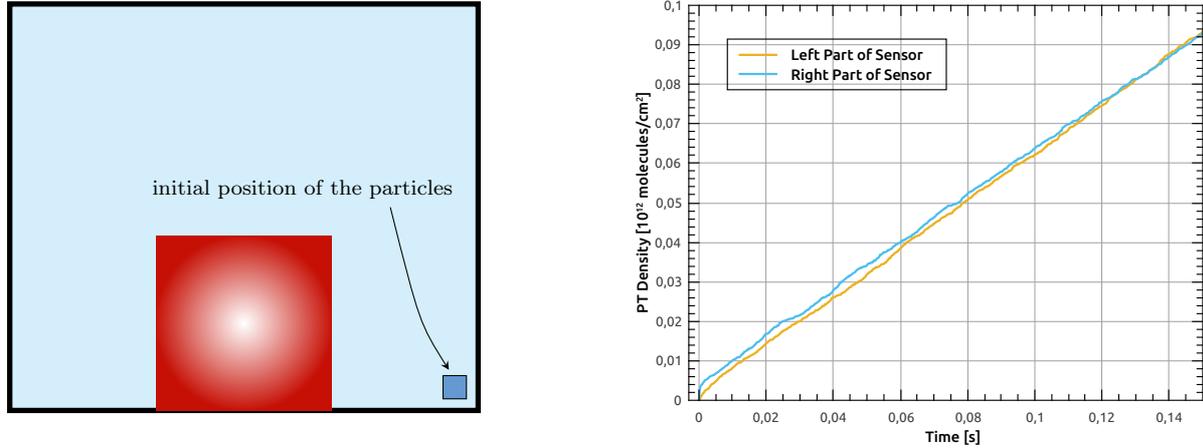
Figure 5.17: Left: Sketch of the asymmetrical initial conditions used in this simulation. Right: Comparison of the signal at the two halfs of the nanowire. Here, just the first 0.25 s are shown. The difference between the two parts is significant in the beginning, but vanishes during the simulation.

In order to investigate different initial conditions, it is necessary to choose very small timesteps in order to resolve single moves of the particles. The maximal acceptable timestep is assumed to be in the order of the size of the nanowire, which is 100 nm in this case. Here, we chose a step of 5×10^{-6} s. Accordingly, we only investigated shorter periods of time, since after some time the system will be in the same state as in the symmetric situation. In fact, it will turn out that this happens very fast. The used parameters for this simulation are given in Table 5.2.

Figure 5.17(b) shows the sums of the hybridized complexes on the left and on the right half of the nanowire. Obviously and as expected, hybridization starts earlier on the right half, but the density increases approximately with the same rate at both parts. However, after just 0.25 s, the

parameter	numerical value	unit
height of domain	1	μm
width of domain	200	nm
depth of domain	12	nm
height of sensor	100	nm
width of sensor	100	nm
number of particles	10	–
duration	3	s
stepsize	5	μs
iterations	5000	–
probe molecule density	3×10^{12}	cm^{-2}

Table 5.2: Used parameters for the simulations investigating the effect of the initial conditions on the sensor behavior.

difference between these two vanishes again and the situation is similar as in the cases discussed in the previous section.

This shows that asymmetrical initial conditions have low effects in the investigated situation. This means that there is no urgent need for experimental improvements in order to lower the waiting time until an optimal signal-to-noise ratio is obtained.

5.4   Summary

In this last part, we simulated the biosensor behavior with a one-dimensional as well as with a two-dimensional model. The 1D model allowed insight in the basic behavior of the system, which includes dependences on the target-molecule density in the liquid, the probe-molecule density at the surface and different initial conditions. Important features for experimentalist have beend discovered, that help to rationally design the biosensors.

In the 2D case, the effect of the sensor geometry was considered. Especially the different regions of the surface were of interest here, and insight not only on the signal, but only on the noise was given here. The subsequent study of asymmetrical initial conditions revealed that the effects are very small, which might allow a neglection of the asymmetry in the initial conditions in the first place. However, it has to be kept in mind that the overall initial conditions have indeed great impact on the sensor behavior.

Chapter 6

Conclusions and Outlook

There were two main objectives in this work. The first task was the determination of parameters governing surface processes at nanowire sensors from experimental data. Secondly, simulations of biomolecule hybridization at biosensor surface were to be performed by taking into account the random nature of all the chemical processes taking place within the system.

To obtain numerical values for parameters describing the interactions of the target molecules with the surface, a deterministic model was adopted from literature and refined for our case. The mass action law allows a formulation in terms of ordinary differential equations. The main difficulty here is that the system of equations is highly nonlinear in the case of gas sensors, which is due to an exponential term related to the density of available electrons. Therefore, the differential equations can only be solved numerically. Furthermore, the parameters governing the processes arise also within exponential, which makes their determination difficult. When considering biosensors, the situation is easier since the differential equation becomes linear under certain assumptions.

This model was used to investigate measurements performed with prototypes of SnO_2 single nanowire gas sensors. These devices were fabricated by the group of Anton Köck, who collaborated with our group in this project.

For the parameter determination, we first considered measurements under inert atmosphere, which is ideal for a stepwise estimation procedure. We obtained parameters determined from five different temperatures between 250°C and 350°C.

Next, we considered the sensor behavior during carbon monoxide adsorption at 300°C as well as at 350°C, where the results from the inert-atmosphere case could already be exploited.

Finally, we also investigated the adsorption of hydrogen in an atmosphere of dry air, which

turned out to be complicated, since all parameters had to be estimated at once from the given data. Therefore, we only obtained results for one constant temperature, which was 300°C in this experiment.

This investigation was completed by a comparison of different error notions in order to find out the best one for the determination of the numerical values. It turned out that it is crucial to take all data points into account for comparison, which means that the maximum norm cannot be used for this task. The best results were obtained for the widely used *least-squares* error.

To tackle the second objective, the deterministic model approach was refined in order to include the random effects. A stochastic model was derived which yields chemical Langevin equations for the surface interactions. When considering gas sensors, this model is sufficient for the description of the system, which allows to draw conclusions on the expected level of biological noise in the experiments. In fact, it turned out that the noise level increases with an increasing number of reactions taking place. This qualitative approach worked very well within the measurement data again provided by Anton Köck's group. Here, prototypes of CuO single nanowires and nanowire networks detecting hydrogen sulfide and water vapor in air were considered.

However, the diffusion of the target molecules through the liquid is much slower than the transport of a heated gas. Therefore, the surface-interaction processes need to be coupled with a diffusion equation to obtain reliable results. This coupled system was used to simulate the binding efficiency and the corresponding fluctuations at biosensor surfaces.

To calculate the quantities of interest, we implemented two different algorithms. First, for the one-dimensional simulations, we considered a box-based approach, which considers diffusion as well as hybridization as transition between different boxes. Second, since the box approach turns out to bit cumbersome in higher dimensions, we also implemented a random-walk based approach, which was then used for the two-dimensional simulations.

The first set of experiments was conducted using a one-dimensional simulator. Here, we focused on the interplay between diffusion and hybridization at the surface. From these, we extracted information on the equilibrium values of signal, noise and signal-to-noise ratio depending on probe density and target-molecule concentration in the aqueous solution surrounding the sensor. Here, it turned out that there are two notions that can be considered as a signal, which are binding efficiency and surface-charge density. We discussed the advantages of considering each of these quantities throughout the thesis. Furthermore, we discovered that there might be a waiting time to obtain the best signal-to-noise ratio under certain circumstances. This is due to the fact that there is a significant maximum in the variance after a certain period of time when considering high target-molecule concentrations.

In the second set of simulations, we used a two-dimensional simulator to investigate the hybridization at different regions of the surface. It turned out that there are three regions to distinguish in our case, which all showed different qualitative behavior. Therefore, a proper choice of the geometry of the domain yields a better signal-to-noise ratio. However, it also turned out that the optimal signal-to-noise ratio might not be obtained in the equilibrium, which makes it necessary to find the right moment for the detection of the biomolecules.

Finally, we investigated asymetrical initial conditions, which corresponds to a more realistic situation due to the design of the biosensing devices. Considering the hybridization at both halfs of the nanowire, we obtained a difference in the signal in the very beginning of the simulation,

which then vanishes surprisingly fast, i.e. within tenths of seconds. In particular, this effect is very small, so it can be neglected in the first place. However, the overall initial conditions do have significant influence on the sensor behavior, which still makes a proper choice necessary.

Of course, especially for the two-dimensional case, many more different situations, which could not be considered in this thesis, are of interest. Hence, based on the insights obtained in this work, a lot can be done on this topic that will lead to further insights yielding to even better sensor designs that might lead to safe, efficient and reliable sensing of whichever species in the future.

Bibliography

[1] T. Addabbo, F. Bertocci, A. Fort, M. Mugnaini, S. Rocchi, and V. Vignoli. Surface state model for metal oxide p-type conductometric co sensors. In *Instrumentation and Measurement Technology Conference (I2MTC), 2013 IEEE International*, pages 88–92. IEEE, 2013.

[2] M.-W. Ahn, K.-S. Park, J.-H. Heo, J.-G. Park, D.-W. Kim, K. Choi, J.-H. Lee, and S.-H. Hong. Gas sensing properties of defect-controlled ZnO-nanowire gas sensor. *Applied Physics Letters*, 93(26):263103, 2008.

[3] M. Arafat, B. Dinan, S. A. Akbar, and A. Haseeb. Gas sensors based on one dimensional nanostructured metal-oxides: a review. *Sensors*, 12(6):7207–7258, 2012.

[4] N. Barsan, D. Koziej, and U. Weimar. Metal oxide-based gas sensor research: How to? *Sensors and Actuators B: Chemical*, 121(1):18–35, 2007.

[5] N. Barsan and U. Weimar. Conduction model of metal oxide gas sensors. *Journal of Electroceramics*, 7(3):143–167, 2001.

[6] N. Barsan and U. Weimar. Understanding the fundamental principles of metal oxide based gas sensors; the example of CO sensing with SnO_2 sensors in the presence of humidity. *Journal of Physics: Condensed Matter*, 15(20):R813, 2003.

[7] S. Baumgartner and C. Heitzinger. Existence and local uniqueness for 3d self-consistent multiscale models for field-effect sensors. *Commun. Math. Sci.*, 10(2):693–716, 2012.

[8] S. Baumgartner and C. Heitzinger. A one-level FETI method for the drift-diffusion-Poisson system with discontinuities at an interface. *J. Comput. Phys.*, 243:74–86, June 2013.

[9] S. Baumgartner, C. Heitzinger, A. Vacic, and M. A. Reed. Predictive simulations and optimization of nanowire field-effect PSA sensors including screening. *Nanotechnology*, 24(22):225503/1–9, June 2013.

[10] S. Baumgartner, M. Vasicek, A. Bulyha, and C. Heitzinger. Optimization of nanowire DNA sensor sensitivity using self-consistent simulation. *Nanotechnology*, 22(42):425503/1–8, Oct. 2011.

[11] S. Baumgartner, M. Vasicek, and C. Heitzinger. Analysis of field-effect biosensors using self-consistent 3D drift-diffusion and Monte-Carlo simulations. *Procedia Engineering*, 25:407–410, 2011.

[12] S. Baumgartner, M. Vasicek, and C. Heitzinger. Modeling and simulation of nanowire based field-effect biosensors. In G. Korotcenkov, editor, *Chemical Sensors: Simulation and Modeling. Volume 2: Conductometric-Type Sensors*, pages 447–469. Momentum Press, 2012.

[13] P. Bergveld. Development of an ion-sensitive solid-state device for neurophysiological measurements. *Biomedical engineering, IEEE Transactions on*, (1):70–71, 1970.

[14] A. Bielanski, J. Deren, and J. Haber. Electric conductivity and catalytic activity of semi-conducting oxide catalysts. *Nature*, 179:668–669, 1957.

[15] J. Boyle and K. Jones. The effects of CO, water vapor and surface temperature on the conductivity of a SnO_2 gas sensor. *Journal of Electronic Materials*, 6(6):717–733, 1977.

[16] E. Brunet. *Fabrication of tin dioxide nanowire gas sensors*. Dissertation, Vienna University of Technology, 2014.

[17] E. Brunet, T. Maier, G. Mutinati, S. Steinhauer, A. Köck, C. Gspan, and W. Grogger. Comparison of the gas sensing performance of SnO_2 thin film and SnO_2 nanowire sensors. *Sensors and Actuators B: Chemical*, 165(1):110–118, 2012.

[18] A. Bulyha. *Modeling and Simulation of field-effect biosensors*. Dissertation, University of Vienna, 2011.

[19] J. Chen, K. Wang, L. Hartman, and W. Zhou. H_2S detection by vertically aligned CuO nanowire array sensors. *The Journal of Physical Chemistry C*, 112(41):16017–16021, 2008.

[20] Y.-J. Choi, I.-S. Hwang, J.-G. Park, K. J. Choi, J.-H. Park, and J.-H. Lee. Novel fabrication of an SnO_2 nanowire gas sensor with high sensitivity. *Nanotechnology*, 19(9):095508, 2008.

[21] E. Comini, G. Faglia, G. Sberveglieri, D. Calestani, L. Zanotti, and M. Zha. Tin oxide nanobelts electrical and sensing properties. *Sensors and Actuators B: Chemical*, 111:2–6, 2005.

[22] Y. Cui, Q. Wei, H. Park, and C. M. Lieber. Nanowire nanosensors for highly sensitive and selective detection of biological and chemical species. *Science*, 293(5533):1289–1292, 2001.

[23] I. Daubechies. Orthonormal bases of compactly supported wavelets. *Communications on pure and applied mathematics*, 41(7):909–996, 1988.

[24] M. Deen, M. Shinwari, J. Ranuárez, and D. Landheer. Noise considerations in field-effect biosensors. *Journal of applied physics*, 100(7):074703, 2006.

[25] J. Ding, T. J. McAvoy, R. E. Cavicchi, and S. Semancik. Surface state trapping models for SnO_2-based microhotplate sensors. *Sensors and Actuators B: Chemical*, 77(3):597–613, 2001.

[26] X. Duan, Y. Li, N. K. Rajan, D. A. Routenberg, Y. Modis, and M. A. Reed. Quantification of the affinities and kinetics of protein interactions using silicon nanowire biosensors. *Nature Nanotechnology*, 7(6):401–407, 2012.

[27] R. Erban, J. Chapman, and P. Maini. A practical guide to stochastic simulations of reaction-diffusion processes. *arXiv preprint arXiv:0704.1908*, 2007.

[28] G. Filipič and U. Cvelbar. Copper oxide nanowires: a review of growth. *Nanotechnology*, 23(19):194001, 2012.

[29] A. Fort, M. Mugnaini, S. Rocchi, M. B. Serrano-Santos, V. Vignoli, and R. Spinicci. Simplified models for SnO_2 sensors during chemical and thermal transients in mixtures of inert, oxidizing and reducing gases. *Sensors and Actuators B: Chemical*, 124(1):245–259, 2007.

[30] A. Fort, M. Mugnaini, S. Rocchi, V. Vignoli, E. Comini, G. Faglia, and A. Ponzoni. Metal-oxide nanowire sensors for CO detection: Characterization and modeling. *Sensors and Actuators B: Chemical*, 148(1):283–291, 2010.

[31] A. Fort, S. Rocchi, M. B. Serrano-Santos, R. Spinicci, and V. Vignoli. Surface state model for conductance responses during thermal-modulation of SnO_2-based thick film sensors: Part I—model derivation. *Instrumentation and Measurement, IEEE Transactions on*, 55(6):2102–2106, 2006.

[32] L. Francioso, A. Taurino, A. Forleo, and P. Siciliano. TiO_2 nanowires array fabrication and gas sensing properties. *Sensors and Actuators B: Chemical*, 130(1):70–76, 2008.

[33] D. T. Gillespie. A general method for numerically simulating the stochastic time evolution of coupled chemical reactions. *Journal of computational physics*, 22(4):403–434, 1976.

[34] D. T. Gillespie. The chemical Langevin equation. *The Journal of Chemical Physics*, 113(1):297–306, 2000.

[35] D. T. Gillespie. Simulation methods in systems biology. In *Formal Methods for Computational Systems Biology*, pages 125–167. Springer, 2008.

[36] J. Gong, Q. Chen, W. Fei, and S. Seal. Micromachined nanocrystalline SnO_2 chemical gas sensors for electronic nose. *Sensors and Actuators B: Chemical*, 102(1):117–125, 2004.

[37] C. Griessler, E. Brunet, T. Maier, S. Steinhauer, A. Köck, T. Jordi, F. Schrank, and M. Schrems. Tin oxide nanosensors for highly sensitive toxic gas detection and their 3D system integration. *Microelectronic Engineering*, 88(8):1779–1781, 2011.

[38] S. Hahn, N. Barsan, U. Weimar, S. Ejakov, J. Visser, and R. Soltis. CO sensing with SnO_2 thick film sensors: role of oxygen and water vapour. *Thin Solid Films*, 436(1):17–24, 2003.

[39] Z. Hai-Lang and H. Shi-Jun. Viscosity and density of water + sodium chloride + potassium chloride solutions at 298.15 K. *Journal of Chemical & Engineering Data*, 41(3):516–520, 1996.

[40] A. Hassibi, R. Navid, R. W. Dutton, and T. H. Lee. Comprehensive study of noise processes in electrode electrolyte interfaces. *Journal of applied physics*, 96(2):1074–1082, 2004.

[41] A. Hassibi, H. Vikalo, and A. Hajimiri. On noise processes and limits of performance in biosensors. *Journal of applied physics*, 102(1):014909, 2007.

[42] A. Hassibi, S. Zahedi, R. Navid, R. W. Dutton, and T. H. Lee. Biological shot-noise and quantum-limited signal-to-noise ratio in affinity-based biosensors. *Journal of Applied Physics*, 97(8):084701, 2005.

[43] G. Heiland. Zum Einfluß von adsorbiertem Sauerstoff auf die elektrische Leitfähigkeit von Zinkoxydkristallen. *Zeitschrift für Physik*, 138(3-4):459–464, 1954.

[44] C. Heitzinger, Y. Liu, N. Mauser, C. Ringhofer, and R. W. Dutton. Calculation of fluctuations in boundary layers of nanowire field-effect biosensors. *J. Comput. Theor. Nanosci.*, 7(12):2574–2580, 2010.

[45] C. Heitzinger, N. Mauser, and C. Ringhofer. Multiscale modeling of planar and nanowire field-effect biosensors. *SIAM J. Appl. Math.*, 70(5):1634–1654, 2010.

[46] F. Hernandez-Ramirez, A. Tarancon, O. Casals, J. Arbiol, A. Romano-Rodriguez, and J. Morante. High response and stability in CO and humidity measures using a single SnO_2 nanowire. *Sensors and Actuators B: Chemical*, 121(1):3–17, 2007.

[47] M. Hübner, C. Simion, A. Tomescu-Stănoiu, S. Pokhrel, N. Bârsan, and U. Weimar. Influence of humidity on CO sensing with p-type CuO thick film gas sensors. *Sensors and Actuators B: Chemical*, 153(2):347–353, 2011.

[48] H. K. Hunt and A. M. Armani. Label-free biological and chemical sensors. *Nanoscale*, 2(9):1544–1559, 2010.

[49] I.-S. Hwang, J.-K. Choi, S.-J. Kim, K.-Y. Dong, J.-H. Kwon, B.-K. Ju, and J.-H. Lee. Enhanced H_2S sensing characteristics of SnO_2 nanowires functionalized with CuO. *Sensors and Actuators B: Chemical*, 142(1):105–110, 2009.

[50] M. Kaur, K. Muthe, S. Despande, S. Choudhury, J. Singh, N. Verma, S. Gupta, and J. Yakhmi. Growth and branching of CuO nanowires by thermal oxidation of copper. *Journal of Crystal Growth*, 289(2):670–675, 2006.

[51] Y.-S. Kim, I.-S. Hwang, S.-J. Kim, C.-Y. Lee, and J.-H. Lee. CuO nanowire gas sensors for air quality control in automotive cabin. *Sensors and Actuators B: Chemical*, 135(1):298–303, 2008.

[52] A. Kolmakov, Y. Zhang, G. Cheng, and M. Moskovits. Detection of CO and O_2 using tin oxide nanowire sensors. *Advanced Materials*, 15(12):997–1000, 2003.

[53] G. Korotcenkov. Metal oxides for solid-state gas sensors: What determines our choice? *Materials Science and Engineering: B*, 139(1):1–23, 2007.

[54] D. Koziej, N. Bârsan, U. Weimar, J. Szuber, K. Shimanoe, and N. Yamazoe. Water–oxygen interplay on tin dioxide surface: implication on gas sensing. *Chemical physics letters*, 410(4):321–323, 2005.

[55] V. Kumar, S. Sen, K. Muthe, N. Gaur, S. Gupta, and J. Yakhmi. Copper doped SnO_2 nanowires as highly sensitive H_2S gas sensor. *Sensors and Actuators B: Chemical*, 138(2):587–590, 2009.

[56] K. J. Laidler. The development of the Arrhenius equation. *Journal of Chemical Education*, 61(6):494, 1984.

[57] A. Leung, P. M. Shankar, and R. Mutharasan. A review of fiber-optic biosensors. *Sensors and Actuators B: Chemical*, 125(2):688–703, 2007.

[58] D. Li, J. Hu, R. Wu, and J. G. Lu. Conductometric chemical sensor based on individual CuO nanowires. *Nanotechnology*, 21(48):485502, 2010.

[59] X. Li, Y. Wang, Y. Lei, and Z. Gu. Highly sensitive H_2S sensor based on template-synthesized CuO nanowires. *Rsc Advances*, 2(6):2302–2307, 2012.

[60] L. Liao, Z. Zhang, B. Yan, Z. Zheng, Q. Bao, T. Wu, C. Li, Z. Shen, J. Zhang, H. Gong, et al. Multifunctional CuO nanowire devices: p-type field effect transistors and CO gas sensors. *Nanotechnology*, 20(8):085203, 2009.

[61] H.-H. Lin, C.-Y. Wang, H. C. Shih, J.-M. Chen, and C.-T. Hsieh. Characterizing well-ordered CuO nanofibrils synthesized through gas-solid reactions. *Journal of Applied Physics*, 95(10):5889–5895, 2004.

[62] V. Malyshev and A. Pislyakov. SnO_2-based thick-film-resistive sensor for H_2S detection in the concentration range of 1–10 mg m^{-3}. *Sensors and Actuators B: Chemical*, 47(1):181–188, 1998.

[63] V. Malyshev and A. Pislyakov. Investigation of gas-sensitivity of sensor structures to hydrogen in a wide range of temperature, concentration and humidity of gas medium. *Sensors and Actuators B: Chemical*, 134(2):913–921, 2008.

[64] P. A. Markowich, C. A. Ringhofer, and C. Schmeiser. *Semiconductor equations*. Springer-Verlag New York, Inc., 1990.

[65] K. Mazloomi and C. Gomes. Hydrogen as an energy carrier: prospects and challenges. *Renewable and Sustainable Energy Reviews*, 16(5):3024–3033, 2012.

[66] H. Meixner, J. Gerblinger, U. Lampe, and M. Fleischer. Thin-film gas sensors based on semiconducting metal oxides. *Sensors and Actuators B: Chemical*, 23(2):119–125, 1995.

[67] Y. Meyer. Principe d'incertitude, bases hilbertiennes et algebres d'operateurs. *Séminaire Bourbaki*, 28:209–223, 1985.

[68] S. R. Morrison. *The chemical physics of surfaces*. Plenum, 1990.

[69] F. Mugwang'a, P. Karimi, W. Njoroge, O. Omayio, and S. Waita. Optical characterization of copper oxide thin films prepared by reactive DC magnetron sputtering for solar cell applications. *International Journal of Advanced Renewable Energy Research (IJARER)*, 1(8), 2012.

[70] T. Naoyoshi. Gas-detecting device, Dec. 28 1971. US Patent 3,631,436.

[71] T. Naoyoshi. Gas detecting device, Oct. 3 1972. US Patent 3,695,848.

[72] B. Øksendal. *Stochastic differential equations*. Springer, 2003.

[73] T. Oyabu. Sensing characteristics of SnO_2 thin film gas sensor. *Journal of Applied Physics*, 53(4):2785–2787, 1982.

[74] F. Patolsky, G. Zheng, and C. M. Lieber. Fabrication of silicon nanowire devices for ultrasensitive, label-free, real-time detection of biological and chemical species. *Nature protocols*, 1(4):1711–1724, 2006.

[75] A. W. Peterson, R. J. Heaton, and R. M. Georgiadis. The effect of surface probe density on DNA hybridization. *Nucleic acids research*, 29(24):5163–5168, 2001.

[76] A. Ponzoni, E. Comini, G. Sberveglieri, J. Zhou, S. Z. Deng, N. S. Xu, Y. Ding, and Z. L. Wang. Ultrasensitive and highly selective gas sensors using three-dimensional tungsten oxide nanowire networks. *Applied Physics Letters*, 88(20):203101, 2006.

[77] P. E. Rouse Jr. A theory of the linear viscoelastic properties of dilute solutions of coiling polymers. *The Journal of Chemical Physics*, 21(7):1272–1280, 1953.

[78] G. Sakai, N. S. Baik, N. Miura, and N. Yamazoe. Gas sensing properties of tin oxide thin films fabricated from hydrothermally treated nanoparticles: Dependence of CO and H_2 response on film thickness. *Sensors and Actuators B: Chemical*, 77(1):116–121, 2001.

[79] K. Santra, C. Sarkar, M. Mukherjee, and B. Ghosh. Copper oxide thin films grown by plasma evaporation method. *Thin Solid Films*, 213(2):226–229, 1992.

[80] T. Seiyama, A. Kato, K. Fujiishi, and M. Nagatani. A new detector for gaseous components using semiconductive thin films. *Analytical Chemistry*, 34(11):1502–1503, 1962.

[81] S. Selberherr. *Analysis and simulation of semiconductor devices*. Springer Wien; New York, 1984.

[82] P. Serrini, V. Briois, M. Horrillo, A. Traverse, and L. Manes. Chemical composition and crystalline structure of SnO_2 thin films used as gas sensors. *Thin Solid Films*, 304(1):113–122, 1997.

[83] P. Shankar and J. B. B. Rayappan. Gas sensing mechanism of metal oxides: The role of ambient atmosphere, type of semiconductor and gases-a review. *ScienceJet*, 4:126, 2015.

[84] F. Shao, F. Hernández-Ramírez, J. Prades, C. Fàbrega, T. Andreu, and J. Morante. Copper (ii) oxide nanowires for p-type conductometric NH_3 sensing. *Applied Surface Science*, 2014.

[85] Y. Shen, T. Yamazaki, Z. Liu, D. Meng, T. Kikuta, N. Nakatani, M. Saito, and M. Mori. Microstructure and H_2 gas sensing properties of undoped and Pd-doped SnO_2 nanowires. *Sensors and Actuators B: Chemical*, 135(2):524–529, 2009.

[86] I. F. Silvera and J. W. Cole. Metallic hydrogen: The most powerful rocket fuel yet to exist. In *Journal of Physics: Conference Series*, volume 215, page 012194. IOP Publishing, 2010.

[87] S. Steinhauer. *Gas Sensing Properties of Metal Oxide Nanowires and their CMOS Integration*. Dissertation, Vienna University of Technology, 2014.

[88] S. Steinhauer, E. Brunet, T. Maier, G. Mutinati, and A. Köck. Suspended cuo nanowires for ppb level H_2S sensing in dry and humid atmosphere. *Sensors and Actuators B: Chemical*, 186:550–556, 2013.

[89] S. Steinhauer, E. Brunet, T. Maier, G. Mutinati, A. Köck, O. Freudenberg, C. Gspan, W. Grogger, A. Neuhold, and R. Resel. Gas sensing properties of novel CuO nanowire devices. *Sensors and Actuators B: Chemical*, 187:50–57, 2013.

[90] E. Stern, J. F. Klemic, D. A. Routenberg, P. N. Wyrembak, D. B. Turner-Evans, A. D. Hamilton, D. A. LaVan, T. M. Fahmy, and M. A. Reed. Label-free immunodetection with CMOS-compatible semiconducting nanowires. *Nature*, 445(7127):519–522, 2007.

[91] E. Stern, A. Vacic, N. K. Rajan, J. M. Criscione, J. Park, B. R. Ilic, D. J. Mooney, M. A. Reed, and T. M. Fahmy. Label-free biomarker detection from whole blood. *Nature nanotechnology*, 5(2):138–142, 2010.

[92] M. M. Tirado, C. L. Martinez, and J. G. de la Torre. Comparison of theories for the translational and rotational diffusion coefficients of rod-like macromolecules. Application to short DNA fragments. *The Journal of chemical physics*, 81(4):2047–2052, 1984.

[93] D. R. Tree, A. Muralidhar, P. S. Doyle, and K. D. Dorfman. Is DNA a good model polymer? *Macromolecules*, 46(20):8369–8382, 2013.

[94] G. Tulzer, S. Baumgartner, E. Brunet, G. Mutinati, S. Steinhauer, A. Köck, and C. Heitzinger. Inverse modeling of CO adsorption processes at semiconductor nanowire surfaces for selective gas detection. In *Proc. Computational Methods in Applied Mathematics (CMAM 2012)*, pages 54–55, Berlin, Germany, 30 July – 3 August 2012.

[95] G. Tulzer, S. Baumgartner, E. Brunet, G. Mutinati, S. Steinhauer, A. Köck, and C. Heitzinger. Modeling H_2 adsorption processes at SnO_2 nanowire surfaces: Parameter estimation and simulation. In *Proc. 6th International Conference on Biomedical Electronics and Devices (BIODEVICES 2013)*, pages 265–268, Barcelona, Spain, 11–14 February 2013.

[96] G. Tulzer, S. Baumgartner, E. Brunet, G. C. Mutinati, S. Steinhauer, A. Köck, P. E. Barbano, and C. Heitzinger. Kinetic parameter estimation and fluctuation analysis of CO at SnO_2 single nanowires. *Nanotechnology*, 24(31):315501, 2013.

[97] G. Tulzer, S. Baumgartner, E. Brunet, G. C. Mutinati, S. Steinhauer, A. Köck, and C. Heitzinger. Inverse modeling of CO reactions at SnO_2 nanowire surfaces for selective detection. *Procedia Engineering*, 47:809–812, 2012.

[98] G. Tulzer and C. Heitzinger. Fluctuations due to association and dissociation processes at nanowire-biosensor surfaces and their optimal design. *Nanotechnology*, 26(2):025502, 2015.

[99] G. Tulzer and C. Heitzinger. Noise and fluctuations in nanowire biosensors. In *Proc. 8th Vienna International Conference on Mathematical Modelling (MATHMOD 2015)*, Vienna, Austria, Feb. 2015. At press.

[100] G. Tulzer, S. Steinhauer, E. Brunet, G. Mutinati, A. Köck, and C. Heitzinger. Noise-level analysis of metal-oxide nanowire gas-sensor signals for selective gas detection. In

Proc. International Conference on One-Dimensional Nanomaterials (ICON 2013), page 161, Annecy, France, 23–26 September 2013.

[101] Q. Wan, Q. Li, Y. Chen, T.-H. Wang, X. He, J. Li, and C. Lin. Fabrication and ethanol sensing characteristics of ZnO nanowire gas sensors. *Applied Physics Letters*, 84(18):3654–3656, 2004.

[102] B. Wang, L. Zhu, Y. Yang, N. Xu, and G. Yang. Fabrication of a SnO_2 nanowire gas sensor and sensor performance for hydrogen. *The Journal of Physical Chemistry C*, 112(17):6643–6647, 2008.

[103] N. Yamazoe. Toward innovations of gas sensor technology. *Sensors and Actuators B: Chemical*, 108(1):2–14, 2005.

[104] N. Yamazoe, J. Fuchigami, M. Kishikawa, and T. Seiyama. Interactions of tin oxide surface with O_2, H_2O and H_2. *Surface Science*, 86:335–344, 1979.

[105] D. Zappa, E. Comini, R. Zamani, J. Arbiol, J. Morante, and G. Sberveglieri. Preparation of copper oxide nanowire-based conductometric chemical sensors. *Sensors and Actuators B: Chemical*, 182:7–15, 2013.

[106] D. Zhang, Z. Liu, C. Li, T. Tang, X. Liu, S. Han, B. Lei, and C. Zhou. Detection of NO_2 down to ppb levels using individual and multiple In_2O_3 nanowire devices. *Nano letters*, 4(10):1919–1924, 2004.

[107] F. Zhang, A. Zhu, Y. Luo, Y. Tian, J. Yang, and Y. Qin. CuO nanosheets for sensitive and selective determination of H_2S with high recovery ability. *The Journal of Physical Chemistry C*, 114(45):19214–19219, 2010.

[108] G. Zheng, F. Patolsky, Y. Cui, W. U. Wang, and C. M. Lieber. Multiplexed electrical detection of cancer markers with nanowire sensor arrays. *Nature biotechnology*, 23(10):1294–1301, 2005.

[109] D. Zhou, L. Gan, S. Gong, Q. Fu, and H. Liu. p-type metal oxide doped SnO_2 thin films for H_2 detection. *Sensor Letters*, 9(2):651–654, 2011.

Curriculum Vitae

Personal Information

Name	Gerhard Tulzer
Date of Birth	July 24, 1986
City of Birth	Linz, Austria
Citizenship	Austria

Education

Since 2014	**Doctoral studies in mathematics**, Vienna University of Technology
	Thesis: Modeling and Simulation of Surface Processes at Nanoscale Sensors
	Advisor: Clemens Heitzinger
2011–2014	**Doctoral studies in mathematics**, University of Vienna
Since 2012	**Master studies in physics**, University of Vienna
2008–2012	**Bachelor studies in physics**, University of Vienna
2005–2011	**Diploma studies in Mathematics**, University of Vienna
	Thesis: On symmetry of steady periodic water waves with constant vorticity
	Advisor: Adrian Constantin
10/2004–09/2005	**Military service ("Einjährig-Freiwilligen-Ausbildung")**
06/2004	**Highschool graduation**

Academic Employment

Since 11/2013	**Vienna University of Technology**
	START project No. Y-660 *"Partial Differential Equations in Nanotechnology"*
04/2012–09/2013	**Austrian Institute of Technology**
	WWTF (Viennese Science and Technology Fund) project No. MA09-028 *"Mathematics and Nanosensors"*
09/2011–03/2012	**Wolfgang Pauli Institute**
	WWTF (Viennese Science and Technology Fund) project No. MA09-028 *"Mathematics and Nanosensors"*

Research Visits

11/2013	**Arizona State University**
	School of Mathematical and Statistical Sciences
10/2014	**Arizona State University**
	School of Mathematical and Statistical Sciences

Journal Publications

Tulzer G. and Heitzinger C. Fluctuations due to association and dissociation processes at nanowire-biosensor surfaces and their optimal design. *Nanotechnology*, **26** (2), 025502, 2015.

Tulzer G., Baumgartner S., Brunet E., Mutinati G.C., Steinhauer S., Köck A., Barbano P.E. and Heitzinger C. Kinetic parameter estimation and fluctuation analysis of CO at SNO_2 single nanowires. *Nanotechnology*, **24** (31), 315501, 2013.

Tulzer G., Baumgartner S., Brunet E., Mutinati G.C., Steinhauer S., Köck A. and Heitzinger C. Inverse modeling of CO reactions at SnO_2 nanowire surface for selective detection. *Procedia Engineering*, **47**, 809–812, 2012.

Tulzer G. On the symmetry of steady periodic water waves with stagnation points, *Communications on Pure and Applied Analysis*, **11**, 1577–1586, 2012.

Contributions to Conferences and Workshops

Tulzer G. and Heitzinger C. Noise and Fluctuations in Nanowire Biosensors. In *Proc. 8th Vienna International Conference on Mathematical Modeling – MATHMOD, February 18–20, 2015*, Vienna, Austria (at press).

Tulzer G. and Heitzinger C. Various strategies for the numerical stochastic homogenization of the stochastic Poisson and Helmholtz equations. In *Proc. SIAM Annual Meeting, July 7–11, 2014*, page 15, Chicago, USA.

Tulzer G. and Heitzinger C. Monte-Carlo and quasi-Monte-Carlo approaches for the numerical

stochastic homogenization of elliptic partial differential equations. In *Proc. 11th International Conference on Monte Carlo and Quasi-Monte Carlo Methods in Scientific Computing (MC-QMC2014), April 6–11, 2014*, page 168, Leuven, Belgium.

Tulzer G. and Heitzinger C. Simulations of Fluctuations and Noise in Nanoscale Sensors. In *Proc. 5th International Congress on Nanotechnology in Medicine and Biology (BioNanoMed 2014), March 26–28, 2014*, page 52, Krems, Austria.

Tulzer G., Steinhauer S., Brunet E., Mutinati G.C., Köck A., and Heitzinger C. Noise-level analysis of metal-oxide nanowire gas-sensor signals for selective gas detection. In *Proc. International Conference on One-Dimensional Nanomaterials (ICON 2013), September 23–26, 2013*, page 161, Annecy, France.

Tulzer G., Baumgartner S., Brunet E., Mutinati G.C., Steinhauer S., Köck A., and Heitzinger C. Modeling H_2 adsorption processes at SnO_2 nanowire surfaces: Parameter estimation and simulation. In *Proc. 6th International Conference on Biomedical Electronics and Devices (BIODE-VICES 2013) February 11–14, 2013*, pages 265-268, Barcelona, Spain.

Tulzer G., Baumgartner S., Brunet E., Mutinati G.C., Steinhauer S., Köck A., and Heitzinger C. Characteristics of CO and H_2 detection with single nanowire gas sensors. In *Proc. 5th Szeged International Workshop on Advances in Nanoscience 2012 (SIWAN 2012), October 24–27, 2012*, pages 36-37, Szeged, Hungary.

Tulzer G., Baumgartner S., Brunet E., Mutinati G.C., Steinhauer S., Köck A., and Heitzinger C. Inverse modeling of CO reactions at SnO_2 nanowire surfaces for selective detection. In *Proc. Eurosensors XXVI, September 9–12, 2012*, pages W2C-4/1-4, Krakow, Poland.

Tulzer G., Baumgartner S., Brunet E., Mutinati G.C., Steinhauer S., Köck A., and Heitzinger C. Inverse modeling of CO adsorption processes at semiconductor nanowire surfaces for selective gas detection. In *Proc. Computational Methods in Applied Mathematics (CMAM 2012), July 30 – August 3, 2012*, pages 54-55, Berlin, Germany.

Tulzer G., Baumgartner S., Brunet E., Mutinati G.C., Steinhauer S., Köck A., and Heitzinger C. Calculation of gas surface-reaction parameters at SnO_2 nanowire surfaces. In *Proc. 9th International Conference on Nanosciences and Nanotechnologies (NN12), July 3–6, 2012*, page 59, Thessaloniki, Greece.

Brunet E., Tulzer G., Steinhauer S., Mutinati G.C., Köck A., Vasicek M. and Heitzinger C. Fabrication and simulation of SnO_2 nanowire gas sensors. In *Proc. 3rd International Congress on Nanotechnology in Medicine and Biology (BioNanoMed 2012), March 1–2, 2012*, page 8, Krems, Austria.